THE EFFECTS OF OFF-DESIGN CONDITIONS ON THE LAMINAR-TO-TURBULENT TRANSITION LOCATION ON A SLOTTED, NATURAL-LAMINAR-FLOW AIRFOIL

A Thesis

by

DANIEL THOMAS HESTON

Submitted to the Office of Graduate and Professional Studies of
Texas A&M University
in partial fulfillment of the requirements for the degree of

MASTER OF SCIENCE

Chair of Committee,	Helen Reed
Committee Members,	Edward White
	Rodney Bowersox
	Prabir Daripa
Head of Department,	Srinivas Vadali

December 2020

Major Subject: Aerospace Engineering

ABSTRACT

The National Aeronautics and Space Administration (NASA) Aeronautics Research Mission Directorate (ARMD) vision for aeronautical research has defined the goal of creating an ultra-efficient subsonic transport flight vehicle. In order to create such a vehicle, the Advanced Aerodynamic Design Center for Ultra-Efficient Vehicles was established. This center is developing a new airfoil capable of maintaining laminar flow. At Texas A&M's Computational Stability and Transition Laboratory, I am working to define the allowable sweep and twist for a new slotted, natural-laminar-flow (SNLF) airfoil, the S207. Setting the limits for these sweep and twist parameters will allow for proper implementation into Boeing's subsonic ultra green aircraft configuration. The goal of this thesis is to identity the maximum sweep angle for which the crossflow instability does not negate the benefits of the natural-laminar-flow (NLF) design of the S207 airfoil, for a range of angles of attack.

To determine this angle, the amplification of all expected disturbances is calculated using the Linear Parabolized Stability Equations (LPSE) on a multitude of sweep angles. In addition to sweep, the effects of angle of attack variation are also examined. For sweep angles $\geq 20^\circ$ and $c_l \approx 0.65$, crossflow disturbances exceed their critical N-factor value of 5, and therefore crossflow is presumed to onset transition. Lowering the sweep angle to $\Lambda = 15^\circ$ and considering an angle of attack variation, the crossflow N-factors reach 4.6 units. This is below the critical value, but does not allow for much margin of error. Additionally, this critical value does not account for any interaction between the mechanisms, which lowers the N-factor necessary to induce transition. Therefore, a reduced sweep angle of 12.5° is analyzed. For a 12.5° sweep angle, the maximum N-factors achieved are well below the critical values, for all studied angles of attack. Considering the interaction between the Tollmien-Schlichting and crossflow mechanisms, flow over the 12.5° sweep case is still predicted to be laminar. Therefore, the crossflow instability does not appear to negate the benefits of the S207's SNLF design for sweep angles up to and including 12.5° for an angle of attack range of -1.772° to -1.272°.

CONTRIBUTORS AND FUNDING SOURCES

Contributors

This work was supported by a thesis committee consisting of my advisor Dr. Helen Reed and professors Dr.Edward White, Dr.Rodney Bowersox and Dr.Prabir Daripa.

The OVERFLOW solutions presented in Chapters 2 and 3 were provided by Dr. James Coder of the University of Tennessee, Knoxville. This work was also aided by my colleagues Dr.Helen Reed, Dr.Koen Groot and, Ethan Beyak.

All other work conducted for this thesis was completed by the student independently.

Funding Sources

Graduate study was supported as a graduate research assistant at Texas A&M University. This material is based upon work supported by the National Aeronautics and Space Administration (NASA) under cooperative agreement award number NNX17AJ95A. The work was performed under the University Leadership Initiative (ULI) at Texas A&M University as a subcontract to the University of Tennessee, Knoxville Advanced Aerodynamic Design Center for Ultra-Efficient Commercial Vehicles.

NOMENCLATURE

α	Angle of attack
α	Streamwise wavenumber in the leading-edge-orthogonal direction
β	Spanwise wavenumber in the leading-edge-parallel direction
γ	Ratio of specific heats
δ	Boundary-layer height
κ	Coefficient of thermal conductivity
λ_v	Second viscosity coefficient
Λ	Sweep angle
μ	Dynamic viscosity coefficient
ρ	Density
ϕ	Primitive variable vector (u, v, w, T, ρ)
ψ_s	Streamline angle
ψ_w	Wave angle
ω	Angular frequency
a	Speed of sound
$\mathcal{A}$, $\mathcal{B}$, $\mathcal{C}$, $\mathcal{D}$, and $\mathcal{E}$	Linear (5×5) matrices present in LPSE/LST disturbance equations
c	Leading-edge-normal chord length
c_l	Section-lift coefficient
c_p	Specific heat at constant pressure
c_{ph}	Phase speed
E_c	Eckert number

M	Mach number
N	Amplification factor
N_s	Number of leading-edge-orthogonal points in the stability domain
N_y	Number of wall-normal points in the stability domain
P	Pressure
Pr	Prandtl number
R	Specific gas constant
Re	Reynolds number
s	Coordinate in the leading-edge-orthogonal direction which traces the chord
S	Sutherland's temperature
T	Absolute static temperature
u, v, w	Velocity components in (s, y, z) directions, respectively
y	Coordinate in the wall-normal direction
z	Coordinate perpendicular to the leading edge
$\approx$	Approximately equal to

ACRONYMS

AOA	Angle of attack
CF	Crossflow
CST	Computational Stability and Transition
DEKAF	Digits by Ethan, Koen, Alex, and Fernando
EPIC	Euonymous Parabolized Instability Code
IATA	International Air Transport Association
LFC	Laminar flow control
LPSE	Linear parabolized stability equations

LST	Linear stability theory
NASA	National Aeronautics and Space Administration
NLF	Natural-laminar-flow
SCF	Stationary crossflow
SNLF	Slotted, natural-laminar-flow
SUGAR	Subsonic Ultra Green Aircraft Research
TS	Tollmien-Schlichting
ULI	University Leadership Initiative

SUBSCRIPTS

i	Imaginary value
∞	Freestream quantity
I	Correspond the branch-I neutral point
r	Real value
ref	Reference value
w	Pertaining to values at the wall

ACCENTS

$\wedge$	Shape-function quantity
$-$	Basic state quantity
$'$	Disturbance quantity
$\%$	Percentage
$\circ$	Degrees
$\dagger$	Complex conjugate
$\sim$	Slowly varying
$\rightarrow$	Vector

TABLE OF CONTENTS

Page

ABSTRACT ii

CONTRIBUTORS AND FUNDING SOURCES iii

NOMENCLATURE iv

TABLE OF CONTENTS vii

LIST OF FIGURES ix

LIST OF TABLES xi

1. INTRODUCTION 1

    1.1 Motivation 1
    1.2 Background 2
        1.2.1 Instability Mechanisms 2
        1.2.2 Approaches to Control Instability Mechanisms 3
    1.3 Present Work 4

2. METHODOLOGY 8

    2.1 Governing Equations 8
    2.2 Base-Flow Quantification 9
    2.3 Flow Stability 11
        2.3.1 Linear Stability Theory 12
        2.3.2 Linear Parabolized Stability Equations 14
    2.4 Applying Stability Theory 16
    2.5 Analyzing the Results 17

3. STABILITY RESULTS 20

    3.1 Discretization of the (ω, β) Space 20
    3.2 Stability Convergence Analysis 23
    3.3 Sweep Variation Analysis for Design Angle of Attack, $\alpha = -1.520°$ 24
    3.4 Angle of Attack Variation for $\Lambda = 15°$ 29
    3.5 Angle of Attack Variation for $\Lambda = 12.5°$ 35

4. CONCLUSION 41

Page

REFERENCES 44

APPENDIX A. COORDINATE SYSTEM DEFINITION 48

APPENDIX B. GOVERNING EQUATIONS 51

B.1 Nondimensionalization 51
B.2 LST Governing Equations 52
B.2.1 Momentum along the s-Axis 53
B.2.2 Momentum along the y-Axis 53
B.2.3 Momentum along the z-Axis 54
B.2.4 Conservation of Energy 54
B.2.5 Continuity 55
B.3 LPSE Governing Equations 55
B.3.1 Momentum along the s-Axis 56
B.3.2 Momentum along the y-Axis 57
B.3.3 Momentum along the z-Axis 59
B.3.4 Conservation of Energy 59
B.3.5 Continuity 61

APPENDIX C. WAVE ANGLES AND STREAMLINE ANGLES 62

LIST OF FIGURES

FIGURE Page

1.1 S207 Geometry 4
1.2 (a) The S207 airfoil. (b) Pressure distributions for different angles of attack and sweep angles. The sonic pressure-coefficient limit, above which the velocity at the edge of the boundary layer is supersonic, is also indicated by straight lines. 6

3.1 Definitions of the (ω, β) subspaces. Wavelength ranges that are typically associated with crossflow vortices ($4\delta_{99}$, accounting for δ_{99} variation beyond x/c of 2%) are indicated with grey patches. 22
3.2 Comparisons of the N-factor envelopes (composed of individual N-curves for a broad range of frequencies and wavelengths) for $\Lambda = 15^\circ$ and the design angle of attack $\alpha = -1.520^\circ$ ($c_l \approx 0.65$), as computed using the DEKAF and OVERFLOW base-flow solutions and with different resolutions for the stability problem. Low-frequency content is pictured on the left (panel a), while high-frequency content is on the right (panel b). 25

3.3 N-factor envelopes representing the overall maximum values (dashed red lines), the Tollmien-Schlichting mechanism (green), the traveling crossflow mechanism (purple), and the stationary crossflow mechanism (blue) for the angle of attack, $\alpha = -1.520^\circ$. The grey lines represent individual wavenumber and frequency combinations..... 26

3.4 N-factor envelopes representing the overall maximum values (red), the Tollmien-Schlichting (green), stationary crossflow (blue), and traveling crossflow (purple) mechanisms for $\Lambda = 15^\circ$. Selected N-curves, each corresponding to a single (ω, β)-combination, are shown that define the maximum envelope (grey) at the local maximums. The disturbance characteristics of these selected (ω, β)-combinations are then reported in table 3.4..... 31

3.5 Tollmien-Schlichting and stationary crossflow N-factors attained for the 15° sweep case plotted against qualitative representations of the critical "universal" curves representing strong (concave line) and moderate (straight line) interactions. N-factors corresponding to traveling crossflow are also plotted against TS N-factors for completeness. The markers are placed at every 20% of the chord in order to follow the N-factor evolution in x. The first marker, at $x/c \approx 0.20$, is filled in. Additionally, arrows are shown which indicated increasing x/c are drawn. Black lines correspond to the top side of the airfoil, while red lines indicate the bottom side. 35

Page

3.6 N-factor envelopes representing the overall maximum values (red), the Tollmien-Schlichting (green), stationary crossflow (blue), and traveling crossflow (purple) mechanisms for $\Lambda = 12.5°$. Selected N-curves, each corresponding to a single (ω, β)-combination, are shown that define the maximum envelope (grey) at the local maximums. The disturbance characteristics of these selected (ω, β)-combinations are then reported in table 3.5. 37

3.7 Tollmien-Schlichting and crossflow N-factors attained for the $12.5°$ sweep case plotted against critical "universal" curves representing strong (concave line) and moderate (straight line) interactions. N-factors corresponding to traveling crossflow are also plotted against TS N-factors for completeness. The markers are placed at every 20% of the chord in order to follow the N-factor evolution in x. The first marker, at $x/c \approx 0.20$, is filled in. Additionally, arrows are shown which indicated increasing x/c are drawn. Black lines correspond to the top side of the airfoil, while red lines indicate the bottom side. 39

A.1 $s, y, \text{and } z$ coordinates system. x is also displayed here. 48

A.2 Important angles used throughout this study are displayed. The blue line is the inviscid streamline for the $\Lambda = 15°$ sweep case. All variables shown are defined within Section A 49

A.3 Difference between the x and chord axis. 50

B.1 Scaling factor derivation in the streamwise (1) and spanwise (3) directions. $ds_{1,3}$ is the differential surface distance in the (1,3)-direction and $ds_{1,3}^{ref}$ is the corresponding differential surface distance at the wall. 52

LIST OF TABLES

TABLE Page

2.1 Fixed reference parameters 9

3.1 Complete list of the input frequencies ω, in $[\mathrm{Hz}]$. 21

3.2 Complete list of the (magnitude of the) input wavelengths $\lambda = 2\pi/\beta$, in $[\mathrm{mm}]$. 21

3.3 Parameters characterizing the most amplified disturbances as presented in Figure 3.3, considering the design angle of attack ($\alpha = -1.520°$). The purple text represents characteristics expected for the traveling cross mechanism, and green text represents characteristics expected for TS. All calculations were performed on the DEKAF^u base flow data set. The complete lists of ψ_w and ψ_s for these cases is presented in table C.1 within Appendix C. 28

3.4 Parameters characterizing the most relevant disturbances for the sweep angle $\Lambda = 15°$ with varying angles of attack as seen in Figure 3.4. The purple text represents characteristics expected for the traveling cross mechanism, and green text represents characteristics expected for TS. The points where this data was extracted are indicated by grey circles in this figure. The complete lists of ψ_w and ψ_s for these cases is presented in table C.2 within Appendix C. 30

3.5 Parameters characterizing the most relevant disturbances for the sweep angle $\Lambda = 12.5°$ with varying angles of attack as seen in Figure 3.6. The purple text represents characteristics expected for the traveling cross mechanism, and green text represents characteristics expected for TS. The points where this data was extracted are indicated by grey circles in this figure. The complete lists of ψ_w and ψ_s for these cases is presented in table C.3 within Appendix C. 36

C.1 Wave angle and streamline angle values for the sweep angle variation study. These parameters correspond to the most amplified disturbances as presented in Figure 3.3, considering the design angle of attack ($\alpha = -1.520°$). 62

C.2 Wave angle and streamline angle values for the $\Lambda = 12.5°$ sweep case angle of attack variation study. These parameters characterize the most relevant disturbances for this sweep angle with varying angles of attack as seen in Figure 3.4. The points where this data was extracted are indicated by grey circles in this figure. 62

Page

C.3 Wave angle and streamline angle values for the $\Lambda = 12.5^{\circ}$ sweep case angle of attack variation study. These parameters characterize the most relevant disturbances for this sweep angle with varying angles of attack as seen in Figure 3.6. The points where this data was extracted are indicated by grey circles in this figure. 63

1. INTRODUCTION

1.1 Motivation

The International Air Transport Association (IATA) calls for a vast reduction in net emissions for long-haul subsonic transport vehicles. As compared to 2005 emission levels, a reduction of 50% is to be achieved by 2050, in order to greatly reduce the impact of aviation on climate change [1]. IATA and the aviation community expect this goal to be achieved through a combination of ultra-efficient airframes, propulsion technology, and propulsion-airframe integration [2]. To contribute to designing an ultra-efficient airframe in particular, the Advanced Aerodynamic Design Center for Ultra-Efficient Commercial Vehicles was established. This design center was created as a University Leadership Initiative (ULI) in 2016, led by the University of Tennessee, Knoxville, and funded by the National Aeronautics and Space Administration (NASA). As part of the ultra-efficient airframe development, this ULI focuses on an innovative wing concept. Ultimately, this wing design will be integrated into Boeing's Subsonic Ultra Green Aircraft Research (SUGAR) project [1].

In order for this innovative wing concept to aid in the reduction of net emissions, a decrease in turbulence-induced drag on the wing is deemed to be most lucrative. This is explained as follows. First, the largest contributor to total aircraft drag is the skin-friction-drag component. This skin-friction drag accounts for up to 50% of the total drag for long-haul transport aircraft [3][4]. Second, drag due to laminar skin friction can be as much as 90% less than that due to turbulent skin friction [3]. Finally, the wing profile drag, mostly consisting of skin-friction drag, accounts for approximately one third of the total drag for a transport aircraft [5]. Therefore, minimizing turbulent flow over the wing is one way to reduce a large portion of the total aircraft drag, increasing the efficiency of the aircraft.

1.2 Background

A flow's likelihood of transitioning to turbulence is determined by its stability. In this context, stability refers to a system's ability to return to its original state following a small perturbation. Under certain circumstances, some of these perturbations amplify due to existing instability mechanisms. Once these perturbations reach a large enough amplitude, they break down the laminar flow into turbulence. It is important to understand these instability mechanisms in order to control them and prevent the onset of turbulence.

1.2.1 Instability Mechanisms

For subsonic flight conditions on a swept wing, two of the driving instability mechanisms are Tollmien-Schlichting (TS) waves and crossflow (CF) vortices [6]. These two mechanisms are described as follows.

The Tollmien-Schlichting instability is a viscous instability, meaning it is destabilized by the presence of viscosity, which gives rise to high-frequency TS waves [7]. These TS waves propagate in the boundary layer, traveling approximately in the direction of the local inviscid streamline. Tollmien-Schlichting waves are stabilized by a favorable pressure gradient as well as suction at the wall [3][7][8][9].

Crossflow, on the other hand, is an inviscid instability that is either stationary or traveling and is a result of the crossflow velocity component. This crossflow velocity component is created when sweeping the wing misaligns the pressure gradient and the local inviscid streamline. Since the forces caused by the pressure gradient and shear stress must balance at the wall, a velocity component perpendicular to the local inviscid streamline, called crossflow, is generated. The crossflow velocity profile contains a generalized inflection point, and therefore an inviscid instability can occur. Due to the direct relation of this inviscid instability to the crossflow velocity component, this mechanism is referred to as the crossflow instability [6][10][11]. If the crossflow instability is strong enough, the amplitude will grow and give rise to crossflow vortices that will distort the basic state, which can be considered the onset of transition. Whereas a more favorable streamwise pres-

sure gradient stabilizes TS, it has the opposite effect on crossflow. However, both TS and crossflow are destabilized by a more adverse pressure gradient. To prevent crossflow-vortex-induced transition, this pressure gradient must be minimized and/or the sweep angle must be limited.

1.2.2 Approaches to Control Instability Mechanisms

These instability mechanisms have previously been subdued through the implementation of a natural-laminar-flow (NLF) airfoil or by employing laminar flow control (LFC); see reviews by Joslin [3], Reed et al. [9], and Saric et al. [10].

NLF airfoils take advantage of the benefits of a favorable pressure gradient on TS induced transition, while minimizing the sweep to limit the growth of crossflow vortices. Laminar coverage for an NLF airfoil is generally limited to around 70% of the chord, due to a pressure-recovery gradient in the aft portion of the airfoil [5]. This adverse pressure gradient has two possible effects: 1) the strong destabilization of TS waves leading to transition or 2) the possibility of trailing-edge separation.

In contrast to the *passive* geometry-driven mechanisms of the NLF airfoil, LFC airfoils use *active* flow control to increase the laminar-flow extent. For gases, wall cooling is shown to result in lower disturbance growth and wall-normal suction through porous wing skins can result in 100% laminar coverage [9][12]. Unfortunately, these active-flow-control systems are mechanically and structurally complex, leading to high costs and issues in manufacturing and day-to-day operations [5].

In order to maximize laminar-flow coverage, while maintaining mechanical simplicity, Dan Somers of Airfoils Incorporated has designed a new slotted, natural-laminar-flow (SNLF) airfoil named the S207, seen in Figure 1.1. The SNLF airfoil shape has a slot between the upper and lower surfaces near the trailing edge. This slot removes the requirement that the pressure on the upper surface must return to the freestream value at the trailing edge of the fore element, limiting the effectiveness of the NLF airfoil design. This reduction in required pressure recovery extends the available region that can support a favorable pressure gradient. This increased area of favorable pressure gradient, on both the upper and lower surfaces, can result in practically completely

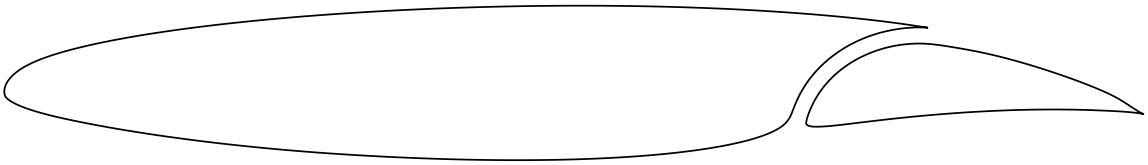

Figure 1.1: S207 Geometry

laminar flow on the fore element. This passive flow control strategy removes the worries and complexity that come with LFC airfoils, while reaching a significant amount of laminar-flow coverage. Although consisting of two elements, each element in the SNLF design is not drastically different from conventional airfoils, making it relatively simple to manufacture [5].

1.3 Present Work

In order to aid in the development of this SNLF airfoil, the Computational Stability and Transition (CST) Lab at Texas A&M is working with the fore element of the S207 airfoil. The CST Lab is working to determine the critical sweep angle for which the crossflow instability negates the benefits of the SNLF design, therefore predicting the sweep-angle range for which laminar flow is maintained. Although sweeping the wing destabilizes the crossflow instability, this is necessary at high-subsonic speeds [13]. The leading-edge-normal Mach number, later referred to as $\mathrm{M}_{\overline{u}_\infty \overline{v}_\infty}$,for the S207 is 0.70 and is predicted to be below the drag-divergence Mach number for a straight wing. By sweeping the wing, the drag-divergence Mach number for the aircraft is increased and the aircraft can fly faster without a significant increase in drag [14][15]. The benefit of flying faster, from an efficiency standpoint, is seen through use of the Bréguet range equation [16], which calculates the range of an aircraft as follows:

$$R = \frac{1}{\mathrm{c}} \frac{VL}{D} \ln \frac{W_i}{W_f} \qquad \Rightarrow \qquad \frac{W_i}{W_f} = \exp\left\{ \frac{R}{\mathrm{c}} \frac{D}{VL} \right\}$$

Here, $R, \mathrm{c}, V, L, D, \text{and } W_i/W_f$ are the range, specific fuel consumption, velocity, lift, aircraft drag, and ratio of initial to final aircraft weight, respectively. This equation shows that if all values except for velocity and the ratio of initial to final aircraft weight are held nearly constant, an increase in velocity leads to a reduction in W_i/W_f. The aircraft emissions are directly responsible for the difference between the initial and final weights of the aircraft and therefore, minimizing this ratio directly minimizes the aircraft emissions.

Previous work by Groot et al., in which I participated, has formed a foundation for this study, quantifying the TS and CF growth rates for sweep angles between 0° and 30° on an airfoil representative of the fore element of the S207, the X207.o [17].

In addition to these sweep-angle-justification efforts, the impact of the variation of the angle of attack on the fore element of the S207 airfoil is studied. The importance of studying the variation in the angle of attack is explained as follows. An aircraft's wings are twisted to create a near-elliptical lift distribution, thereby minimizing the wing's induced drag and bending moment at the root of the wing [15]. Due to this wing twist and assuming the same cross-sectional S207 shape along the span, each section of the planform will effectively see a different angle of attack (AOA). Determining the maximum and minimum angles of attack that are allowable in order to maintain laminar flow is crucial to determining the maximum wing twist. In addition to twist, a given spanwise wing location will see a variety of angles of attack throughout the complete flight envelope. Angle of attack is directly related to the coefficient of lift and therefore AOA will vary from climb to cruise to descent. Presenting the angles of attack for which laminar flow is maintained, for a set of sweep angles, allows the aircraft designers to make an informed decision for the twist distribution on the wing.

Figure 1.2 shows the effects of the angle of attack and sweep on the pressure distribution for the fore element of the S207 airfoil. As mentioned before, the pressure gradient plays a significant role in the growth of the instabilities in question [7][9][18]. Although a decrease in angle of attack leads to a more (less) favorable pressure gradient on the top (bottom) side of the airfoil, the leading-edge-orthogonal pressure distribution is nearly independent of sweep. This independence occurs

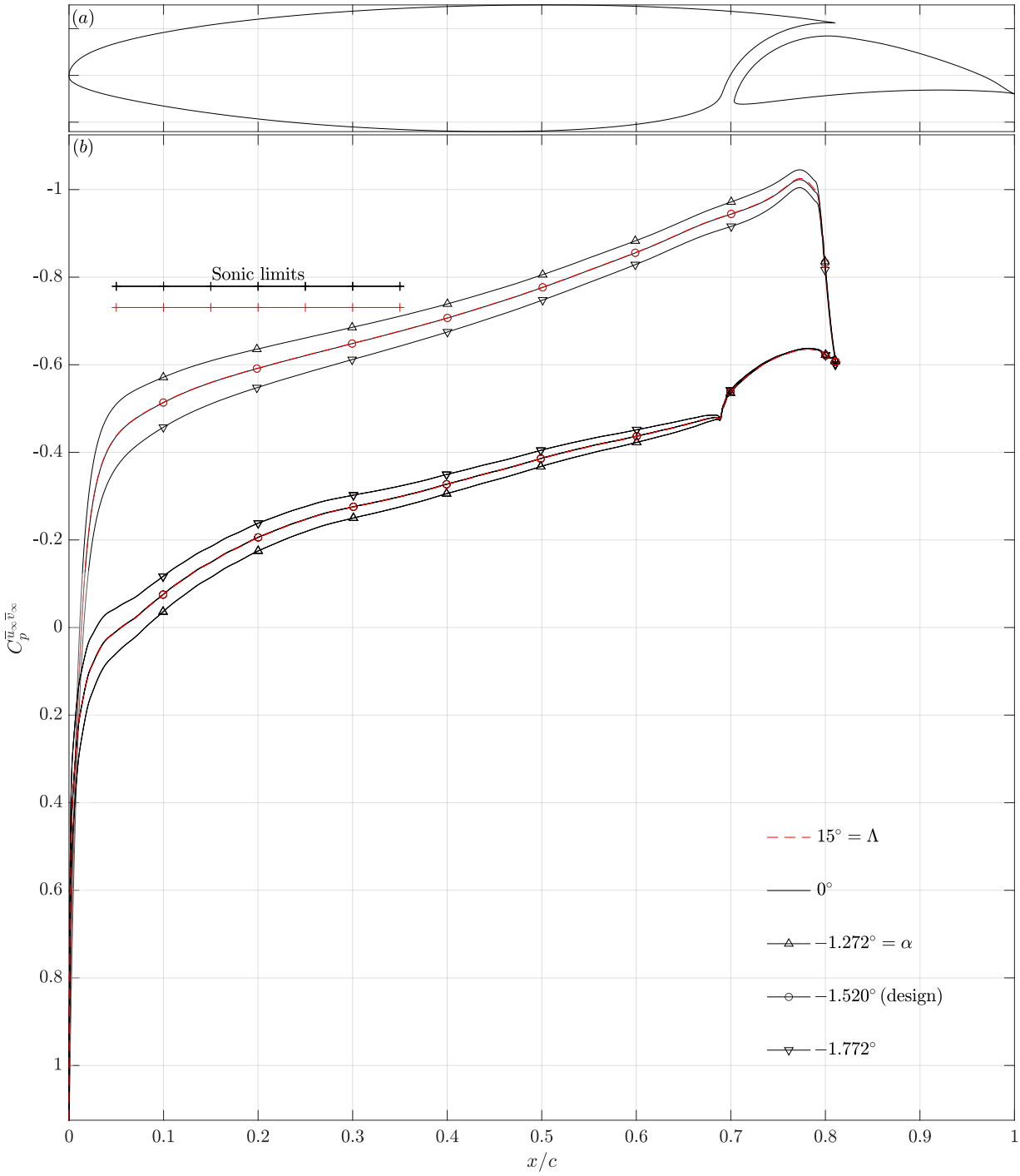

Figure 1.2: (a) The S207 airfoil. (b) Pressure distributions for different angles of attack and sweep angles. The sonic pressure-coefficient limit, above which the velocity at the edge of the boundary layer is supersonic, is also indicated by straight lines.

for the "2-D" C_p definition implemented:

$$C_p^{\overline{u}_\infty \overline{v}_\infty} \equiv \frac{\overline{p}_w - \overline{p}_\infty}{\frac{1}{2}\overline{\rho}_\infty(\overline{u}_\infty^2 + \overline{v}_\infty^2)} \tag{1.1}$$

This $C_p^{\overline{u}_\infty \overline{v}_\infty}$ definition neglects the spanwise freestream velocity in the dynamic pressure term (the denominator). Additionally, $\overline{p}_e$, the pressure at the inviscid wall, is approximately equal to $\overline{p}_w$ and depends only on the leading-edge-orthogonal inviscid flow properties and therefore $C_p^{\overline{u}_\infty \overline{v}_\infty}$ is expected to be nearly constant with respect to sweep variation. This near independence with respect to sweep angle is illustrated with the pressure distribution of the 15° sweep case for the design angle of attack, shown in Figure 1.2 by a red dashed line. Notice that this line lies directly on top of the pressure distribution for the unswept case for the entirely of the chord.

The objective of my thesis work will be to extend the work of Groot et al. [19] on the X207.o to the fore element of the S207 airfoil under flight operating conditions. The effects of sweep angle and angle of attack will be assessed to determine the limits for full-chord laminar flow for the fore element.

2. METHODOLOGY

In this chapter, the methods applied to analyze the effects of sweep angle and angle of attack variation on the laminar-flow coverage of the S207 are presented. The coordinate systems used throughout this section are described and visualized in Appendix A.

2.1 Governing Equations

Computational models of fluid flow are derived from the most general forms of the continuum equations of motions. Conservation of mass, momentum, and energy, respectively seen below, govern the evolution of these flows. The considered form of the momentum equation includes only pressure and viscous forces. For the sake of this paper, the equations below will be referred to as the full, dimensional Navier-Stokes equations.

$$\frac{\partial \rho}{\partial t} + \nabla \cdot (\rho \vec{V}) = 0 \tag{2.1}$$

$$\rho\left[\frac{\partial \vec{V}}{\partial t} + (\vec{V} \cdot \nabla)\vec{V}\right] = -\nabla P + \nabla\Big[\lambda_v(\nabla \cdot \vec{V})\Big] + \nabla \cdot \Big[\mu((\nabla \vec{V} + (\nabla \vec{V})^T)\Big] \tag{2.2}$$

$$\rho c_p\left[\frac{\partial T}{\partial t} + (\vec{V} \cdot \nabla)T\right] = \nabla \cdot (\kappa \nabla T) + \frac{\partial P}{\partial t} + (\vec{V} \cdot \nabla)P + \lambda_v(\nabla \cdot \vec{V})^2 + \frac{\mu}{2}\Big[(\nabla \vec{V}) + (\nabla \vec{V})^T\Big]^2 \tag{2.3}$$

The state variables are $\rho, \vec{V}, \text{and } T$, where $\vec{V}$ is a 3-D vector comprised of the velocity components u, v, w. The terms ρ and T are mass density and temperature, respectively. The remaining variables, $P, c_p, \mu, \lambda_v, \text{and } \kappa$, are given through constitutive relations below:

$$P = \rho R_g T \tag{2.4}$$

$$c_p = \frac{\gamma R_g}{\gamma - 1} \tag{2.5}$$

$$\mu = \mu_{\text{ref}} \left(\frac{T}{T_{\text{ref}}} \right)^{3/2} \frac{T_{\text{ref}} + S}{T + S} \tag{2.6}$$

$$\lambda_v = -\frac{2}{3}\mu, \qquad \kappa = \frac{\mu c_p}{\text{Pr}} \tag{2.7}$$

These equations assume an ideal and calorically perfect gas, Sutherland's law, and Stokes' hypothesis [15][18]. The gas constant (R_g), Prandtl number (Pr), and ratio of specific heats (γ) are assumed to be constant and their values are presented in table 2.1. In Equation 2.6, Sutherlands' law, $\mu_{\text{ref}}, T_{\text{ref}}$, and S are governing constants for a air. The constants used for the calculations performed in this study are also present in table 2.1. These values are all independent of both sweep angle and angle of attack.

Table 2.1: Fixed reference parameters

$\text{M}_{\overline{u}_\infty \overline{v}_\infty}$	$\text{Re}_c^{\overline{u}_\infty \overline{v}_\infty}$	$c\,[\text{m}]$	altitude [ft]	$\overline{T}_\infty\,[\text{K}]$	$\overline{p}_\infty\,[\text{Pa}]$
0.70	13.2×10^6	3.65084	44,000	216.650	15473.8

Pr	γ	$R_g\,[\text{J}/(\text{kg K})]$	$\mu_{\text{ref}}\,[\text{kg}/(\text{m s})]$	$T_{\text{ref}}\,[\text{K}]$	$S\,[\text{K}]$
0.72	1.4	287.058	1.716×10^{-5}	273.15	110.6

2.2 Base-Flow Quantification

To properly study the disturbances in a given flow, a high-quality representation of the laminar base-flow without these perturbations must first be obtained. In order to obtain this base flow, two distinct methods are utilized.

In the first method, the basic-state data is calculated using the OVERFLOW 2.2n computational fluid dynamics solver which solves the full, steady Navier-Stokes equations [20]. These solutions are generated and provided to Texas A&M by Dr. James Coder from the University of Tennessee, Knoxville. In order to model the laminar boundary-layer development within OVERFLOW as realistically as possible, a transition model must be used. Fully laminar solutions often lead to flow separation near the trailing edge, which in turn leads to a large deviation in the pressure distribution from the realistic behavior upstream of the transition location. On the other hand, fully turbulent simulations are not viable in order to study the stability of the laminar flow. To avoid the issues that arise from using a fully laminar or fully turbulent solution, the AFT2019b transition model is implemented [21]. This transition model is not used to induce laminar-to-turbulent transition realistically, but rather to provide a numerical model of the realistic surface-pressure distribution without contaminating the boundary layer. Once a converged solution is reached and received by the CST Lab, this data is extracted using TecPlot and an in-house data-extraction tool, detailed in Travis Kocian's dissertation [22]. This tool interpolates the base-flow data onto a wall-normal, orthogonal coordinate system.

OVERFLOW solves the full, steady Navier-Stokes equations, making it a time intensive and memory intensive tool. Although the OVERFLOW solutions have been deemed converged from the stand point of the basic-state flow variables, stability calculations are known to be very sensitive to details of the basic state. In order to perform further detailed grid resolution studies and parameter uncertainty checks in a reasonable time frame, the inviscid pressure distributions from the OVERFLOW solutions are extracted and coupled with the boundary-layer solver, DEKAF (Digits by Ethan, Koen, Alex, and Fernando) [23].

DEKAF solves the boundary-layer equations, instead of the full, steady Navier-Stokes equations, which allows for much faster simulations and increased grid resolutions. The boundary-layer equations use the assumption that the boundary-layer is thin to simplify the momentum and energy equations. The term δ is used to represent the boundary-layer height and s is the leading-edge-orthogonal surface distance. Applying the order of magnitude analysis directly to the mass conti-

nuity equation leads to $\frac{\partial}{\partial s} \ll \frac{\partial}{\partial y}$. This condition is violated near the flow's attachment line, where gradients in s are typically large. Additionally, if the flow separates, $\frac{\partial}{\partial s}$ becomes comparable to $\frac{\partial}{\partial y}$, while the boundary-layer height is still small with respect to s, violating the boundary-layer assumption [15][18]. In areas where flow separation occurs, DEKAF is unable to be run due to the parabolic flow assumption inherent in the boundary-layer approximation. These two situations lead to discrepancies relative to the full, steady Navier-Stokes solutions near these regions of interest.

For the sake of this study, DEKAF is being implemented in two different ways. *One*, an OVERFLOW solution is obtained on a swept-wing case and the inviscid pressure distribution is taken directly from that solution and put into the DEKAF boundary-layer solver. This approach will be referred to as DEKAF$^{\mathrm{s}}$, where "s" corresponds to a *s*wept pressure distribution. *Two*, an OVERFLOW solution can be obtained on an unswept wing, and the unswept inviscid pressure distribution can be input into DEKAF and swept internally. This approach will be referred to as DEKAF$^{\mathrm{u}}$, where "u" corresponds to an *un*swept pressure distribution. In the latter approach, a freestream spanwise velocity component is imposed within DEKAF based on the freestream Mach number, sweep angle, and angle of attack. Using this method minimizes the number of OVERFLOW solutions required in order to perform sweep variation analysis.

Comparing results obtained through these different approaches will give valuable insight into the validity of each method. DEKAF can be run with extremely high resolutions due to the assumptions made and therefore can be used to verify that the OVERFLOW solution is fully converged. On the other hand, OVERFLOW verifies that the assumptions made in the development of the boundary-layer equations, used in DEKAF, have negligible effects on the results over the majority of the chord, and hence on transition prediction.

2.3 Flow Stability

In order to accurately model and study transitional flows, numerical approaches based on stability methods and perturbation theory are used. The basic concept behind this idea is fairly simple, all flow variables (ϕ) are decomposed into their steady, laminar, unperturbed, base-flow component

($\bar{\phi}$), and the perturbations which act on this base-flow (ϕ').

$$\phi(s,y,z,t) = \overline{\phi}(s,y,z) + \phi'(s,y,z,t) \tag{2.8}$$
$$\phi = [u,v,w,T,\rho]^T$$

If these perturbations are damped out by their interaction with the boundary layer, the flow is considered stable. On the contrary, if these perturbations are amplified by the boundary layer, the flow is said to be unstable. Stability methods study the development of these perturbations once they have already entered the flow. Each stability method imposes a different solution form of ϕ.

Substituting the general perturbation equation, Equation 2.8, into the governing equations leads to three distinct kinds of terms: base-flow, linear perturbation, and non-linear terms. The base-flow terms are required to satisfy the governing equations and for linear approaches the non-linear terms are assumed to be negligible, due to the minute amplitude of the perturbations in question. The two stability methods discussed below and implemented in this study are linear stability methods, and therefore neglect these non-linear terms. The resulting equations, for the sake of this paper, are referred to as the linearized Navier-Stokes equations.

2.3.1 Linear Stability Theory

Linear Stability Theory (LST) is the simplest and most commonly used approximation method for stability analysis.

LST assumes that the flow is locally parallel, meaning that the base-flow quantities are functions of wall-normal direction only, and as a consequence of the continuity equation for the laminar base flow, the wall-normal velocity is equal to zero. Additionally, linear stability theory imposes that the shape of the perturbation is general with respect to the wall-normal direction. The constant base-flow variables in the other spatial directions and time, allow imposing a complex exponential function of those directions and time [7][9][11][22]. This decomposition of the perturbation is

represented as a shape function and wave and is seen in Equation 2.9.

$$\phi'(s,y,z,t) = \underbrace{\hat{\phi}(y)}_{\text{shape}} \underbrace{e^{i(\alpha s+\beta z-\omega t)}}_{\text{wave}} + c.c. \tag{2.9}$$

Assuming frequency, ω, is real, values for ω and the complex spanwise wavenumber, β, are specified in order to solve for the complex streamwise wavenumber, α. This approach is referred to as spatial LST. It is also possible to specify values for the real spanwise wavenumber and real streamwise wavenumber, in order to solve for the complex frequency. This approach is referred to as temporal LST. The wing is modeled to be spanwise infinite, and therefore growth in the spanwise direction is set to be zero, making $\beta_i = 0$. Two quantities that represent the physical characteristics of the disturbance include the wave angle and phase speed:

$$\psi_w = \arctan\left(\frac{\beta_r}{\alpha_r}\right) \qquad \text{and} \qquad c_{ph} = \frac{\omega}{\sqrt{\alpha_r^2 + \beta_r^2}} \tag{2.10}$$

The LST perturbation ansatz, seen in Equation 2.9, is substituted into the linearized Navier-Stokes equations in order to study the development of these disturbances. Once the LST assumptions are implemented, a single matrix representation of the system of individual disturbance equations can be represented as follows.

$$\mathcal{A}\frac{\mathrm{d}^2\hat{\phi}}{\mathrm{d}y^2} + \mathcal{B}\frac{\mathrm{d}\hat{\phi}}{\mathrm{d}y} + \mathcal{C}\hat{\phi} = 0 \tag{2.11}$$

Here $\mathcal{A}, \mathcal{B}$, and $\mathcal{C}$ are a set of (5×5) matrices, containing only linear terms for each wall-normal point. These equations are fully expanded and presented in Appendix B.2. Applying boundary conditions to the first and last wall-normal grid points, sets up a system which can be solved for the complex eigenvalue α. Since the system presented in Equation 2.11 and Appendix B.2 contains

quadratic terms with respect to α, this eigenvector is expanded to the form seen in Equation 2.12.

$$\hat{\Phi} = \begin{bmatrix} \hat{u} \\ \hat{v} \\ \hat{w} \\ \hat{T} \\ \hat{\rho} \\ \alpha\hat{u} \\ \alpha\hat{v} \\ \alpha\hat{w} \\ \alpha\hat{T} \end{bmatrix} \tag{2.12}$$

This companion-matrix leads to the linear generalized eigenvalue problem:

$$\mathbf{A}\hat{\Phi} = \alpha\mathbf{B}\hat{\Phi} \tag{2.13}$$

where **A** and **B** are $(9N_y \times 9N_y)$ matrices and $\hat{\Phi}$ is a $(9N_y \times 1)$ vector. This eigenvalue problem is solved using the iterative Arnoldi method [24]. This method returns a multitude of eigenmodes, of which only one eigenmode represents the disturbance of interest. To ease in mode selection, filtering based on physical characteristics of the eigenmode, such phase speed and wave angle, is applied.

2.3.2 Linear Parabolized Stability Equations

The Linear Parabolized Stability Equations (LPSE) improve upon the LST approach by accounting for small variations of the base flow in the streamwise direction. The derivation of LPSE is similar to that for LST. The total flow is decomposed into a basic state plus a perturbation, and asserts that the basic state is a solution to the equations of motion. The difference between the two methods lies in the assumptions taken. While LST assumes a parallel flow, LPSE alleviates this parallel flow assumption and becomes a marching solution which incorporates the upstream his-

tory of the disturbance. In order to do this, the flow quantities are assumed to be "slowly varying", represented with a $\sim$, in the streamwise direction. This is accomplished by defining $\frac{\partial}{\partial \tilde{s}} \equiv \epsilon_s \frac{\partial}{\partial s}$. This slowly varying assumption in turn removes all $\frac{\partial^2}{\partial s^2}$ terms from the equations. Additionally, as in LST, the flow is assumed to be spanwise invariant. These assumptions lead to a perturbation ansatz modeled as the product of a slowly varying shape function and a rapidly varying wave function, as seen in Equation 2.14. This equation includes an $\alpha(\tilde{s})$ term which is the slowly varying complex streamwise wavenumber.

$$\phi'(s,y,z,t) = \underbrace{\hat{\phi}(\tilde{s},y)}_{\text{shape}} \underbrace{e^{i(\int^{\tilde{s}} \alpha(\bar{s})\mathrm{d}\bar{s} + \beta z - \omega t)}}_{\text{wave}} + c.c. \tag{2.14}$$

Substituting the LPSE disturbance equation into the equations for mass, momentum, and energy, and neglecting all $\frac{\partial^2}{\partial s^2}$ derivatives as explained above, results in the LPSE stability equations.

$$\mathcal{A}\frac{\partial^2 \hat{\phi}}{\partial y^2} + \mathcal{B}\frac{\partial^2 \hat{\phi}}{\partial \tilde{s} \partial y} + \mathcal{C}\frac{\partial \hat{\phi}}{\partial y} + \mathcal{D}\frac{\partial \hat{\phi}}{\partial \tilde{s}} + \mathcal{E}\hat{\phi} = 0 \tag{2.15}$$

$\mathcal{A}$, $\mathcal{B}$, $\mathcal{C}$, $\mathcal{D}$, and $\mathcal{E}$ are (5 $\times$ 5) linear matrices and $\alpha(\tilde{s})$ is determined iteratively for each LPSE marching step. It is worth noting that $\mathcal{A}$, $\mathcal{B}$, and $\mathcal{C}$ in the LPSE equations are not equal to those in Equation 2.11. These equations, fully expanded, are presented in Appendix B.3. Unlike LST, LPSE is not formulated as an eigenvalue problem, but rather an initial value problem. In order to solve LPSE, a shape function obtained through the LST method can be introduced. Once this LPSE solution is deemed converged, it is marched downstream in the surface coordinate, s. Per LPSE step, α is updated by converging upon the auxiliary condition defined below.

$$\alpha^{k+1} = \alpha^k - \mathrm{i} \left(\sum_{\hat{\phi} \in \{\hat{u},\hat{v},\ldots,\hat{\rho}\}} \int_0^{y_{\max}} \hat{\phi}^\dagger \cdot \frac{\partial \hat{\phi}}{\partial \tilde{s}} \, \mathrm{d}y \Big/ \sum_{\hat{\phi} \in \{\hat{u},\hat{v},\ldots,\hat{\rho}\}} \int_0^{y_{\max}} |\hat{\phi}|^2 \mathrm{d}y \right) \tag{2.16}$$

This condition removes the ambiguity in growth distribution between the shape function and wave amplitude by minimizing the streamwise growth of the shape functions. This condition is necessary in order to absorb the exponential growth into the fast-varying wave function, while retaining slow

streamwise variation of the shape function $\hat{\phi}$ required for the LPSE assumptions.

2.4 Applying Stability Theory

In order to solve the LST and LPSE equations, I am using the Euonymous Parabolized Instability Code, EPIC, as described in Nick Oliviero's Masters Thesis [22][25][26][27]. EPIC solves spatial LST and LPSE for input real frequencies (ω) and real spanwise wavenumbers (β) in order to obtain the streamwise perturbation growth rates. Stability results obtained using EPIC, specifically those solving LST, have been verified against those calculated with VESTA (the VKI Extensible Stability and Transition Analysis toolkit) and the in-house stability code of the Delft University of Technology, as detailed in Groot et al. [23]. Within EPIC, the following boundary conditions are implemented for the stability problem:

$$\hat{\phi}_\infty = 0, \qquad \hat{u}_w = \hat{v}_w = \hat{w}_w = 0,$$

where the subscript w corresponds to values evaluated at the wall, and ∞ is the boundary value at $y = y_{max}$. The condition at the freestream boundary is imposed for all eigenfunctions contained within $\hat{\phi}$. A Dirichlet condition, $\hat{T}_w = 0$, is used for the temperature at the wall. It is common to use an adiabatic wall condition for stationary crossflow, but for the purpose of this study this is neglected, as its effects on the N-factor are found to negligible in the context of the present problem. The y-momentum equation is used as a compatibility equation for $\hat{\rho}$ at the wall.

As stated in Section 2.3.2, in order to initialize LPSE, an LST solution for each real (ω, β) pair must first be obtained. To solve the LST generalized eigenvalue problem, Equation 2.13, the iterative Arnoldi algorithm is implemented for a single frequency and spanwise wavenumber [24]. The obtained eigensolution is then converged further using a Newton-Raphson procedure to a tolerance specified by the user. The Newton-Raphson technique is then used to obtain eigensolutions for subsequent wavenumbers and frequencies. These operations are both performed up to a tolerance of $O(10^{-11})$. This tolerance refers to the sum of the absolute value of the right-hand side forcing vector driving the Newton-Raphson algorithm, as detailed in Moyes et al. [28].

Before LPSE can be initialized, a reasonable initial s-location must be determined. This s-location must be far enough upstream to properly capture all the growth in the system. This location is determined as follows:

First, a streamwise location is selected at which, ideally, the LST eigenmode for the prescribed values of ω and β is unstable. This can sometimes prove to be challenging. If an unstable eigenmode is not found, the mode is selected based on specific physical characteristics of the eigenmode in question, such as phase speed and wave angle. Next, this LST eigenmode is marched upstream in s using the Newton-Raphson approach until it reaches the most upstream location where the selected solution displays neutral growth within the context of the LST approach. This s-location is also referred to as the LST branch-I neutral-point, and is denoted by s_{I}. It should be noted that this neutral-point location does not take into account the non-parallel effects present in LPSE. To account for these non-parallel effects, LPSE is not initialized at the LST branch-I neutral point location, but rather upstream of it. The LST solution is marched, at minimum, an additional 4 steps upstream of its neutral point. This upstream s-station and the corresponding LST solution are used to initialize LPSE. This approach is repeated for the remaining input (ω, β) pairs. Rather than specifying a streamwise starting location for each pair, the LST neutral point for the previous (ω, β) combination is used. If no LST neutral point existed for the previous (ω, β) pair, the starting location of the Newton-Raphson marching approach for this previous pair is used. This process is repeated until all (ω, β) combinations are accounted for.

Once LPSE has been properly initialized, the auxiliary condition laid out in Equation 2.16 is evaluated in order to update the eigenvalue α. Using this new value for α, a correction in the shape functions is determined. This process is repeated until a tolerance of $O(10^{-11})$ is obtained for the absolute value of α. After reaching this convergence criterion, an s-step is made. This process is repeated for all s-nodes, determining the perturbation evolution for the complete chord.

2.5 Analyzing the Results

Once the perturbation growth rates have been obtained using the LPSE approach, the amplification of these perturbations will be presented by the N-factor. The N-factor, commonly referred

to as the "amplification factor", is an integrated measure of growth corresponding to a disturbance of a given frequency and spanwise wavenumber. For LST solutions, the imaginary part of the eigenvalue, α_i, contains all of the streamwise growth of the instability. LPSE solutions additionally contain a small portion of the streamwise growth in the perturbation shape function. In order to capture the total streamwise growth for the LPSE solutions, the Chu-norm [29], $\Phi(s)$, is utilized. This norm calculates the total perturbation energy in the shape functions, leading to the expression below for N-factor:

$$N(s) = \int_{s_{\mathrm{I,LPSE}}}^{s} -\gamma_i(\overline{s})\,\mathrm{d}\overline{s}, \qquad \gamma(\tilde{s}) = \alpha - \frac{\mathrm{i}}{\Phi}\frac{\partial \Phi}{\partial \tilde{s}},$$

$$|\Phi(s)|^2 = \int_0^{y_{\max}} \left(\overline{\rho}(|\hat{u}|^2 + |\hat{v}|^2 + |\hat{w}|^2) + \frac{\overline{\rho}}{\gamma(\gamma-1)\mathrm{M}^2\,\overline{T}}|\hat{T}|^2 + \frac{\overline{T}}{\gamma \mathrm{M}^2\,\overline{\rho}}|\hat{\rho}|^2 \right) \mathrm{d}y$$

Here, $s_{\mathrm{I,LPSE}}$ represents the s-location of the LPSE neutral point (i.e. the location where $\gamma_i = 0$). A subscript i denotes the imaginary part. Additionally in the Chu-norm, M is defined as $\overline{u}$ divided by the speed of sound, $\overline{a}$, at the edge of the domain, at the first s station of the input base flow. This M definition is chosen because it has the same nondimensionalization scale used internally with EPIC. Integration in both y and s are performed using the trapezoidal rule.

Calculating this N-factor for a complete range of frequencies and wavelengths gives a maximum amplification factor for all s-locations, creating an N-factor envelope. When analyzing N-factor envelopes, knowing the critical N-factor values for the present instability mechanisms is necessary. A critical N-factor is the N-factor value above which the flow is expected to transition to turbulence as a consequence of the instability mechanism in question. Tollmien-Schlichting-induced transition is anticipated near an N-factor value of 9 units [30][31]. Additionally, stationary-crossflow-induced transition has been seen for LPSE N-factors as low as 5 units [32]. There has not yet been a good foundation for a critical N-factor value corresponding to traveling crossflow. Therefore, without further information of the disturbance environment, roughness, and freestream turbulence, a conservative critical N-factor value of 5 is used for traveling-crossflow disturbances as well. These unique critical N-factor values are only directly viable when a single instability is

present, as it neglects any interaction between instability mechanisms. This interaction can diminish the allowable maximum N-factor for sustained laminar flow and will be discussed further in the results section below.

By comparing the N-factor envelopes to the critical N-factor values, I will be able to define a range for allowable sweep angles and angles of attack for this SNLF airfoil. It should be noted that the critical N-factor is only directly valid if the disturbance environment is consistent with that of the experiment in which these values were obtained. Therefore, a factor of safety should be implemented when comparing the maximum N-factor achieved by an instability mechanism to its respective critical value.

3. STABILITY RESULTS

In what follows, the convergence of the linear stability results and the stability results themselves for the fore element of the S207 airfoil will be discussed.

3.1 Discretization of the (ω, β) Space

As stated previously, the focus of this study is to accurately capture the streamwise amplification of waves with an imposed frequency and wavelength in the leading-edge-parallel direction. These imposed quantities remain fixed while marching downstream. In high-subsonic-speed regimes, the most unstable perturbations typically have a frequency in the kilohertz range, whether this be TS or CF driven [7][33]. Additionally, the most-amplified wavelength for crossflow vortices is typically approximately equal to four times the boundary-layer height [34]. These frequency and wavelength ranges have been discretized and distributed among multiple groups as illustrated in Figure 3.1. The numerical values of these quantities are listed in tables 3.1 and 3.2; the positive and negative values have equal magnitudes. This discretization process was developed while working with the precursor airfoil, the X207.o, as detailed in Groot et al. [19], and is described as follows.

Due to the complex perturbation quantities $\{\alpha, \omega, \beta, \hat{\phi}\}$ present in the perturbation equations, Equations 2.9 and 2.14, a symmetry exists in the (ω, β) parameter space. [1] This symmetry means that all of the unique solutions exist in only half of the (ω, β)-plane. Any half of the plane can be chosen, but for the purpose of this study only positive ω-values are being considered. A positive ω value results in solution propagation in the direction of $\vec{k} = [\alpha, \beta]$. Using this convention, a positive

[1] As detailed in Koen Groot's dissertation [35], when the complex perturbation quantities $\{\alpha, \omega, \beta; \hat{\phi}\}$ are replaced by their complex conjugates (with appropriate change of sign) as follows:

$$\alpha \Rightarrow -\alpha^{\dagger}, \qquad \beta \Rightarrow -\beta^{\dagger}, \qquad \omega \Rightarrow -\omega^{\dagger}, \qquad \hat{\phi} \Rightarrow \hat{\phi}^{\dagger} \tag{3.1}$$

the solution corresponding to $\{-\alpha^{\dagger}, -\omega^{\dagger}, -\beta^{\dagger}; \hat{\phi}^{\dagger}\}$ represents an identical solution. This is explained as follows. Since ω and β are imposed to be real values, taking the complex conjugate of these values simply results in flipping the signs, i.e. a reflection about the origin of the (ω, β)-plane. Additionally, $\vec{k} = [\alpha, \beta]$ contains the direction of the wave propagation, seen in Equation 2.10. The above operation flips the direction of this wave vector, $-\vec{k}^{\dagger} = [-\alpha^{\dagger}, -\beta^{\dagger}]$. The opposite sign on the real part of $-\omega^{\dagger}$ implies that the solution $\{-\alpha^{\dagger}, -\omega^{\dagger}, -\beta^{\dagger}; \hat{\phi}^{\dagger}\}$ propagates in the direction opposite to $-\vec{k}^{\dagger}$, thereby marching in the same direction as $\{\alpha, \omega, \beta; \hat{\phi}\}$. In summation, when reflecting about the origin of the (ω, β)-plane, identical solutions are obtained.

Table 3.1: Complete list of the input frequencies ω, in $[\mathrm{Hz}]$.

0	162	288	450	648	882	1017	1152	1303
1458	1801	2179	2593	3043	3529	4051	4609	5204
5843	6500	6725	7328	7957	8612	9293	10000	

Table 3.2: Complete list of the (magnitude of the) input wavelengths $\lambda = 2\pi/\beta$, in $[\mathrm{mm}]$.

2.412	2.736	3.113	3.556	4.075	4.689	5.417	6.285	7.325
8.578	10.098	11.953	14.232	17.053	20.572	25.000	27.121	31.196
36.028	41.786	48.685	56.997	67.071	79.359	94.451	∞	

(negative) β corresponds to propagation in the positive (negative) z-direction; where the positive z-axis points to the wing tip on the top side of the airfoil and the wing root on the bottom side of the airfoil. A solution with $\beta = 0$ represents a wave propagating in the leading-edge-orthogonal direction.

The discretization of this positive ω portion of the (ω, β)-space is broken down into 4 subspaces, denoted by I(a), I(b), II(a), and II(b). The subspaces I(a) and II(a) have an overlap on the β-axis ($\omega = 0$) and the subspaces I(b) and II(b) have an overlap on the ω-axis ($\beta = 0$ or $\lambda = \infty$).

The distinction between (a) and (b) subspaces is due to the different contained axes and the slightly different computational approaches required to properly obtain stability results in these domains:

First, different resolutions are required to obtain converged stability results within these subspaces. The baselines resolutions required are $N_s = 750$ and $N_y = 200$ for the (a)-subset and $N_s = 150$ and $N_y = 150$ for the (b)-subset. Here, N_s and N_y represent the number of grid points in the stability domain in the leading-edge-orthogonal and wall-normal directions, respectively. Section 3.2 will demonstrate that these resolutions lead to converged stability solutions for their respective (ω, β)-subspaces.

Second, stability calculations were performed on different portions of the s-domain. In order to completely capture the growth due to stationary crossflow, contained within (ω, β)-subspaces I(a)

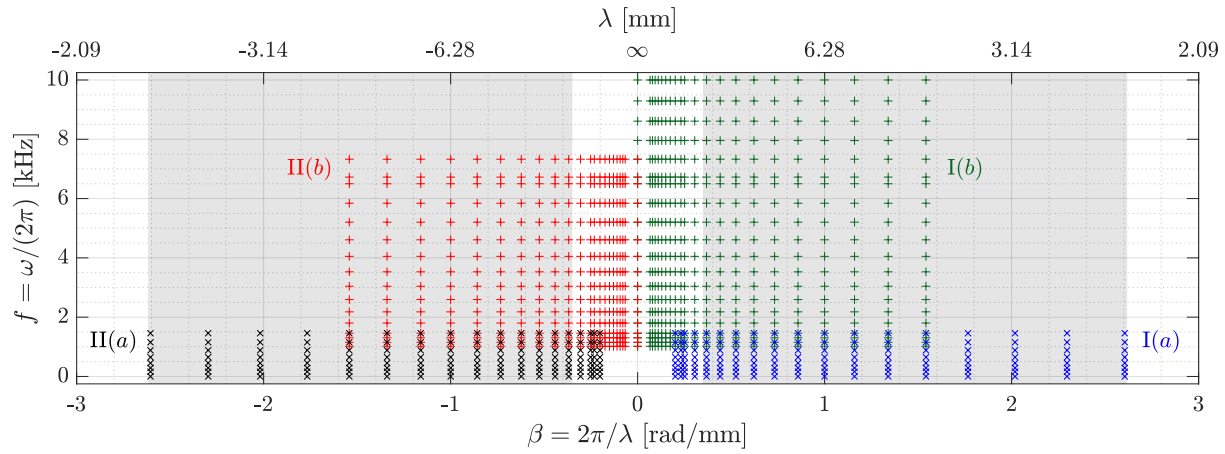

Figure 3.1: Definitions of the (ω, β) subspaces. Wavelength ranges that are typically associated with crossflow vortices ($4\delta_{99}$, accounting for δ_{99} variation beyond x/c of 2%) are indicated with grey patches.

and II(a), stability calculations must be initiated as close to the attachment line as possible, within the computational restrictions. The s-location at which LPSE is initialized can have a significant impact on the resulting N-factors for the stationary crossflow disturbance, as shown in Groot et al. [17].

Third, the order in which the (ω, β)-pairs are run varies between the two subspaces. For the (a)-subset, the Newton-Raphson approach for the LST solution is initiated from the largest wavenumber on the β-axis, i.e. the stationary disturbance with the smallest wavelength. For the (b)-subset, the Newton-Raphson approach for the LST solutions is initiated from the highest frequency on the ω-axis, i.e. the highest frequency spanwise-infinite disturbance.

The distinction between I and II subspaces is made to denote the first ($\beta > 0$) and second ($\beta < 0$) quadrants of the (ω, β)-space. Unstable, traveling crossflow content can propagate both in the direction of and opposite to that of the crossflow velocity component of the base flow, $\bar{w}_s$. As stated in Mack [7]:

> [...] there are two groups of positive unstable frequencies with quite different wave angles. The first group, which includes the peak amplification rate, is oriented anywhere from 5° to 31° (clockwise) from the direction opposite to the crossflow direction. The

second group is oriented close to the crossflow direction itself.

Rather than looking at only one quadrant, in order to capture all of the unstable content, stability calculations must be performed on both quadrants I and II due to these two different wave-angle groups. Additionally, this means that the most unstable traveling crossflow disturbances are anticipated to propagate, in terms of phase speed, in the direction *opposite* of the crossflow velocity component.

3.2 Stability Convergence Analysis

In order to ensure that the stability results are reliable, stability convergence and verification studies are performed. The convergence study is performed by demonstrating that the results presented are independent of the used resolution for the stability problem. Showing that the stability results derived from different base-flow solutions (DEKAF and OVERFLOW) yield similar results verifies both the solution and the approach. Comparisons between the stability solutions obtained on base-flow solutions corresponding to DEKAF on an OVERFLOW-swept pressure distribution (DEKAF$^{\text{s}}$) and an internally-swept pressure distribution (DEKAF$^{\text{u}}$) will also be presented.

These studies were conducted on the $\Lambda = 15^\circ$ sweep case, with an $\alpha = -1.520^\circ$ angle of attack. This angle of attack yields the design section-lift coefficient, and this sweep angle will be demonstrated to be of primary interest in what follows. In order to present these results more clearly, only the N-factor envelopes are shown, rather than "N-curves" that correspond to individual (ω, β) combinations. These N-factor envelopes are shown in Figure 3.2.

As stated above, low-frequency content (contained in subspaces I(a) and II(a)) is more difficult to converge, and therefore require a higher resolution. In particular, a baseline resolution of N_s = 750 and N_y = 200 was used for the (a)-subspaces and N_s = 150 and N_y = 150 was used for the (b)-subspaces. The required resolution for low-frequency content is larger because these solutions must be obtained very close to the attachment line, where streamwise gradients are large. To show that these solutions are converged, the number of leading-edge-orthogonal and wall-normal stability grid points were varied independently with respect to the baseline resolution, and resulting N-factor envelopes were compared. The envelopes corresponding to different resolutions are indi-

cated with different symbols. For the majority of the chord, all of these different resolutions lie on top of each other; N-factor errors are smaller than 0.15 everywhere. This result applies to both the top and bottom sides of the airfoil, as well as all of the (ω, β)-subspaces, and is argued to be small enough for the purpose of this study.

Now that it is determined that the results are converged in terms of the resolution used to solve the stability problem, we compare the results obtained using the different representations of the base flow (OVERFLOW, DEKAF$^{\mathrm{s}}$, and DEKAF$^{\mathrm{u}}$). N-factor envelopes corresponding to the OVERFLOW, DEKAF$^{\mathrm{s}}$, and DEKAF$^{\mathrm{u}}$ solutions are represented by dashed, dotted, and solid lines, respectively. As seen in Figure 3.2, the N-factor differences corresponding to the three different base-flow solutions are also very small; N-factor errors smaller than 0.15 for the entirety of the chord.

Now that a proper resolution has been identified and the stability results are shown to be independent of the base flow used, the remainder of the computed data will be based on the DEKAF$^{\mathrm{u}}$ base flow, using the baseline resolutions defined above. This base flow was chosen to ease the sweep-angle variation study, as described in Section 2.2.

3.3 Sweep Variation Analysis for Design Angle of Attack, $\alpha = -1.520^\circ$

In order to gain a better understanding of the effects of sweep on the amplification rates, a sweep-variation study was performed on a wide range of sweep angles, while fixing the angle of attack to the value corresponding to the design-section-lift coefficient ($c_l \approx 0.65$ and $\alpha = -1.520^\circ$). Using the baseline resolutions for the stability problem determined in Section 3.2 ($N_s = 750$ and $N_y = 200$ for low-frequency content and $N_s = 150$ and $N_y = 150$ for high-frequency content), N-factor envelopes were developed for sweep angles ranging from 0° to 30° in 5° increments. All of the stability results presented in this section are computed using the DEKAF^{u} base flow solutions and are seen in Figure 3.3.

Figure 3.3 contains a number of different N-factor envelopes. The red dashed lines correspond to the maximum overall N-factor achieved over the total frequency and wavelength domain. The blue lines correspond to the stationary crossflow envelopes. Stationary crossflow corresponds to

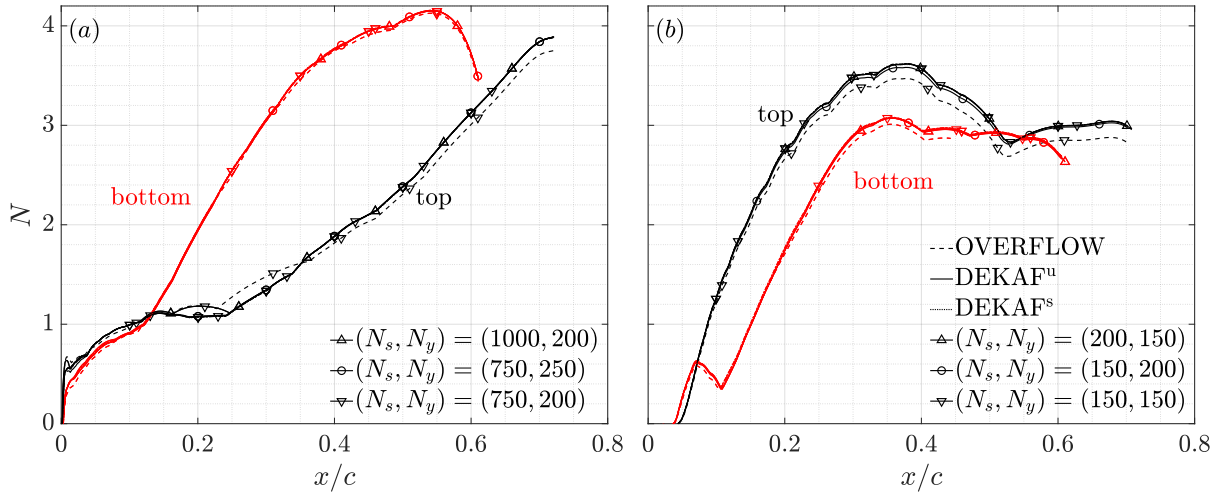

Figure 3.2: Comparisons of the N-factor envelopes (composed of individual N-curves for a broad range of frequencies and wavelengths) for $\Lambda = 15°$ and the design angle of attack $\alpha = -1.520°$ ($c_l \approx 0.65$), as computed using the DEKAF and OVERFLOW base-flow solutions and with different resolutions for the stability problem. Low-frequency content is pictured on the left (panel a), while high-frequency content is on the right (panel b).

solutions with a frequency of 0 Hz. The traveling crossflow and Tollmien-Schlichting envelopes are more difficult to distinguish, as they span a variety of different frequency and wavelength combinations. In order to tackle this challenge, the characteristics of the disturbances attained must be considered and include:

$$c_{\text{ph}} = \frac{\omega}{\sqrt{\alpha_r^2 + \beta^2}}, \quad \psi_w = \arctan\left(\frac{\beta}{\alpha_r}\right), \quad \psi_s = \arctan\left(\frac{\overline{w}_0}{\overline{u}_e}\right), \quad f = \frac{\omega}{2\pi}, \quad \lambda = \frac{2\pi}{\sqrt{\alpha_r^2 + \beta^2}}$$

which are the phase speed, c_{ph}, wave angle, ψ_w, streamline angle, ψ_s, frequency, f, and wavelength in the direction of the wave vector, λ, of the disturbance. The subscript r indicates the real part. The wave and streamline angles are zero if the wave vector and streamline are oriented in the leading-edge-orthogonal direction. Note that the wave propagates towards the wing tip (root) on the top (bottom) side of the airfoil for wave angles $0° < \psi_w < 180°$.

The typical characteristics of the traveling crossflow instability are as follows:

1. The most unstable wavelength in the direction of the wave vector, λ is on the order of 4 boundary-layer thicknesses, $4\delta_{99}$;

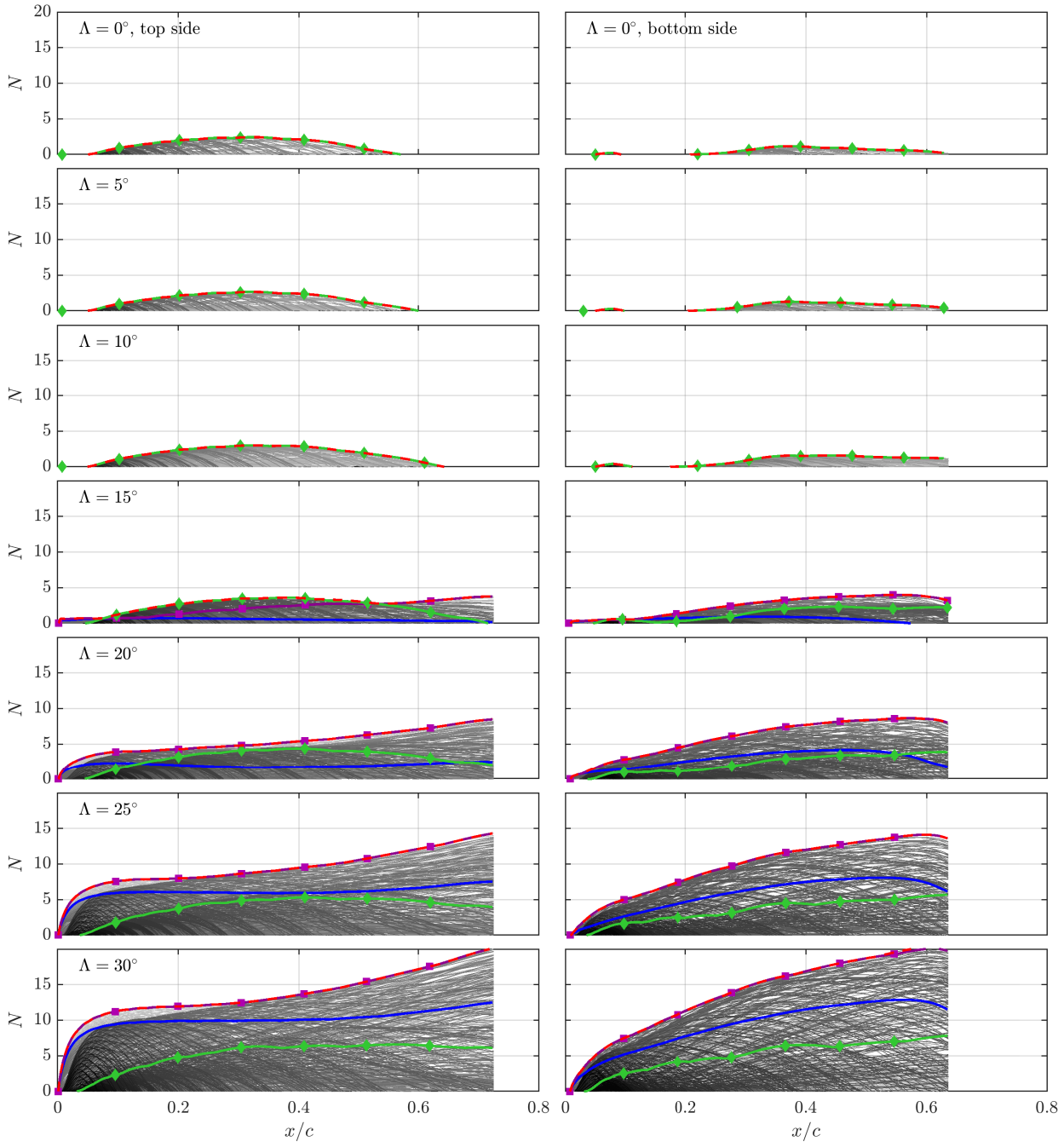

Figure 3.3: N-factor envelopes representing the overall maximum values (dashed red lines), the Tollmien-Schlichting mechanism (green), the traveling crossflow mechanism (purple), and the stationary crossflow mechanism (blue) for the angle of attack, $\alpha = -1.520°$. The grey lines represent individual wavenumber and frequency combinations.

2. The phase speed is small with respect to $\overline{u}_{s,e}$, but is on the order of $\overline{w}_{s,max}$;
3. The wave angle is oriented near ($\approx \pm 15^{\circ}$) the crossflow direction, or from 5° to 31° (clockwise) from the direction opposite to the crossflow direction;
4. The frequency is typically in the range of 400 to 1500 Hz.

Tollmien-Schlichting content, on the other hand, is slightly more difficult to define. The TS mechanism is typically described as a 'streamwise' mechanism, meaning that the wave angle (ψ_w) and streamline angle (ψ_s) are oriented near one another. Additionally, it is observed that the phase speed is approximately 20-40% of the edge velocity in the streamline direction: $c_{\mathrm{ph}}/\overline{u}_{s,e} \approx 0.20 - 0.40$.

In order to define envelopes for the Tollmien-Schlichting and traveling crossflow mechanisms, the orientation of the wave angle with respect to the streamline angle, as well as the impact of pressure gradient is used. Recall that a favorable pressure gradient is stabilizing for TS and a minimized pressure gradient magnitude (and minimized sweep angle) is stabilizing for crossflow.

Traveling crossflow is determined to be content which at any point along the chord $||\psi_w - \psi_s| - 90^{\circ}| \leq 15^{\circ}$, i.e. the wave angle is oriented near (opposite) the crossflow direction. This angle selection is verified and visualized in Sections 3.4 and 3.5 where it is shown that increasing the magnitude of the pressure gradient destabilized this content. The Tollmien-Schlichting mechanism is determined to be present when at any point along the chord, $|\psi_w - \psi_s| \leq 65^{\circ}$. Although this angle is relatively high, all of the content attained using this parameter follows the anticipated trends for the effect of pressure gradient on TS. This value also aligns well with findings by Rozendaal, in which the most unstable relative wave angle for the streamwise disturbance was approximately 40° to 60° on a transonic swept wing case [11][36][37][38]. The verification and visualization of this angle selection is presented in Sections 3.4 and 3.5. The maximum N-factor envelopes of each mechanism, developed with the aforementioned criteria, combine to form the overall maximum N-factor envelope for the total chord. It is interesting to note, that these are two distinct relative wave-angle groups. Disturbances which have relative wave angles between 65° and 75° never define the overall maximum N-factor. In order to further verify that these solutions correspond to

Table 3.3: Parameters characterizing the most amplified disturbances as presented in Figure 3.3, considering the design angle of attack ($\alpha = -1.520°$). The purple text represents characteristics expected for the traveling cross mechanism, and green text represents characteristics expected for TS. All calculations were performed on the DEKAF^u base flow data set. The complete lists of ψ_w and ψ_s for these cases is presented in table C.1 within Appendix C.

side,	Λ [°]	$N_{\max}$	$4\delta_{99}$ [mm]	λ [mm]	f [Hz]	$c_{\mathrm{ph}}/\overline{u}_{s,e}$	$c_{\mathrm{ph}}/\lvert\overline{w}_{s,\max}\rvert$	$\psi_w - \psi_s$ [°]
top,	0	2.4	10.77	32.1	2593	0.3057	∞	+23.87
	5	2.7	10.69	29.6	2593	0.2810	68.79	+33.61
	10	3.0	10.77	29.0	2593	0.2733	33.46	+36.32
	15	3.8	14.97	20.5	648	0.0429	1.95	+83.11
	20	8.5	14.99	16.9	648	0.0348	1.19	+84.30
	25	14.3	15.02	16.7	648	0.0338	0.93	+84.28
	30	20.2	15.07	16.5	882	0.0445	1.03	+82.81
bottom,	0	1.2	11.16	34.7	2179	0.3174	∞	0.00
	5	1.3	11.16	32.9	2179	0.2999	55.88	−20.19
	10	1.6	12.21	34.7	1801	0.2540	22.23	−37.00
	15	4.0	13.42	16.9	648	0.0430	2.42	−84.12
	20	8.7	13.61	13.9	648	0.0346	1.48	−85.30
	25	14.1	13.92	13.7	648	0.0329	1.14	−85.37
	30	20.3	14.11	13.4	882	0.0425	1.25	−84.23

the expected instability mechanisms, the characteristics of the maximum perturbation for each side and sweep angle is extracted and presented in table 3.3

Using this data, a reasonable reference sweep angle for which laminar flow is possible is determined for further analysis. To define this reference angle, the N-factors obtained for the various sweep angles will be compared against the critical N-factors for the Tollmien-Schlichting ($N = 9$) and crossflow ($N = 5$) mechanisms, as detailed in Section 2.5. Comparing the stationary crossflow envelopes (blue lines) to the critical N-factor of 5 immediately discredits sweep angles $\Lambda \geq 25°$ from further consideration as laminar flow is not expected to be maintained on the airfoil for these sweep angles. The $\Lambda = 20°$ case is the first sweep angle for which the maximum N-factor obtained for stationary crossflow does not exceed 5 units. Therefore, this case must be further examined to determine the most amplified instability mechanism. Using the characteristics laid out in table 3.3, the most unstable mode, which reaches an N-factor value of 8.5 (8.7) on the top (bottom) for $\Lambda = 20°$, is determined to be a traveling crossflow mode, due to the relative wave angle, the most

amplified wavelength, and the relative phase speed. Using a critical N-factor of 5 for traveling crossflow predicts that laminar flow will not be maintained for sweep angles $\Lambda \geq 20°$.

The sweep angle $\Lambda = 15°$ is the first case for which the N-factors obtained do not exceed any critical N-factor. Although for this case, the maximum N-factor achieved on either side is only 4.0, it is important to understand the present mechanism since, as stated previously, the critical N-factor is not an exact science. Here, once again, the most unstable disturbance is considered to be traveling crossflow, and therefore is near the critical N-factor for this content. To study the development of these instabilities as the wing is pitched, this case is considered at different angles of attack in order to account for twist and variations in flight conditions. It should be noted that up to this point, any interaction between the two mechanisms has been ignored when comparing N-factor values to the critical N-factors. In reality, the Tollmien-Schlichting and stationary crossflow mechanisms interact with one another, which reduces the total amplification factor necessary for the onset of transition, as detailed in D.Arnal [11]. This interaction will be further described in the upcoming sections.

3.4 Angle of Attack Variation for $\Lambda = 15°$

The simulations performed for the $\Lambda = 15°$ sweep case are repeated for additional angles of attack to analyze the effects of pitch/twist on laminar flow for this airfoil. In addition to the $\alpha = -1.520°$ ($c_l \approx 0.65$) case discussed above, the $\alpha = -1.772°$ ($c_l \approx 0.60$) and $\alpha = -1.272°$ ($c_l \approx 0.70$) cases are also evaluated. The results of this study are presented in Figure 3.4. This figure is limited to showing primarily N-factor envelopes, rather than individual N-factor curves. In addition to the maximum N-factor envelope (red), the stationary crossflow (blue), traveling crossflow (purple), and Tollmien-Schlichting (green) envelopes are attained and shown as described in Section 3.3. In order to verify the most amplified instability mechanism, the stability characteristics of the local maximum N-factor locations are extracted and presented in table 3.4.

In table 3.4, the disturbance parameters which are characteristic of the Tollmien-Schlichting mechanism are shown in green and those characteristic of traveling crossflow are shown in purple. These will be discussed further in the coming paragraphs. In addition to the parameters above, the

Table 3.4: Parameters characterizing the most relevant disturbances for the sweep angle $\Lambda = 15°$ with varying angles of attack as seen in Figure 3.4. The purple text represents characteristics expected for the traveling cross mechanism, and green text represents characteristics expected for TS. The points where this data was extracted are indicated by grey circles in this figure. The complete lists of ψ_w and ψ_s for these cases is presented in table C.2 within Appendix C.

side,	α [°],	x/c [%]	$N_{\max}$	$4\delta_{99}$ [mm]	λ [mm]	f [Hz]	$c_{\mathrm{ph}}/\overline{u}_{s,e}$	$c_{\mathrm{ph}}/\lvert\overline{w}_{s,\max}\rvert$	$\psi_w - \psi_s$ [°]
top,	−1.772	36	3.0	11.23	27.6	2179	0.2172	15.73	+50.93
	−1.520	37	3.6	11.48	30.4	2179	0.2355	18.28	+46.11
	−1.272	38	4.2	11.64	30.5	2179	0.2341	19.83	+46.72
	−1.772	71	4.2	14.54	20.5	648	0.0433	1.90	+84.04
	−1.520	70	3.7	14.71	20.5	648	0.0432	2.04	+84.17
	−1.272	73	3.4	15.13	25.0	648	0.0518	2.46	+81.54
bottom,	−1.772	8	1.1	5.46	12.1	5843	0.3169	22.63	−30.70
	−1.772	55	3.4	13.50	16.9	648	0.0428	2.58	−84.15
	−1.520	55	4.0	13.37	16.9	648	0.0431	2.42	−84.12
	−1.272	56	4.6	13.32	16.9	648	0.0433	2.29	−84.09

effects of pressure gradient variation are studied.

First, the *top side* of the airfoil is analyzed. Referring back to Figure 1.2, as the airfoil is pitched up (α increases) the magnitude of the favorable pressure gradient for the majority of the chord decreases. As anticipated, the Tollmien-Schlichting content is thereby destabilized and reaches higher N-factors with this increase in angle of attack. The crossflow content, on the other hand, is stabilized as the airfoil is pitched up because the magnitude of the pressure gradient decreases.

The most amplified content for the top side of the airfoil varies throughout the chord. Near the stagnation line, $x/c < 5$ to 10%, the traveling crossflow content is most unstable. This is due to the large magnitude of the pressure gradient that exists in this region. As this large favorable pressure gradient subsides, the Tollmien-Schlichting content begins to destabilize. The TS envelope dictates the total maximum N-factor envelope from approximately 10 to 50% of the total chord. Near 35% chord, the pressure gradient on the top side of the airfoil becomes slightly more favorable, stabilizing the TS mechanism, which in turn reduces the corresponding N-factors beyond this location. This leads to a local maximum N-factor near 35% chord, as presented in table 3.4 and Figure 3.4. With an angle of attack increase of $0.5°$, the maximum N-factor achieved for TS

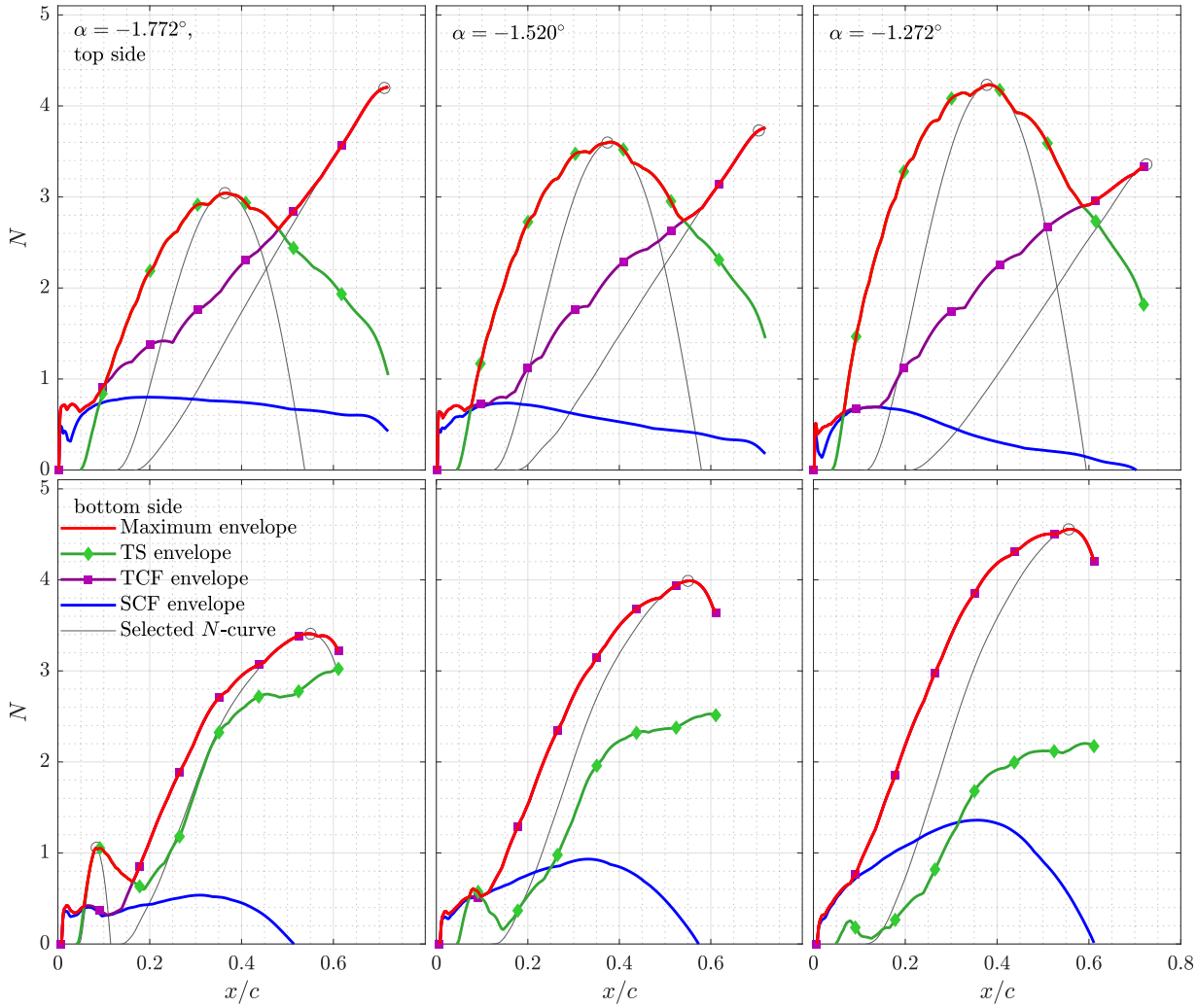

Figure 3.4: N-factor envelopes representing the overall maximum values (red), the Tollmien-Schlichting (green), stationary crossflow (blue), and traveling crossflow (purple) mechanisms for $\Lambda = 15°$. Selected N-curves, each corresponding to a single (ω, β)-combination, are shown that define the maximum envelope (grey) at the local maximums. The disturbance characteristics of these selected (ω, β)-combinations are then reported in table 3.4.

content increases by approximately 40%, from 3.0 to 4.2 units. This relative increase highlights how sensitive the Tollmien-Schlichting mechanism is to the pressure gradient. It should be noted, that as the airfoil is pitched up, the x/c location for which the TS envelope defines the maximum N-factor moves downstream. Beyond this x/c location, the maximum disturbance propagates nearly perpendicular to the streamline, has a wavelength on the order to $4\delta_{99}$, and has a phase speed on the order of the crossflow velocity component. This content is therefore determined to

be associated with traveling crossflow. As the magnitude of the pressure gradient increases in this region, as expected, the N-factors corresponding to traveling crossflow increase. When pitching the airfoil up (increasing α) the crossflow content becomes less unstable. Therefore, for the top side of the airfoil, the largest N-factor obtained for traveling crossflow, 4.2, occurs for the lowest angle of attack. With an angle of attack increase of 0.5°, the maximum N-factor obtained for traveling crossflow content decreases by 0.8 units, from 4.2 to 3.4. The top side of the S207 at $\Lambda = 15^\circ$ sweep presents an interesting case where the overall most amplified disturbance changes from crossflow for the lowest angle of attack ($\alpha = -1.772^\circ$) to Tollmien-Schlichting for the highest angle of attack ($\alpha = -1.272^\circ$).

On the *bottom* side of the airfoil, the magnitude of the favorable pressure gradient increases while the airfoil is pitched up (α increases). This stabilizes the Tollmien-Schlichting content while destabilizing the traveling crossflow modes. The maximum N-factor envelope on this side of the airfoil is almost entirely comprised of traveling crossflow content, for all angles of attack. There is only one small region of the chord ($0.05 < x/c < 0.15$) for the lowest angle of attack case ($\alpha = -1.772^\circ$) where Tollmien-Schlichting content forms the maximum overall N-factor envelope. As the airfoil is pitched up and TS is stabilized, this small region of maximum N-factor is subdued and the increasingly unstable traveling crossflow content takes over. Near the maximum x/c location contained in the stability domain, a local maximum N-factor value for the traveling crossflow content exists. An angle of attack increase of 0.5° leads to an N-factor variation of 1.2 units, from 3.4 to 4.6, at this location.

When discussing the twist/pitch of a wing, it is important that laminar flow can be maintained for all angles of attack simultaneously in order to maximize total laminar-flow coverage and minimize the total drag. To justify that these cases will or will not maintain laminar flow, the maximum N-factors achieved for each transition mechanism must be compared to its respective critical value. As stated previously, this critical N-factor value is taken to be 5 for stationary and traveling crossflow and 9 for Tollmien-Schlichting.

On the *top* side of the airfoil, the maximum N-factor value obtained for stationary or traveling

crossflow is 4.2 units. This occurs near the trailing edge for the lowest angle of attack case ($\alpha = -1.772°$). The maximum N-factor value obtained for Tollmien-Schlichting content on the top side of the airfoil is 4.2 units and occurs on the highest angle of attack case ($\alpha = -1.2726°$). Neither of these values exceed their respective critical N-factors and therefore transition is not expected on the upper surface at $15°$ of sweep. On the *bottom* side of the airfoil, the maximum N-factor value obtained for stationary or traveling crossflow is 4.6 units. This value is attained towards the rear of the stability domain for the least negative angle of attack ($\alpha = -1.272°$). The maximum N-factor value obtained for Tollmien-Schlichting content on the bottom side of the airfoil is 3.0 units and occurs on the lowest angle of attack case ($\alpha = -1.772°$). Once again, neither of these values exceed their respective critical N-factors and therefore transition is not expected on the lower surface at $15°$ of sweep.

The maximum obtained N-factors for each instability mechanism appear to change in a near-linear trend with respect to the angle of attack. If this linear trend is maintained, and the critical N-factor values are deemed to be exact (when in-fact they are only an approximation), for a sweep angle of $\Lambda = 15°$, $-2.27°$ to $-1.11°$ is the angle of attack range for which laminar flow is maintained. At both the upper and lower angle of attack bounds, traveling crossflow is the mechanism which reaches its critical value.

The analysis above, which predicts maintained laminar flow at a sweep angle of $15°$, neglects any interaction between the TS and CF mechanisms. That being said, stationary crossflow disturbances must be treated very cautiously as their stationary nature implies that any crossflow amplification at a fixed location directly feeds the (non-linear) distortion of the laminar base flow at relatively low N-factors. Therefore, in lieu of performing non-linear analysis computationally in this thesis, I will attempt to identify cases in which transition occurs due to this interaction.

In the particular case of swept wings, the effect of the SCF disturbance on the TS disturbances has been quantified through experimental correlations. This interaction is represented through the use of a "universal" $N_{\mathrm{TS,crit}}$ versus $N_{\mathrm{CF,crit}}$ curve, where $N_{\mathrm{TS,crit}}$ and $N_{\mathrm{CF,crit}}$ are the newly defined critical values for the TS and crossflow mechanisms, as fully detailed in Arnal [11]. Above

this curve, the flow is not expected to maintain laminar flow, while the opposite is true below the curve. This universal curve allows for variation in critical N-factor, depending on the strength of the interaction between the present mechanisms. A weak interaction creates a convex curve, a strong interaction leads to a concave curve, and a straight line of $N_{\mathrm{TS,crit}} + N_{\mathrm{CF,crit}} = constant$ represents a moderate interaction. The strength of the interaction between these mechanisms, and the critical curve itself, is typically determined through experiments. Without experimental data, the following equation is used to qualitatively approximate the curves presented in Arnal [11]:

$$\left(\frac{N_{\mathrm{TS,crit}}}{N_{\mathrm{TS,crit,0}}}\right)^{a} + \left(\frac{N_{\mathrm{CF,crit}}}{N_{\mathrm{CF,crit,0}}}\right)^{b} = 1$$

Here, $N_{\mathrm{TS,crit,0}}$ and $N_{\mathrm{CF,crit,0}}$ are the values previously used for the unique critical N-factors for TS (9) and CF (5), respectively. $N_{\mathrm{TS,crit}}$ and $N_{\mathrm{CF,crit}}$ are the newly defined varying critical values which are used to generate the "universal" curves. The a and b values dictate the strength of the interaction which these curves correspond to. Values greater than 1 represent a weak interaction, values equal to 1 represent a moderate interaction, and values less than 1 represent strong interactions. For the present study, a and b are both set to 0.5 for strong interactions. The resulting convex curve is shown in Figure 3.5 with a dashed line, along with the curve representative of a moderate interaction.

The traveling crossflow N-factor envelopes are also plotted against the TS N-factor envelope in Figure 3.5 for completeness. It should be emphasized that the previously discussed interaction criterion does not apply to this combination of instability mechanisms, and further experimental research is required to quantify any interaction which may occur.

For corresponding x/c locations, the maximum Tollmien-Schlichting and crossflow N-factors have been plotted against one another and shown in Figure 3.5 as N_{TS} versus N_{CF} curves. To track the x/c progression, markers are placed at every 20% of the chord and the filled marker corresponds to $x/c \approx 0.20$. Additionally, arrows are shown which indicate the direction of increasing x/c. The bounds for the N_{TS} and N_{SCF} axes are set to the respective values for the previously considered

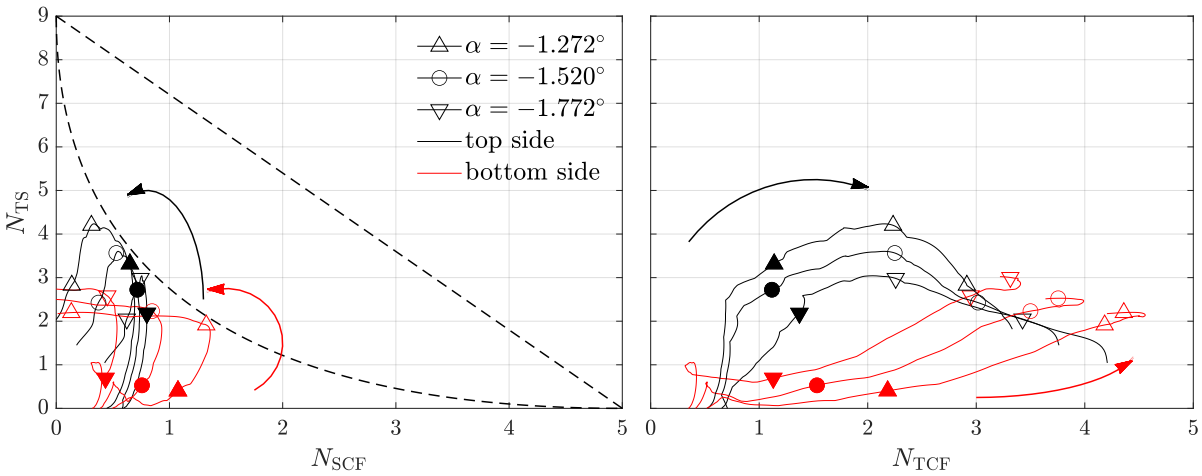

Figure 3.5: Tollmien-Schlichting and stationary crossflow N-factors attained for the $15°$ sweep case plotted against qualitative representations of the critical "universal" curves representing strong (concave line) and moderate (straight line) interactions. N-factors corresponding to traveling crossflow are also plotted against TS N-factors for completeness. The markers are placed at every 20% of the chord in order to follow the N-factor evolution in x. The first marker, at $x/c \approx 0.20$, is filled in. Additionally, arrows are shown which indicated increasing x/c are drawn. Black lines correspond to the top side of the airfoil, while red lines indicate the bottom side.

unique critical N-factors.

For the $\Lambda = 15°$ sweep case, when discussing the interaction between the stationary crossflow and Tollmien-Schlichting mechanisms, the N-factors obtained are in the vicinity of the strong-interaction curve. Previous studies by Henke et al. [39], Redeker et al. [40], and Horstmann et al. [41], have indicated a weak interaction between TS and SCF. On the other hand, work presented in Rozendaal (1987) [38], Runyan et al. [42], and Obara et al. [43] shows a strong-interaction between the stationary crossflow and Tollmien-Schlichting mechanisms in the flow over a transonic swept wing. To err on the side of caution, since the N_{TS} versus N_{SCF} curves are near the qualitative curve representative of a strong interaction and the N-factors obtained by traveling crossflow are close to the considered unique critical value, a slightly reduced sweep angle is also studied.

3.5 Angle of Attack Variation for $\Lambda = 12.5°$

To account for the uncertainty of the critical N-factor method, although the $15°$ sweep case does not reach any critical N-factor values, an angle of attack variation study is also performed

Table 3.5: Parameters characterizing the most relevant disturbances for the sweep angle $\Lambda = 12.5°$ with varying angles of attack as seen in Figure 3.6. The purple text represents characteristics expected for the traveling cross mechanism, and green text represents characteristics expected for TS. The points where this data was extracted are indicated by grey circles in this figure. The complete lists of ψ_w and ψ_s for these cases is presented in table C.3 within Appendix C.

side,	α [°],	x/c [%]	$N_{\max}$	$4\delta_{99}$ [mm]	λ [mm]	f [Hz]	$c_{\mathrm{ph}}/\overline{u}_{s,e}$	$c_{\mathrm{ph}}/\lvert\overline{w}_{s,\max}\rvert$	$\psi_w - \psi_s$ [°]
top,	−1.772	37	2.7	11.29	29.7	2179	0.2347	20.21	+46.08
	−1.520	38	3.3	11.53	29.9	2179	0.2332	21.53	+46.72
	−1.272	38	3.9	11.64	30.1	2179	0.2319	23.51	+47.27
	−1.772	70	2.1	14.54	20.5	648	0.0438	2.40	+84.22
	−1.520	70	1.9	14.71	25.0	648	0.0530	3.04	+82.77
	−1.272	70	1.7	14.84	25.0	648	0.0525	3.11	+82.79
bottom,	−1.772	9	0.9	5.58	12.5	5843	0.3298	27.54	−25.41
	−1.520	8	0.5	5.28	12.2	5843	0.3325	24.68	−24.31
	−1.772	60	2.4	14.05	36.2	1458	0.2059	14.70	−49.89
	−1.520	52	2.0	12.96	17.0	648	0.0438	2.94	−84.06
	−1.272	52	2.3	12.94	17.0	648	0.0440	2.77	−84.05

on the $12.5°$ sweep angle case. The results of this study are presented in Figure 3.6 and table 3.5. In both the table and figure, the disturbances which are representative of the Tollmien-Schlichting mechanism are shown in green and those characteristic of traveling crossflow are shown in purple. Figure 3.6 also displays envelopes for the stationary crossflow disturbance and the overall maximum N-factor achieved. The effects on the pressure distribution of pitching this airfoil are independent of sweep angle and therefore trends remain the same between sweep cases. On the top (bottom) side, pitching the airfoil up (increasing α) leads to a less (more) favorable pressure gradient.

First, the *top* side of the airfoil is analyzed. The most amplified content on this side of the airfoil varies along the chord for this sweep case, similar to that seen in the $\Lambda = 15°$ case. There remains a small region near the attachment line where the magnitude of the pressure gradient is extremely large and therefore the crossflow mechanism is highly destabilized. Following this region of large pressure gradient, the Tollmien-Schlichting content begins to destabilize and the corresponding TS envelope defines the maximum overall envelope for the majority of the chord.

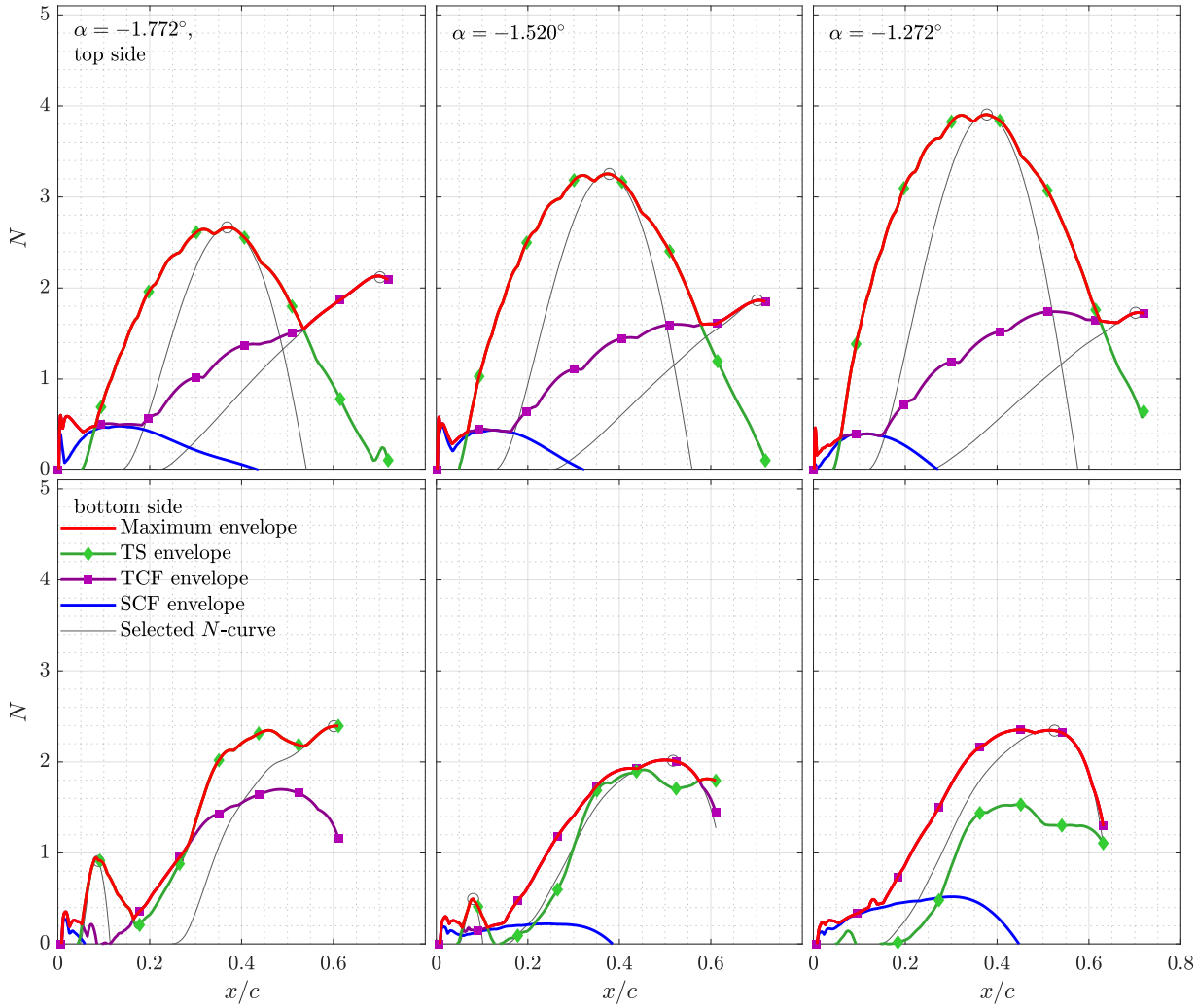

Figure 3.6: N-factor envelopes representing the overall maximum values (red), the Tollmien-Schlichting (green), stationary crossflow (blue), and traveling crossflow (purple) mechanisms for $\Lambda = 12.5°$. Selected N-curves, each corresponding to a single (ω, β)-combination, are shown that define the maximum envelope (grey) at the local maximums. The disturbance characteristics of these selected (ω, β)-combinations are then reported in table 3.5.

With the reduction of sweep angle, the crossflow component of velocity is smaller and therefore the crossflow mechanism is less unstable. This causes the TS mechanism to cover a larger x/c range of the maximum N-factor envelope, relative to the $\Lambda = 15°$ case. Pitching the airfoil up, further stabilizes this crossflow content resulting in an even greater x/c range for which the maximum N-factor envelope is defined by Tollmien-Schlichting growth. The sweep angle reduction has a minor effect on the maximum N-factors achieved by Tollmien-Schlichting, which range from 2.7

to 3.9 for the $\Lambda = 12.5^\circ$ sweep case as compared to $3.0 - 4.2$ for the $\Lambda = 15^\circ$ case. Crossflow content, on the other hand, varies rather drastically with this change in sweep angle. While the $\Lambda = 15^\circ$ sweep case reached crossflow N-factors of 3.4 to 4.6, the maximum crossflow N-factors achieved for the $\Lambda = 12.5^\circ$ case range from 1.7 to 2.1. This is approximately a 50% decrease in maximum N-factor achieved for the crossflow mechanism on the top side of the airfoil.

The *bottom* side of the airfoil at $\Lambda = 12.5^\circ$ sweep presents an rather interesting case. For the *lowest* angle of attack ($\alpha = -1.772^\circ$), the Tollmien-Schlichting content dominates the overall maximum N-factor envelope for the majority of the chord. For the *highest* angle of attack ($\alpha = -1.272^\circ$), on the other hand, the traveling crossflow content dominates the maximum N-factor envelope. At the intermediate/design angle of attack ($\alpha = -1.520^\circ$) the amplitudes of the N-factor envelopes for both Tollmien-Schlichting and traveling crossflow content are fairly similar. This crossover emphasizes the effect of the pressure distribution, due to a varied angle of attack, on the growth of each mechanism. Similar to the top side of the airfoil, the reduction in sweep angle has a large effect on the maximum N-factor reached by traveling crossflow content. The 12.5° sweep case sees maximum N-factor values of 1.6-2.4 units as compared to 3.4-4.6 units for the 15° sweep case. This again is approximately a 50% decrease in the maximum N-factor achieved for the crossflow mechanism.

The maximum N-factor achieved for traveling crossflow content on the *top* of the airfoil, considering all studied angles of attack, is 2.1. This occurs for the lowest angle of attack, where the pressure gradient is most favorable. The largest N-factor achieved for Tollmien-Schlichting on this side of the airfoil is 3.9 and occurs on the highest angle of attack, where the pressure gradient is least favorable. The maximum N-factor for all traveling crossflow content on the *bottom* side of the airfoil is 2.4 and occurs at the highest angle of attack. This is due to the magnitude of the pressure gradient being largest for this case. The maximum N-factor attained on the bottom side by Tollmien-Schlichting is 2.4 and occurs at the lowest angle of attack, where the pressure gradients are least favorable. Comparing these maximum N-factor values to the critical N-factors for traveling crossflow (5) and Tollmien-Schlichting (9) predicts that laminar flow will be maintained

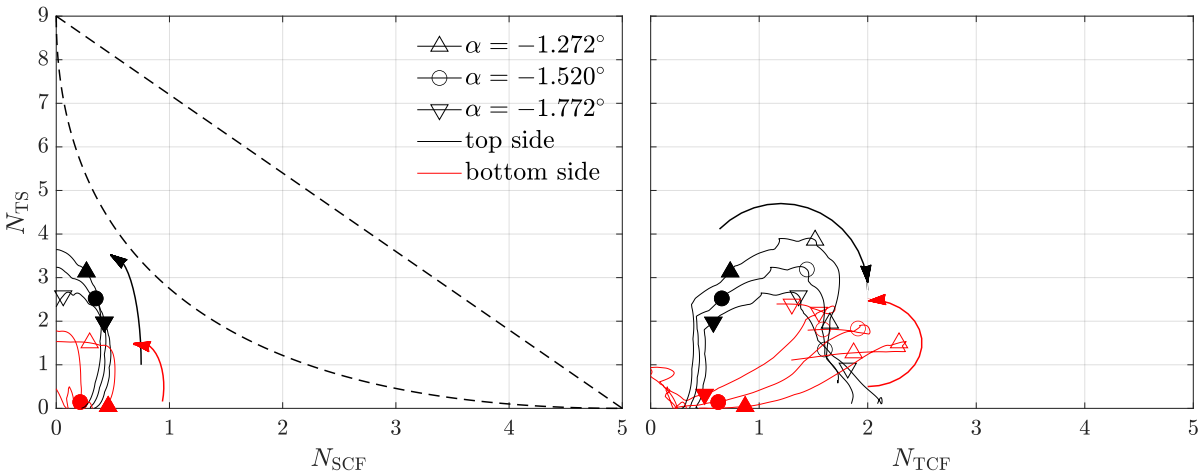

Figure 3.7: Tollmien-Schlichting and crossflow N-factors attained for the $12.5°$ sweep case plotted against critical "universal" curves representing strong (concave line) and moderate (straight line) interactions. N-factors corresponding to traveling crossflow are also plotted against TS N-factors for completeness. The markers are placed at every 20% of the chord in order to follow the N-factor evolution in x. The first marker, at $x/c \approx 0.20$, is filled in. Additionally, arrows are shown which indicated increasing x/c are drawn. Black lines correspond to the top side of the airfoil, while red lines indicate the bottom side.

on the both sides of the airfoil for $12.5°$ sweep.

The maximum N-factor value corresponding to each mechanism appears to change linearly with respect to the angle of attack, as previously seen for the $15°$ sweep case. If this linear trend continues, $\alpha = -5.40°$ to $0.59°$ is the angle of attack range for which laminar flow is maintained. Once again, this range is defined by the traveling flow content reaching its critical N-factor. It should be noted that this range is not anticipated to be realistic for the flow, but it does highlight the increased allowable margin of error for the angle of attack range discussed throughout this paper.

The prior analysis for the $12.5°$ sweep case neglects any interaction between the TS and CF mechanisms. In order to account for this interaction, as detailed in Section 3.4 for the $15°$ sweep case, the N-factors attained for TS and SCF content are plotted against one another and compared to the universal critical curves representing a moderate and strong interaction. Once again, for completeness, the N-factors obtained by traveling crossflow are plotted against those obtained

by TS. As before, the interaction criterion for stationary crossflow and TS does not apply to the combination of the traveling crossflow and TS mechanisms. The results of this study are presented in Figure 3.7. This figure predicts that for a strong interaction between TS and SCF, the N_{TS} versus N_{SCF} curves are adequately beneath the representative critical curve. Therefore, a strong interaction between the TS and SCF mechanisms does not appear to lead to early, SCF-induced transition.

For this reason, the crossflow instability is not expected to negate the benefits of the slotted, natural-laminar-flow design for the studied angle of attack range at a $\Lambda = 12.5^{\circ}$ sweep angle. Due to the 12.5° sweep case's predicted ability to maintain laminar flow for all studied angles of attack, this sweep angle has been selected for further wind tunnel analysis [44].

4. CONCLUSION

The primary goal of this paper is to identify the critical sweep angle beyond which the crossflow instability negates the benefits of the natural-laminar-flow design of the S207 airfoil, for a range of angles of attack. This is done by studying the growth/decay of disturbances in the flow using the Linear Parabolized Stability Equations (LPSE) in tandem with Linear Stability Theory (LST). To properly study the disturbances in this flow, a high-quality representation of the laminar base-flow without these disturbances must obtained.

Base-flow data is obtained using multiple methods. Full, steady Navier-Stokes and boundary-layer solutions have been obtained using OVERFLOW and DEKAF, respectively. DEKAF solutions were obtained using two different approaches for sweeping the wing. One method, DEKAF$^{\mathrm{s}}$, solves the boundary-layer equations on an OVERFLOW-obtained swept C_p. DEKAF$^{\mathrm{u}}$, on the other hand, sweeps the C_p internally to DEKAF. All three of these methods are then cross-verified with respect to each other. This demonstrates that the resolution of OVERFLOW is sufficient to reproduce the extremely high resolution boundary-layer results. This also shows that the boundary-layer assumptions implemented do not have a large effect on the stability results. Showing that results obtained using DEKAF$^{\mathrm{u}}$ and DEKAF$^{\mathrm{s}}$ base flows are comparable removes the necessity of running OVERFLOW on a large number of different sweep angles. Using LPSE stability analysis, baseline resolutions are determined for which stability solutions are deemed sufficiently converged. Stability results obtained on the different base-flow data sets at this baseline resolution are then compared to quantify the effects of using different base flow solutions on the stability results.

Within this paper, the effects of angle of attack variation, in addition to the sweep angle, are considered. This is to study the feasibility of maintaining laminar flow on a twisted wing or at off-design flight conditions. For a twisted wing configuration, in order for the SNLF design to achieve maximum drag reduction, laminar flow must be maintained at all spanwise locations. The SNLF design works to create a large region of favorable pressure gradient, on both the top and bottom surfaces of the airfoil, which is known to stabilize the Tollmien-Schlichting mechanism.

An increase in angle of attack decreases the magnitude of the favorable pressure gradient on the top surface and increases it on the bottom. This destabilizes TS content on the top side, while stabilizing it on the bottom. The crossflow mechanism, on the other hand, is destabilized by the presence of pressure gradients. As the magnitude of the pressure gradient decreases (increases) with an increased angle of attack on the top (bottom) side of the airfoil, the crossflow mechanism becomes less (more) destabilized. These trends were expected due to previous studies performed for transonic airfoils and are verified in the analysis present throughout this paper.

For all sweep angles and angles of attack, the most unstable disturbances are argued to be Tollmien-Schlichting (TS), stationary crossflow (SCF), and traveling crossflow (TCF). The classification of each disturbance as one of these three mechanisms is determined by the disturbance frequency, wavelength, phase speed, wave angle, and how it is influenced by the pressure gradient. In absence of relevant data pertaining to the freestream disturbance environment in flight, a critical N-factor value of 9 is assumed for the TS disturbances and a conservative value of 5 is used for SCF and TCF crossflow disturbances. Comparing the maximum N-factor obtained for each disturbance type to its respective critical value, for each sweep angle and angle of attack, helps to define the range of angles for which laminar flow is maintained.

At the design angle of attack, for sweep angles $\Lambda \geq 25^\circ$, N-factors corresponding to stationary crossflow disturbances exceed 5 units, on both the top and bottom sides of the airfoil. For the 20° sweep case, the stationary crossflow touches, but does not exceed this 5 unit critical value. The TCF disturbances, however, attain N-factor values of 8.5 and 8.7 on the top and bottom sides of the airfoil, respectively, which exceed the critical value for traveling crossflow. For this reason, the $\Lambda = 15^\circ$ sweep case is first case selected for further angle of attack variation analysis.

For the $\Lambda = 15^\circ$ case, across all considered angles of attack and on both sides of the airfoil, the maximum N-factor obtained for all disturbances is 4.6. This value is attributed to the traveling crossflow disturbances. The highest N-factor achieved for TS content is 4.2. Although neither of these values exceed their respective critical value, since the maximum TCF N-factor is near its critical value, it is important to study lower sweep angles to allow for some margin of error. For

the $\Lambda = 12.5^\circ$ case, the maximum N-factor value across all angles of attack and sides was found to be 3.9 and corresponds to the TS mechanism. The maximum N-factor obtained for the TCF content is only 2.4, well below its critical value.

For all considered angles of attack and the sweeps $\Lambda \leq 12.5^\circ$, the maximum N-factors obtained by Tollmien-Schlichting and crossflow instabilities are well below their respective critical values. Additionally, taking into account the interaction between the stationary crossflow and Tollmien-Schlichting mechanisms as described by Arnal [11], laminar flow is expected to be maintained considering a strong interaction between SCF and TS. For this reason, for sweep angles up to and including 12.5°, the crossflow instability does not appear to negate the benefits of the slotted, natural-laminar-flow design for the S207 at flight conditions. This sweep angle has been selected for further wind-tunnel analysis.

REFERENCES

[1] M. Tsairides and K. Datta, "ARMD- University Leadership Initiative (ULI)," 2019. data retrieved on 2 March 2020 from, `https://nari.arc.nasa.gov/uli`.

[2] I. A. T. Association, "IATA Resolution on the Implementation of the Aviation 'CNG2020 Strategy'," June 2013.

[3] R. D. Joslin, "Aircraft Laminar Flow Control," *Annual Review of Fluid Mechanics*, vol. 30, no. 1, pp. 1–29, 1998.

[4] T. Washburn, "Airframe Drag/Weight Reduction Technologies," *Green Aviation Summit-Fuel Burn Reduction, NASA Ames Research Centre*, 2010.

[5] D. M. Somers, "An Exploratory Investigation of a Slotted, Natural-Laminar-Flow Airfoil," Tech. Rep. NASA/CR–2012-217560, National Aeronautics and Space Administration, 2012.

[6] H. L. Reed and W. S. Saric, "Stability of Three-Dimensional Boundary Layers," *Annual Review of Fluid Mechanics*, vol. 21, no. 1, pp. 235–284, 1989.

[7] L. M. Mack, "Boundary-Layer Linear Stability Theory," in *Special Course on Stability and Transition of Laminar Flow, AGARD 709*, AGARD, 1984.

[8] D. M. Bushnell, "Aircraft Drag Reduction—A Review," *Proceedings of the Institution of Mechanical Engineers, Part G: Journal of Aerospace Engineering*, vol. 217, no. 1, pp. 1–18, 2003.

[9] H. L. Reed, W. S. Saric, and D. Arnal, "Linear Stability Theory Applied to Boundary Layers," *Annual Review of Fluid Mechanics*, vol. 28, no. 1, pp. 389–428, 1996.

[10] W. S. Saric, H. L. Reed, and E. B. White, "Stability and Transition of Three-Dimensional Boundary Layers," *Annual Review of Fluid Mechanics*, vol. 35, no. 1, pp. 413–440, 2003.

[11] D. Arnal, "Boundary Layer Transition: Predictions Based on Linear Theory," in *Special Course on Progress in Transition Modeling, AGARD 793*, AGARD, 1994.

[12] G. Lachmann, "Boundary Layer Control," *The Aeronautical Journal*, vol. 59, no. 531, pp. 163–198, 1955.

[13] P. Garabedian and G. McFadden, "Design of Supercritical Swept Wings," *AIAA journal*, vol. 20, no. 3, pp. 289–291, 1982.

[14] D. M. Somers, "Design of a Slotted, Natural-Laminar-Flow Airfoil for a Transport Aircraft," no. NASA/CR–2019-220403, 2019.

[15] J. Anderson, *Fundamentals of Aerodynamics*. McGraw-Hill, 2006.

[16] M. Cavcar, "Bréguet Range Equation?," *Journal of Aircraft*, vol. 43, no. 5, pp. 1542–1544, 2006.

[17] K. J. Groot, E. S. Beyak, D. Heston, and H. L. Reed, "Boundary-Layer Stability of a Natural-Laminar-Flow Airfoil," *AIAA Paper, 2020-1024*, 2020.

[18] F. White, *Viscous Fluid Flow*. McGraw Hill Series in Mechanical Engineering, McGraw-Hill, 1991.

[19] K. J. Groot, E. S. Beyak, D. T. Heston, and H. L. Reed, "Boundary-Layer Stability of a Natural-Laminar-Flow Airfoil at Flight Conditions," *AIAA Paper, 2020-3052*, 2020.

[20] H. Nichols and P. Buning, "User's Manual for OVERFLOW 2.2, August 2010," *http:people.nas.nasa.gov/pulliam/Overflow/OverflowManuals.html*.

[21] J. G. Coder, "Further Development of the Amplification Factor Transport Transition Model for Aerodynamic Flows," *AIAA Paper, 2019-0039*, 2019.

[22] T. S. Kocian, *Computational Hypersonic Boundary-Layer Stability and the Validation and Verification of EPIC*. Ph.D. Dissertation, Texas A&M University, 2018.

[23] K. J. Groot, F. Miró Miró, E. S. Beyak, A. Moyes, F. Pinna, and H. L. Reed, "DEKAF: Spectral Multi-Regime Basic-State Solver for Boundary Layer Stability," *AIAA Paper, 2018-3380*, 2018.

[24] W. E. Arnoldi, "The Principle of Minimized Iterations in the Solution of the Matrix Eigenvalue Problem," *Quarterly of Applied Mathematics*, vol. 9, no. 1, pp. 17–29, 1951.

[25] N. B. Oliviero, "EPIC: A New and Advanced Nonlinear Parabolized Stability Equation Solver," Master's thesis, Texas A&M University, 2015.

[26] A. Moyes, *Computational Laminar-to-Turbulent Transition Physics of Complex Three-Dimensional Hypersonic Flow Fields*. Ph.D. Dissertation, Texas A&M University, 2019.

[27] N. B. Oliviero, T. S. Kocian, A. J. Moyes, and H. L. Reed, "EPIC: NPSE Analysis of Hypersonic Crossflow Instability on Yawed Straight Circular Cone," *AIAA paper, 2015-2772*, 2015.

[28] A. Moyes, E. S. Beyak, T. S. Kocian, and H. L. Reed, "Accurate and Efficient Modeling of Boundary-Layer Instabilities," *AIAA Paper, 2019-1907*, 2019.

[29] B.-T. Chu, "On the Energy Transfer to Small Disturbances in Fluid Flow (Part I)," *Acta Mechanica*, vol. 1, no. 3, pp. 215–234, 1965.

[30] J. Van Ingen, "A Suggested Semi-Empirical Method for the Calculation of the Boundary Layer Transition Region," *Technische Hogeschool Delft, Vliegtuigbouwkunde, Rapport VTH-74*, 1956.

[31] J. Van Ingen, "The e^N Method for Transition Prediction. Historical Review of Work at TU Delft," *AIAA Paper, 2008-3830*, 2008.

[32] T. S. Haynes and H. L. Reed, "Simulation of Swept-Wing Vortices Using Nonlinear Parabolized Stability Equations," *Journal of Fluid Mechanics*, vol. 405, pp. 325–349, 2000.

[33] M. W. Tufts, H. L. Reed, and W. S. Saric, "Design of an Infinite-Swept-Wing Glove for In-Flight Discrete-Roughness-Element Experiment," *Journal of Aircraft*, vol. 51, no. 5, pp. 1618–1631, 2014.

[34] R. Michel, D. Arnal, and E. Coustols, "Stability Calculations and Transition Criteria on Two- or Three-Timensional Flows," in *Laminar-Turbulent Transition*, pp. 455–461, Springer, 1985.

[35] K. Groot, *BiGlobal Stability of Shear Flows: Spanwise & Streamwise Analyses*. Ph.d. dissertation, Delft University of Technology, 2018.

[36] R. A. Rozendaal, "Natural Laminar Flow Flight Experiments on a Swept Wing Business Jet-Boundary Layer Stability Analyses," in *NASA Langley, CR 3975*, 1986.

[37] R. A. Rozendaal, "Variable Sweep Transition Flight Experiment (VSTFE)-Parametric Pressure Distribution Boundary Layer Stability Study and Wing Glove Design Task," in *NASA Langley, CR 3992*, 1986.

[38] R. A. Rozendaal, "Variable-Sweep Transition Flight Experiment (VSTFE): Stability Code Development and Clean-up Glove Data Analysis," in *Natural Laminar Flow and Laminar Flow Control Research, Part 3, NASA Langley, CP 2487*, 1987.

[39] R. Henke, F. Muench, and A. Quast, "Natural Laminar Flow-A Wind Tunnel Test Campaign and Comparison with Flight Test Data," in *Flight Simulation Technologies Conference and Exhibit*, p. 3045, 1990.

[40] G. Redeker, K. Horstmann, H. Koester, P. Thiede, and J. Szodruch, "Design for a Natural Laminar Flow Glove for a Transport Aircraft," in *Flight Simulation Technologies Conference and Exhibit*, p. 3043, 1990.

[41] K. Horstmann, G. Redeker, A. Quast, U. Dressler, and H. Bieler, "Flight Tests with a Natural Laminar Flow Glove on a Transport Aircraft," in *Flight Simulation Technologies Conference and Exhibit*, p. 3044, 1990.

[42] L. J. Runyan, B. H. Navran, and R. A. Rozendaal, "F-111 Natural Laminar Flow Glove Flight Test Data Analysis and Boundary Layer Stability Analysis," in *NASA Langley, CR 166051*, 1984.

[43] C. Obara, C. Lee, and P. Vijgen, "Analysis of Flight-Measured Boundary-Layer Stability and Transition Data," *AIAA Paper, 1991-3282*, 1991.

[44] J. G. Coder and D. M. Somers, "Design of a Slotted, Natural-Laminar-Flow Airfoil for Commercial Transport Applications," *Aerospace Science and Technology*, no. 106217, 2020.

APPENDIX A

COORDINATE SYSTEM DEFINITION

In the following section, the coordinate systems used throughout this study are described. In both the LST and LPSE equations, the stability problem is solved along a curvilinear coordinate system: s, y, and z. The s-direction traces along the airfoil in a leading-edge-orthogonal manner. The y-direction is the surface-orthogonal direction and also varies along the chord. The z-direction, on the other hand, is always leading edge parallel. This coordinate system is visualized in Figure A.1

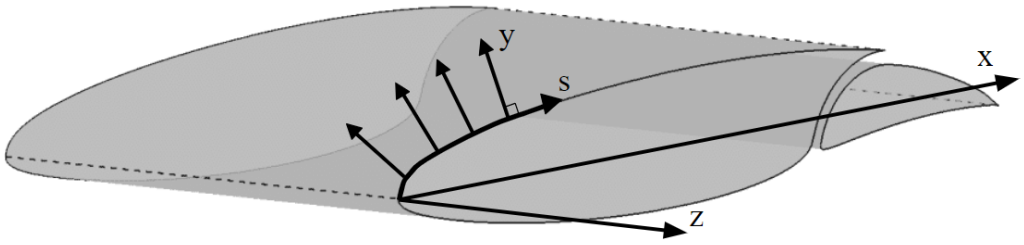

Figure A.1: $s, y, \text{and } z$ coordinates system. x is also displayed here.

In Figure A.2, the inviscid streamline is shown with a blue line and important angles used throughout this paper are visualized. The angles $\Lambda, \psi_w, \text{and } \psi_s$ are the sweep angle, wave angle, and streamline angle, respectively, and are defined as follows:

$$\Lambda \equiv \Lambda^{\overline{w}_\infty}_{\sqrt{\overline{u}_\infty^2+\overline{v}_\infty^2}} = \arctan\frac{\overline{w}_\infty}{\sqrt{\overline{u}_\infty^2+\overline{v}_\infty^2}}, \qquad \psi_w = \arctan\left(\frac{\beta_r}{\alpha_r}\right), \qquad \psi_s = \arctan\left(\frac{\overline{w}_e}{\overline{u}_e}\right) \tag{A.1}$$

Here, $\overline{u}_\infty, \overline{v}_\infty, \text{and } \overline{w}_\infty$ are the freestream velocity components in the $x, Y_c, \text{and } z$ directions, respectively. β_r is the real part of the spanwise wavenumber and α_r is the real part of the streamwise

wave number. Additionally, $\overline{w}_0$ is the crossflow component of velocity at the edge of the boundary layer and for infinite swept wings is equal to $\overline{w}_\infty$. $\overline{u}_e$ is the velocity component in the leading-edge-orthogonal direction at the end of the wall-normal domain of DEKAF.

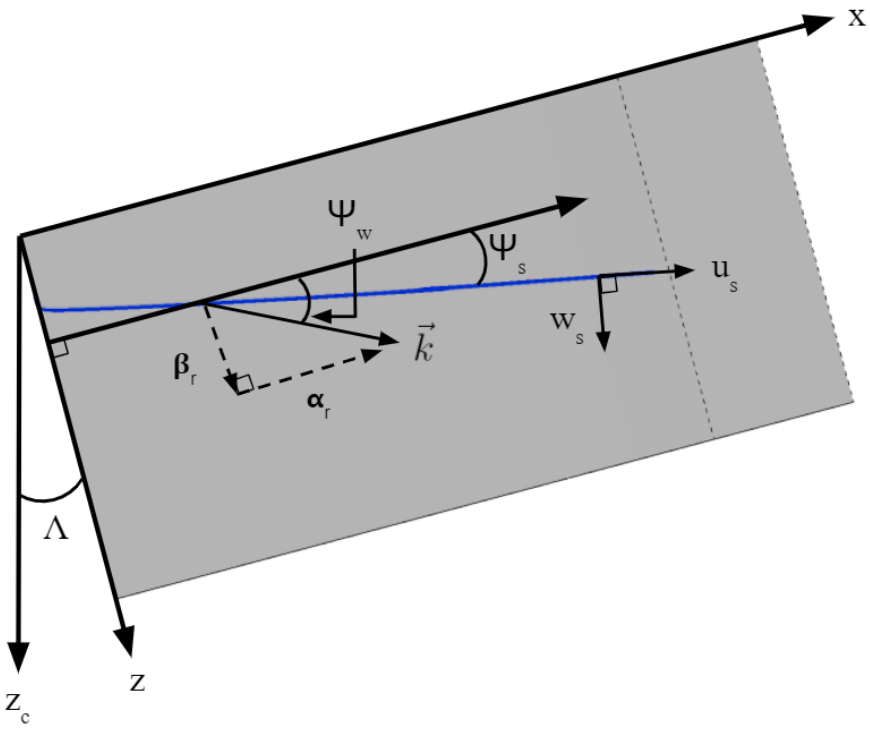

Figure A.2: Important angles used throughout this study are displayed. The blue line is the inviscid streamline for the $\Lambda = 15°$ sweep case. All variables shown are defined within Section A

The subscript c comes from the conventional swept-wing coordinate system, in which the leading edge is swept back with respect to the Z_c axis. u_s and w_s are the streamwise and streamwise-perpendicular velocity components that exist within the boundary layer.

The x-axis, shown in Figures A.1 and A.2, is better defined in Figure A.3. In this figure, the x-axis is visualized by a blue-dashed line. The chord line is defined by a line created between the trailing edge and the airfoil-surface coordinate furthest away from the trailing edge. This line is shown by a solid red line, and is typically gathered with the x-axis. For the S207, the x-axis is not

gathered with this chord axis. To make the x-axis parallel to the chord axis, a rotation of 1.1342° in the clockwise direction about the z axis is required.

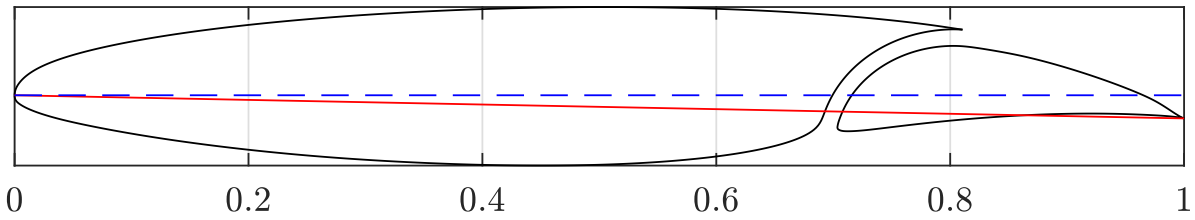

Figure A.3: Difference between the x and chord axis.

APPENDIX B

GOVERNING EQUATIONS

B.1 Nondimensionalization

All the variables used within EPIC and present in the equations laid out in Sections B.2 and B.3 are nondimensional. These nondimensionalizations occurs as follows:

$$u = \frac{u^*}{U_e^*}, \qquad v = \frac{v^*}{U_e^*}, \qquad w = \frac{w^*}{U_e^*}, \qquad x = \frac{x^*}{L^*}, \qquad y = \frac{y^*}{L^*}, \qquad z = \frac{z^*}{L^*},$$

$$T = \frac{T^*}{T_e^*}, \qquad \rho = \frac{\rho^*}{\rho_e^*}, \qquad \mu = \frac{\mu^*}{\mu_e^*}, \qquad \kappa = \frac{\kappa^*}{\kappa_e^*}, \qquad c_p = \frac{c_p^*}{{c_{p_e}}^*} = 1, \qquad c_v = \frac{c_v^*}{{c_{v_e}}^*} = 1,$$

$$t = \frac{t^* L^*}{U_e^*}, \qquad P = \frac{P^*}{\rho_e^* U_e^{*2}}, \qquad R_g = \frac{R_g^*}{{R_{ge}}^*} = 1, \qquad \lambda_v = \frac{\lambda^*}{\mu_e^*}, \qquad L^* \equiv \sqrt{\frac{\mu_e^* c}{\rho_e^* U_e^*}}$$

The superscipt $*$ corresponds to non-dimensional quantities. The velocity components are nondimensionalized by U_e^*, which is the edge value of the u^*-component of velocity. The temperature, density, dynamic viscosity, thermal conductivity, specific heat terms, and the specific gas constant are normalized by their edge values. The edge refers to a location where perturbations have died out, and is typically defined as the edge of the boundary layer. For the purpose of this study, theses edge values are defined as the values at the last wall-normal point in the DEKAF domain. We can also define the following non-dimensional quantities:

$$\mathrm{Re} \equiv \frac{\rho_e^* U_e^* L^*}{\mu_e^*}, \qquad \mathrm{Pr} \equiv \frac{{c_{p_e}}^* \mu_e^*}{\kappa_e^*}, \qquad \gamma_e \equiv \frac{{c_{p_e}}^*}{{c_{v_e}}^*}, \qquad \mathrm{M}^2 \equiv \frac{U_e^{*2}}{\gamma R_g^* T_e^*}, \qquad \mathrm{Ec}_e \equiv \frac{U_e^{*2}}{h_e^*}$$

Note that the values of $c_p^*/{c_{p_e}}^*$ and $c_v^*/{c_{v_e}}^*$ being set equal to unity only applies for calorically perfect gases. The value $R_g^*/{R_{g_e}}^*$ also is set equal to unity for thermally perfect gases (and therefore calorically perfect gases). For the sake of this study, the calorically gas assumptions are made.

B.2 LST Governing Equations

After applying all of the LST assumptions, the stability problem takes on a system of individual disturbance equations which are represented as:

$$\mathcal{A}\frac{\mathrm{d}^2\hat{\phi}}{\mathrm{d}y^2} + \mathcal{B}\frac{\mathrm{d}\hat{\phi}}{\mathrm{d}y} + \mathcal{C}\hat{\phi} = 0 \tag{B.1}$$

Here, $\hat{\phi}$ is the vector of flow variables $\left[\hat{u}, \hat{v}, \hat{w}, \hat{T}, \hat{\rho}\,\right]$, and $\mathcal{A}$, $\mathcal{B}$, and $\mathcal{C}$ are (5×5) matrices that exist at for each wall-normal location. Expanding all of the terms in Equation B.1 leads to the equations for $s-, y-, \text{and } z-$ momentum, conservation of energy, and continuity as seen below. Throughout these equations, subscripts $s, y, \text{and } \overline{T}$ are independent variables of differentiation. Every other subscript is there for notation purposes only and does not imply any sort of differentiation. Due to the curvilinear coordinate system, scaling terms ($h_1 \text{ and } h_3$) are included and defined as such:

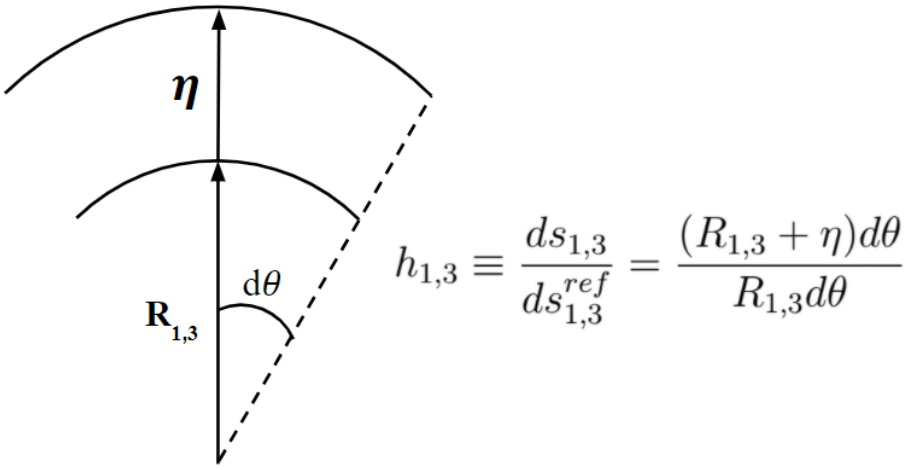

Figure B.1: Scaling factor derivation in the streamwise (1) and spanwise (3) directions. $ds_{1,3}$ is the differential surface distance in the (1,3)-direction and $ds_{1,3}^{ref}$ is the corresponding differential surface distance at the wall.

B.2.1 Momentum along the s-Axis

$$\frac{\alpha\,\beta\,\overline{\mu}\,\hat{w}}{\mathrm{Re}_e\,h_1\,h_3}+\frac{\alpha\,\beta\,\overline{\lambda}\,\hat{w}}{\mathrm{Re}_e\,h_1\,h_3}+\frac{i\,\beta\,\overline{\rho}\,\hat{u}\,\overline{w}}{h_3}-\frac{i\,\alpha\,\overline{\mu}\,\hat{v}_y}{\mathrm{Re}_e\,h_1}-\frac{i\,\alpha\,\overline{\lambda}\,\hat{v}_y}{\mathrm{Re}_e\,h_1}+\overline{\rho}\,\overline{u}_y\,\hat{v}+\frac{h_{1,y}\,\overline{\rho}\,\overline{u}\,\hat{v}}{h_1}-\frac{i\,\overline{T}_y\,\alpha\,\overline{\mu}_{\overline{T}}\,\hat{v}}{\mathrm{Re}_e\,h_1}-$$
$$\frac{i\,\alpha\,h_{3,y}\,\overline{\mu}\,\hat{v}}{\mathrm{Re}_e\,h_1\,h_3}-\frac{3\,i\,\alpha\,h_{1,y}\,\overline{\mu}\,\hat{v}}{\mathrm{Re}_e\,h_1^2}-\frac{i\,\alpha\,h_{3,y}\,\overline{\lambda}\,\hat{v}}{\mathrm{Re}_e\,h_1\,h_3}-\frac{i\,\alpha\,h_{1,y}\,\overline{\lambda}\,\hat{v}}{\mathrm{Re}_e\,h_1^2}-\frac{\overline{\mu}\,\hat{u}_{y\,y}}{\mathrm{Re}_e}-\frac{\overline{T}_y\,\overline{\mu}_{\overline{T}}\,\hat{u}_y}{\mathrm{Re}_e}-\frac{h_{3,y}\,\overline{\mu}\,\hat{u}_y}{\mathrm{Re}_e\,h_3}-$$
$$\frac{h_{1,y}\,\overline{\mu}\,\hat{u}_y}{\mathrm{Re}_e\,h_1}+\frac{i\,\alpha\,\overline{\rho}\,\overline{u}\,\hat{u}}{h_1}-i\,\omega\,\overline{\rho}\,\hat{u}+\frac{\overline{T}_y\,h_{1,y}\,\overline{\mu}_{\overline{T}}\,\hat{u}}{\mathrm{Re}_e\,h_1}+\frac{h_{1,y}\,h_{3,y}\,\overline{\mu}\,\hat{u}}{\mathrm{Re}_e\,h_1\,h_3}+\frac{\beta^2\,\overline{\mu}\,\hat{u}}{\mathrm{Re}_e\,h_3^2}+$$
$$\frac{h_{1,y\,y}\,\overline{\mu}\,\hat{u}}{\mathrm{Re}_e\,h_1}+\frac{\left(h_{1,y}\right)^2\,\overline{\mu}\,\hat{u}}{\mathrm{Re}_e\,h_1^2}+\frac{2\,\alpha^2\,\overline{\mu}\,\hat{u}}{\mathrm{Re}_e\,h_1^2}+\frac{\alpha^2\,\overline{\lambda}\,\hat{u}}{\mathrm{Re}_e\,h_1^2}-\frac{\hat{T}\,\overline{\mu}_{\overline{T}}\,\overline{u}_{y\,y}}{\mathrm{Re}_e}-\frac{\overline{T}_y\,\hat{T}\,\overline{\mu}_{\overline{T}\,\overline{T}}\,\overline{u}_y}{\mathrm{Re}_e}-$$
$$\frac{\hat{T}\,h_{3,y}\,\overline{\mu}_{\overline{T}}\,\overline{u}_y}{\mathrm{Re}_e\,h_3}-\frac{\hat{T}\,h_{1,y}\,\overline{\mu}_{\overline{T}}\,\overline{u}_y}{\mathrm{Re}_e\,h_1}-\frac{\hat{T}_y\,\overline{\mu}_{\overline{T}}\,\overline{u}_y}{\mathrm{Re}_e}+\frac{\overline{T}_y\,\hat{T}\,h_{1,y}\,\overline{\mu}_{\overline{T}\,\overline{T}}\,\overline{u}}{\mathrm{Re}_e\,h_1}+\frac{\hat{T}\,h_{1,y}\,h_{3,y}\,\overline{\mu}_{\overline{T}}\,\overline{u}}{\mathrm{Re}_e\,h_1\,h_3}+$$
$$\frac{\hat{T}\,h_{1,y\,y}\,\overline{\mu}_{\overline{T}}\,\overline{u}}{\mathrm{Re}_e\,h_1}+\frac{\hat{T}\,\left(h_{1,y}\right)^2\,\overline{\mu}_{\overline{T}}\,\overline{u}}{\mathrm{Re}_e\,h_1^2}+\frac{\hat{T}_y\,h_{1,y}\,\overline{\mu}_{\overline{T}}\,\overline{u}}{\mathrm{Re}_e\,h_1}+\frac{i\,\overline{T}\,\alpha\,\hat{\rho}}{{\mathrm{M}_e}^2\,\gamma_e\,h_1}+\frac{i\,\hat{T}\,\alpha\,\overline{\rho}}{{\mathrm{M}_e}^2\,\gamma_e\,h_1}=0$$

B.2.2 Momentum along the y-Axis

$$-\frac{i\,\beta\,\overline{\mu}\,\hat{w}_y}{\mathrm{Re}_e\,h_3}-\frac{i\,\beta\,\overline{\lambda}\,\hat{w}_y}{\mathrm{Re}_e\,h_3}-\frac{2\,h_{3,y}\,\overline{\rho}\,\overline{w}\,\hat{w}}{h_3}+\frac{3\,i\,\beta\,h_{3,y}\,\overline{\mu}\,\hat{w}}{\mathrm{Re}_e\,h_3^2}-\frac{i\,\overline{T}_y\,\beta\,\overline{\lambda}_{\overline{T}}\,\hat{w}}{\mathrm{Re}_e\,h_3}+\frac{i\,\beta\,h_{3,y}\,\overline{\lambda}\,\hat{w}}{\mathrm{Re}_e\,h_3^2}-$$
$$\frac{i\,\hat{T}\,\beta\,\overline{\mu}_{\overline{T}}\,\overline{w}_y}{\mathrm{Re}_e\,h_3}-\frac{h_{3,y}\,\hat{\rho}\,\overline{w}^2}{h_3}+\frac{i\,\beta\,\overline{\rho}\,\hat{v}\,\overline{w}}{h_3}+\frac{i\,\hat{T}\,\beta\,h_{3,y}\,\overline{\mu}_{\overline{T}}\,\overline{w}}{\mathrm{Re}_e\,h_3^2}-\frac{2\,\overline{\mu}\,\hat{v}_{y\,y}}{\mathrm{Re}_e}-\frac{\overline{\lambda}\,\hat{v}_{y\,y}}{\mathrm{Re}_e}-\frac{2\,\overline{T}_y\,\overline{\mu}_{\overline{T}}\,\hat{v}_y}{\mathrm{Re}_e}-$$
$$\frac{2\,h_{3,y}\,\overline{\mu}\,\hat{v}_y}{\mathrm{Re}_e\,h_3}-\frac{2\,h_{1,y}\,\overline{\mu}\,\hat{v}_y}{\mathrm{Re}_e\,h_1}-\frac{\overline{T}_y\,\overline{\lambda}_{\overline{T}}\,\hat{v}_y}{\mathrm{Re}_e}-\frac{h_{3,y}\,\overline{\lambda}\,\hat{v}_y}{\mathrm{Re}_e\,h_3}-\frac{h_{1,y}\,\overline{\lambda}\,\hat{v}_y}{\mathrm{Re}_e\,h_1}+\frac{i\,\alpha\,\overline{\rho}\,\overline{u}\,\hat{v}}{h_1}-i\,\omega\,\overline{\rho}\,\hat{v}+$$
$$\frac{2\,\left(h_{3,y}\right)^2\,\overline{\mu}\,\hat{v}}{\mathrm{Re}_e\,h_3^2}+\frac{\beta^2\,\overline{\mu}\,\hat{v}}{\mathrm{Re}_e\,h_3^2}+\frac{2\,\left(h_{1,y}\right)^2\,\overline{\mu}\,\hat{v}}{\mathrm{Re}_e\,h_1^2}+\frac{\alpha^2\,\overline{\mu}\,\hat{v}}{\mathrm{Re}_e\,h_1^2}-\frac{\overline{T}_y\,h_{3,y}\,\overline{\lambda}_{\overline{T}}\,\hat{v}}{\mathrm{Re}_e\,h_3}-\frac{\overline{T}_y\,h_{1,y}\,\overline{\lambda}_{\overline{T}}\,\hat{v}}{\mathrm{Re}_e\,h_1}-$$
$$\frac{h_{3,y\,y}\,\overline{\lambda}\,\hat{v}}{\mathrm{Re}_e\,h_3}+\frac{\left(h_{3,y}\right)^2\,\overline{\lambda}\,\hat{v}}{\mathrm{Re}_e\,h_3^2}-\frac{h_{1,y\,y}\,\overline{\lambda}\,\hat{v}}{\mathrm{Re}_e\,h_1}+\frac{\left(h_{1,y}\right)^2\,\overline{\lambda}\,\hat{v}}{\mathrm{Re}_e\,h_1^2}-\frac{i\,\alpha\,\overline{\mu}\,\hat{u}_y}{\mathrm{Re}_e\,h_1}-\frac{i\,\alpha\,\overline{\lambda}\,\hat{u}_y}{\mathrm{Re}_e\,h_1}-\frac{2\,h_{1,y}\,\overline{\rho}\,\overline{u}\,\hat{u}}{h_1}+$$
$$\frac{3\,i\,\alpha\,h_{1,y}\,\overline{\mu}\,\hat{u}}{\mathrm{Re}_e\,h_1^2}-\frac{i\,\overline{T}_y\,\alpha\,\overline{\lambda}_{\overline{T}}\,\hat{u}}{\mathrm{Re}_e\,h_1}+\frac{i\,\alpha\,h_{1,y}\,\overline{\lambda}\,\hat{u}}{\mathrm{Re}_e\,h_1^2}-\frac{i\,\hat{T}\,\alpha\,\overline{\mu}_{\overline{T}}\,\overline{u}_y}{\mathrm{Re}_e\,h_1}-\frac{h_{1,y}\,\hat{\rho}\,\overline{u}^2}{h_1}+\frac{i\,\hat{T}\,\alpha\,h_{1,y}\,\overline{\mu}_{\overline{T}}\,\overline{u}}{\mathrm{Re}_e\,h_1^2}+$$
$$\frac{\overline{T}\,\hat{\rho}_y}{{\mathrm{M}_e}^2\,\gamma_e}+\frac{\overline{T}_y\,\hat{\rho}}{{\mathrm{M}_e}^2\,\gamma_e}+\frac{\hat{T}\,\overline{\rho}_y}{{\mathrm{M}_e}^2\,\gamma_e}+\frac{\hat{T}_y\,\overline{\rho}}{{\mathrm{M}_e}^2\,\gamma_e}=0$$

B.2.3 Momentum along the z-Axis

$$
\begin{gathered}
-\frac{\overline{\mu}\,\hat{w}_{y\,y}}{\mathrm{Re}_e}-\frac{\overline{T}_y\,\overline{\mu}_{\overline{T}}\,\hat{w}_y}{\mathrm{Re}_e}-\frac{h_{3,y}\,\overline{\mu}\,\hat{w}_y}{\mathrm{Re}_e\,h_3}-\frac{h_{1,y}\,\overline{\mu}\,\hat{w}_y}{\mathrm{Re}_e\,h_1}+\frac{i\,\beta\,\overline{\rho}\,\overline{w}\,\hat{w}}{h_3}+\frac{i\,\alpha\,\overline{\rho}\,\overline{u}\,\hat{w}}{h_1}-i\,\omega\,\overline{\rho}\,\hat{w}+\\
\frac{\overline{T}_y\,h_{3,y}\,\overline{\mu}_{\overline{T}}\,\hat{w}}{\mathrm{Re}_e\,h_3}+\frac{h_{3,y\,y}\,\overline{\mu}\,\hat{w}}{\mathrm{Re}_e\,h_3}+\frac{\left(h_{3,y}\right)^2\,\overline{\mu}\,\hat{w}}{\mathrm{Re}_e\,h_3^2}+\frac{h_{1,y}\,h_{3,y}\,\overline{\mu}\,\hat{w}}{\mathrm{Re}_e\,h_1\,h_3}+\frac{2\,\beta^2\,\overline{\mu}\,\hat{w}}{\mathrm{Re}_e\,h_3^2}+\frac{\alpha^2\,\overline{\mu}\,\hat{w}}{\mathrm{Re}_e\,h_1^2}+\frac{\beta^2\,\overline{\lambda}\,\hat{w}}{\mathrm{Re}_e\,h_3^2}-\\
\frac{\hat{T}\,\overline{\mu}_{\overline{T}}\,\overline{w}_{y\,y}}{\mathrm{Re}_e}+\overline{\rho}\,\hat{v}\,\overline{w}_y-\frac{\overline{T}_y\,\hat{T}\,\overline{\mu}_{\overline{T}\,\overline{T}}\,\overline{w}_y}{\mathrm{Re}_e}-\frac{\hat{T}\,h_{3,y}\,\overline{\mu}_{\overline{T}}\,\overline{w}_y}{\mathrm{Re}_e\,h_3}-\frac{\hat{T}\,h_{1,y}\,\overline{\mu}_{\overline{T}}\,\overline{w}_y}{\mathrm{Re}_e\,h_1}-\frac{\hat{T}_y\,\overline{\mu}_{\overline{T}}\,\overline{w}_y}{\mathrm{Re}_e}+\frac{h_{3,y}\,\overline{\rho}\,\hat{v}\,\overline{w}}{h_3}+\\
\frac{\overline{T}_y\,\hat{T}\,h_{3,y}\,\overline{\mu}_{\overline{T}\,\overline{T}}\,\overline{w}}{\mathrm{Re}_e\,h_3}+\frac{\hat{T}\,h_{3,y\,y}\,\overline{\mu}_{\overline{T}}\,\overline{w}}{\mathrm{Re}_e\,h_3}+\frac{\hat{T}\,\left(h_{3,y}\right)^2\,\overline{\mu}_{\overline{T}}\,\overline{w}}{\mathrm{Re}_e\,h_3^2}+\frac{\hat{T}\,h_{1,y}\,h_{3,y}\,\overline{\mu}_{\overline{T}}\,\overline{w}}{\mathrm{Re}_e\,h_1\,h_3}+\frac{\hat{T}_y\,h_{3,y}\,\overline{\mu}_{\overline{T}}\,\overline{w}}{\mathrm{Re}_e\,h_3}-\\
\frac{i\,\beta\,\overline{\mu}\,\hat{v}_y}{\mathrm{Re}_e\,h_3}-\frac{i\,\beta\,\overline{\lambda}\,\hat{v}_y}{\mathrm{Re}_e\,h_3}-\frac{i\,\overline{T}_y\,\beta\,\overline{\mu}_{\overline{T}}\,\hat{v}}{\mathrm{Re}_e\,h_3}-\frac{3\,i\,\beta\,h_{3,y}\,\overline{\mu}\,\hat{v}}{\mathrm{Re}_e\,h_3^2}-\frac{i\,\beta\,h_{1,y}\,\overline{\mu}\,\hat{v}}{\mathrm{Re}_e\,h_1\,h_3}-\frac{i\,\beta\,h_{3,y}\,\overline{\lambda}\,\hat{v}}{\mathrm{Re}_e\,h_3^2}-\\
\frac{i\,\beta\,h_{1,y}\,\overline{\lambda}\,\hat{v}}{\mathrm{Re}_e\,h_1\,h_3}+\frac{\alpha\,\beta\,\overline{\mu}\,\hat{u}}{\mathrm{Re}_e\,h_1\,h_3}+\frac{\alpha\,\beta\,\overline{\lambda}\,\hat{u}}{\mathrm{Re}_e\,h_1\,h_3}+\frac{i\,\overline{T}\,\beta\,\hat{\rho}}{{\mathrm{M}_e}^2\,\gamma_e\,h_3}+\frac{i\,\hat{T}\,\beta\,\overline{\rho}}{{\mathrm{M}_e}^2\,\gamma_e\,h_3}=0
\end{gathered}
$$

B.2.4 Conservation of Energy

$$
\begin{gathered}
-\frac{2\,\mathrm{Ec}_e\,\overline{\mu}\,\overline{w}_y\,\hat{w}_y}{\mathrm{Re}_e}+\frac{2\,\mathrm{Ec}_e\,h_{3,y}\,\overline{\mu}\,\overline{w}\,\hat{w}_y}{\mathrm{Re}_e\,h_3}+\frac{2\,\mathrm{Ec}_e\,h_{3,y}\,\overline{\mu}\,\overline{w}_y\,\hat{w}}{\mathrm{Re}_e\,h_3}-\frac{2\,\mathrm{Ec}_e\,\left(h_{3,y}\right)^2\,\overline{\mu}\,\overline{w}\,\hat{w}}{\mathrm{Re}_e\,h_3^2}-\\
\frac{\mathrm{Ec}_e\,\hat{T}\,\overline{\mu}_{\overline{T}}\,\left(\overline{w}_y\right)^2}{\mathrm{Re}_e}+\frac{2\,\mathrm{Ec}_e\,\hat{T}\,h_{3,y}\,\overline{\mu}_{\overline{T}}\,\overline{w}\,\overline{w}_y}{\mathrm{Re}_e\,h_3}-\frac{2\,i\,\mathrm{Ec}_e\,\beta\,\overline{\mu}\,\hat{v}\,\overline{w}_y}{\mathrm{Re}_e\,h_3}-\frac{\mathrm{Ec}_e\,\hat{T}\,\left(h_{3,y}\right)^2\,\overline{\mu}_{\overline{T}}\,\overline{w}^2}{\mathrm{Re}_e\,h_3^2}+\\
\frac{2\,i\,\mathrm{Ec}_e\,\beta\,h_{3,y}\,\overline{\mu}\,\hat{v}\,\overline{w}}{\mathrm{Re}_e\,h_3^2}-\frac{i\,\mathrm{Ec}_e\,\overline{T}\,\beta\,\hat{\rho}\,\overline{w}}{{\mathrm{M}_e}^2\,\gamma_e\,h_3}-\frac{i\,\mathrm{Ec}_e\,\hat{T}\,\beta\,\overline{\rho}\,\overline{w}}{{\mathrm{M}_e}^2\,\gamma_e\,h_3}+\frac{i\,\hat{T}\,\beta\,\overline{c}_p\,\overline{\rho}\,\overline{w}}{h_3}-\frac{2\,i\,\mathrm{Ec}_e\,\alpha\,\overline{\mu}\,\overline{u}_y\,\hat{v}}{\mathrm{Re}_e\,h_1}+\\
\frac{2\,i\,\mathrm{Ec}_e\,\alpha\,h_{1,y}\,\overline{\mu}\,\overline{u}\,\hat{v}}{\mathrm{Re}_e\,h_1^2}-\frac{\mathrm{Ec}_e\,\overline{T}\,\overline{\rho}_y\,\hat{v}}{{\mathrm{M}_e}^2\,\gamma_e}-\frac{\mathrm{Ec}_e\,\overline{T}_y\,\overline{\rho}\,\hat{v}}{{\mathrm{M}_e}^2\,\gamma_e}+\overline{T}_y\,\overline{c}_p\,\overline{\rho}\,\hat{v}-\frac{2\,\mathrm{Ec}_e\,\overline{\mu}\,\overline{u}_y\,\hat{u}_y}{\mathrm{Re}_e}+\frac{2\,\mathrm{Ec}_e\,h_{1,y}\,\overline{\mu}\,\overline{u}\,\hat{u}_y}{\mathrm{Re}_e\,h_1}+\\
\frac{2\,\mathrm{Ec}_e\,h_{1,y}\,\overline{\mu}\,\overline{u}_y\,\hat{u}}{\mathrm{Re}_e\,h_1}-\frac{2\,\mathrm{Ec}_e\,\left(h_{1,y}\right)^2\,\overline{\mu}\,\overline{u}\,\hat{u}}{\mathrm{Re}_e\,h_1^2}-\frac{\mathrm{Ec}_e\,\hat{T}\,\overline{\mu}_{\overline{T}}\,\left(\overline{u}_y\right)^2}{\mathrm{Re}_e}+\frac{2\,\mathrm{Ec}_e\,\hat{T}\,h_{1,y}\,\overline{\mu}_{\overline{T}}\,\overline{u}\,\overline{u}_y}{\mathrm{Re}_e\,h_1}-\\
\frac{\mathrm{Ec}_e\,\hat{T}\,\left(h_{1,y}\right)^2\,\overline{\mu}_{\overline{T}}\,\overline{u}^2}{\mathrm{Re}_e\,h_1^2}-\frac{i\,\mathrm{Ec}_e\,\overline{T}\,\alpha\,\hat{\rho}\,\overline{u}}{{\mathrm{M}_e}^2\,\gamma_e\,h_1}-\frac{i\,\mathrm{Ec}_e\,\hat{T}\,\alpha\,\overline{\rho}\,\overline{u}}{{\mathrm{M}_e}^2\,\gamma_e\,h_1}+\frac{i\,\hat{T}\,\alpha\,\overline{c}_p\,\overline{\rho}\,\overline{u}}{h_1}+\frac{i\,\mathrm{Ec}_e\,\overline{T}\,\omega\,\hat{\rho}}{{\mathrm{M}_e}^2\,\gamma_e}+\frac{i\,\mathrm{Ec}_e\,\hat{T}\,\omega\,\overline{\rho}}{{\mathrm{M}_e}^2\,\gamma_e}-\\
i\,\hat{T}\,\overline{c}_p\,\omega\,\overline{\rho}-\frac{\left(\overline{T}_y\right)^2\,\hat{T}\,\overline{\kappa}_{\overline{T}\,\overline{T}}}{\mathrm{Pr}_e\,\mathrm{Re}_e}-\frac{\overline{T}_y\,\hat{T}\,h_{3,y}\,\overline{\kappa}_{\overline{T}}}{\mathrm{Pr}_e\,\mathrm{Re}_e\,h_3}-\frac{\overline{T}_y\,\hat{T}\,h_{1,y}\,\overline{\kappa}_{\overline{T}}}{\mathrm{Pr}_e\,\mathrm{Re}_e\,h_1}-\frac{2\,\overline{T}_y\,\hat{T}_y\,\overline{\kappa}_{\overline{T}}}{\mathrm{Pr}_e\,\mathrm{Re}_e}-\frac{\overline{T}_{y\,y}\,\hat{T}\,\overline{\kappa}_{\overline{T}}}{\mathrm{Pr}_e\,\mathrm{Re}_e}-\\
\frac{\hat{T}_y\,h_{3,y}\,\overline{\kappa}}{\mathrm{Pr}_e\,\mathrm{Re}_e\,h_3}+\frac{\hat{T}\,\beta^2\,\overline{\kappa}}{\mathrm{Pr}_e\,\mathrm{Re}_e\,h_3^2}-\frac{\hat{T}_y\,h_{1,y}\,\overline{\kappa}}{\mathrm{Pr}_e\,\mathrm{Re}_e\,h_1}+\frac{\hat{T}\,\alpha^2\,\overline{\kappa}}{\mathrm{Pr}_e\,\mathrm{Re}_e\,h_1^2}-\frac{\hat{T}_{y\,y}\,\overline{\kappa}}{\mathrm{Pr}_e\,\mathrm{Re}_e}=0
\end{gathered}
$$

B.2.5 Continuity

$$\frac{i\,\beta\,\overline{\rho}\,\hat{w}}{h_3} + \frac{i\,\beta\,\hat{\rho}\,\overline{w}}{h_3} + \overline{\rho}\,\hat{v}_y + \overline{\rho}_y\,\hat{v} + \frac{h_{3,y}\,\overline{\rho}\,\hat{v}}{h_3} + \frac{h_{1,y}\,\overline{\rho}\,\hat{v}}{h_1} + \frac{i\,\alpha\,\overline{\rho}\,\hat{u}}{h_1} + \frac{i\,\alpha\,\hat{\rho}\,\overline{u}}{h_1} - i\,\omega\,\hat{\rho} = 0$$

B.3 LPSE Governing Equations

After applying all of the LPSE assumptions, the stability problem takes on a system of individual disturbance equations which are represented as:

$$\mathcal{A}\frac{\partial^2\hat{\phi}}{\partial y^2} + \mathcal{B}\frac{\partial^2\hat{\phi}}{\partial\tilde{s}\partial y} + \mathcal{C}\frac{\partial\hat{\phi}}{\partial y} + \mathcal{D}\frac{\partial\hat{\phi}}{\partial\tilde{s}} + \mathcal{E}\hat{\phi} = 0 \tag{B.2}$$

Here, $\hat{\phi}$ is the vector of flow variables $\left[\hat{u}, \hat{v}, \hat{w}, \hat{T}, \hat{\rho}\,\right]$, and $\mathcal{A}$, $\mathcal{B}$, $\mathcal{C}$, $\mathcal{D}$, and $\mathcal{E}$ are (5 $\times$ 5) matrices that exist at for each wall-normal location. Expanding all of the terms in Equation B.2 leads to the equations for $s, y, \text{and } z$ momentums, conservation of energy, and continuity as seen below. Throughout these equations, subscripts $s, y, \text{and } \overline{T}$ are independent variables of differentiation. Every other subscript is there for notation purposes only and does not imply any sort of differentiation. The scaling terms, h_1 and h_3, present in the LPSE equations are the same as seen throughout the LST equations. Throughout the LPSE equations, $\Omega_{\text{Re}}/Re_e \equiv \epsilon_s/Re_e$ and is the parameter used to track the slow varying viscous terms. The value of Ω_{Re} is assigned to be 1 for all cases throughout this study. Also, Ω_p tracks which terms are influenced by the streamwise gradient of the pressure shape function, i.e. $\partial\hat{p}/\partial\tilde{s}$. For all of the analysis presented throughout this study, this term is set equal to zero.

B.3.1 Momentum along the s-Axis

$$
-\frac{i\,\Omega_{\mathrm{Re}}\,\beta\,\overline{\mu}\,\hat{w}_s}{\mathrm{Re}_e\,h_1\,h_3}-\frac{i\,\Omega_{\mathrm{Re}}\,\beta\,\overline{\lambda}\,\hat{w}_s}{\mathrm{Re}_e\,h_1\,h_3}-\frac{2\,h_{3,s}\,\overline{\rho}\,\overline{w}\,\hat{w}}{h_1\,h_3}+\frac{3\,i\,\Omega_{\mathrm{Re}}\,\beta\,h_{3,s}\,\overline{\mu}\,\hat{w}}{\mathrm{Re}_e\,h_1\,h_3^2}+\frac{\alpha\,\beta\,\overline{\mu}\,\hat{w}}{\mathrm{Re}_e\,h_1\,h_3}-
$$

$$
\frac{i\,\Omega_{\mathrm{Re}}\,\overline{T}_s\,\beta\,\overline{\lambda}_{\overline{T}}\,\hat{w}}{\mathrm{Re}_e\,h_1\,h_3}+\frac{i\,\Omega_{\mathrm{Re}}\,\beta\,h_{3,s}\,\overline{\lambda}\,\hat{w}}{\mathrm{Re}_e\,h_1\,h_3^2}+\frac{\alpha\,\beta\,\overline{\lambda}\,\hat{w}}{\mathrm{Re}_e\,h_1\,h_3}-\frac{i\,\Omega_{\mathrm{Re}}\,\hat{T}\,\beta\,\overline{\mu}_{\overline{T}}\,\overline{w}_s}{\mathrm{Re}_e\,h_1\,h_3}-\frac{h_{3,s}\,\hat{\rho}\,\overline{w}^2}{h_1\,h_3}+
$$

$$
\frac{i\,\beta\,\overline{\rho}\,\hat{u}\,\overline{w}}{h_3}+\frac{i\,\Omega_{\mathrm{Re}}\,\hat{T}\,\beta\,h_{3,s}\,\overline{\mu}_{\overline{T}}\,\overline{w}}{\mathrm{Re}_e\,h_1\,h_3^2}-\frac{i\,\alpha\,\overline{\mu}\,\hat{v}_y}{\mathrm{Re}_e\,h_1}-\frac{\Omega_{\mathrm{Re}}\,\overline{T}_s\,\overline{\lambda}_{\overline{T}}\,\hat{v}_y}{\mathrm{Re}_e\,h_1}-\frac{i\,\alpha\,\overline{\lambda}\,\hat{v}_y}{\mathrm{Re}_e\,h_1}-\frac{\Omega_{\mathrm{Re}}\,\overline{\mu}\,\hat{v}_{s\,y}}{\mathrm{Re}_e\,h_1}-
$$

$$
\frac{\Omega_{\mathrm{Re}}\,\overline{\lambda}\,\hat{v}_{s\,y}}{\mathrm{Re}_e\,h_1}-\frac{\Omega_{\mathrm{Re}}\,\overline{T}_y\,\overline{\mu}_{\overline{T}}\,\hat{v}_s}{\mathrm{Re}_e\,h_1}-\frac{\Omega_{\mathrm{Re}}\,h_{3,y}\,\overline{\mu}\,\hat{v}_s}{\mathrm{Re}_e\,h_1\,h_3}-\frac{3\,\Omega_{\mathrm{Re}}\,h_{1,y}\,\overline{\mu}\,\hat{v}_s}{\mathrm{Re}_e\,h_1^2}-\frac{\Omega_{\mathrm{Re}}\,h_{3,y}\,\overline{\lambda}\,\hat{v}_s}{\mathrm{Re}_e\,h_1\,h_3}-
$$

$$
\frac{\Omega_{\mathrm{Re}}\,h_{1,y}\,\overline{\lambda}\,\hat{v}_s}{\mathrm{Re}_e\,h_1^2}+\overline{\rho}\,\overline{u}_y\,\hat{v}+\frac{h_{1,y}\,\overline{\rho}\,\overline{u}\,\hat{v}}{h_1}-\frac{2\,\Omega_{\mathrm{Re}}\,\overline{T}_s\,h_{1,y}\,\overline{\mu}_{\overline{T}}\,\hat{v}}{\mathrm{Re}_e\,h_1^2}-\frac{i\,\overline{T}_y\,\alpha\,\overline{\mu}_{\overline{T}}\,\hat{v}}{\mathrm{Re}_e\,h_1}+
$$

$$
\frac{2\,\Omega_{\mathrm{Re}}\,h_{3,s}\,h_{3,y}\,\overline{\mu}\,\hat{v}}{\mathrm{Re}_e\,h_1\,h_3^2}-\frac{i\,\alpha\,h_{3,y}\,\overline{\mu}\,\hat{v}}{\mathrm{Re}_e\,h_1\,h_3}-\frac{2\,\Omega_{\mathrm{Re}}\,h_{1,y}\,h_{3,s}\,\overline{\mu}\,\hat{v}}{\mathrm{Re}_e\,h_1^2\,h_3}+\frac{2\,\Omega_{\mathrm{Re}}\,h_{1,s}\,h_{1,y}\,\overline{\mu}\,\hat{v}}{\mathrm{Re}_e\,h_1^3}-\frac{3\,i\,\alpha\,h_{1,y}\,\overline{\mu}\,\hat{v}}{\mathrm{Re}_e\,h_1^2}-
$$

$$
\frac{2\,\Omega_{\mathrm{Re}}\,h_{1,s\,y}\,\overline{\mu}\,\hat{v}}{\mathrm{Re}_e\,h_1^2}-\frac{\Omega_{\mathrm{Re}}\,\overline{T}_s\,h_{3,y}\,\overline{\lambda}_{\overline{T}}\,\hat{v}}{\mathrm{Re}_e\,h_1\,h_3}-\frac{\Omega_{\mathrm{Re}}\,\overline{T}_s\,h_{1,y}\,\overline{\lambda}_{\overline{T}}\,\hat{v}}{\mathrm{Re}_e\,h_1^2}+\frac{\Omega_{\mathrm{Re}}\,h_{3,s}\,h_{3,y}\,\overline{\lambda}\,\hat{v}}{\mathrm{Re}_e\,h_1\,h_3^2}-\frac{i\,\alpha\,h_{3,y}\,\overline{\lambda}\,\hat{v}}{\mathrm{Re}_e\,h_1\,h_3}-
$$

$$
\frac{\Omega_{\mathrm{Re}}\,h_{3,s\,y}\,\overline{\lambda}\,\hat{v}}{\mathrm{Re}_e\,h_1\,h_3}+\frac{\Omega_{\mathrm{Re}}\,h_{1,s}\,h_{1,y}\,\overline{\lambda}\,\hat{v}}{\mathrm{Re}_e\,h_1^3}-\frac{i\,\alpha\,h_{1,y}\,\overline{\lambda}\,\hat{v}}{\mathrm{Re}_e\,h_1^2}-\frac{\Omega_{\mathrm{Re}}\,h_{1,s\,y}\,\overline{\lambda}\,\hat{v}}{\mathrm{Re}_e\,h_1^2}-\frac{i\,\Omega_{\mathrm{Re}}\,\hat{T}\,\alpha\,\overline{\lambda}_{\overline{T}}\,\overline{v}_y}{\mathrm{Re}_e\,h_1}+
$$

$$
\overline{\rho}\,\hat{u}_y\,\overline{v}+\frac{h_{1,y}\,\overline{\rho}\,\hat{u}\,\overline{v}}{h_1}+\hat{\rho}\,\overline{u}_y\,\overline{v}+\frac{h_{1,y}\,\hat{\rho}\,\overline{u}\,\overline{v}}{h_1}-\frac{2\,i\,\Omega_{\mathrm{Re}}\,\hat{T}\,\alpha\,h_{1,y}\,\overline{\mu}_{\overline{T}}\,\overline{v}}{\mathrm{Re}_e\,h_1^2}-\frac{i\,\Omega_{\mathrm{Re}}\,\hat{T}\,\alpha\,h_{3,y}\,\overline{\lambda}_{\overline{T}}\,\overline{v}}{\mathrm{Re}_e\,h_1\,h_3}-
$$

$$
\frac{i\,\Omega_{\mathrm{Re}}\,\hat{T}\,\alpha\,h_{1,y}\,\overline{\lambda}_{\overline{T}}\,\overline{v}}{\mathrm{Re}_e\,h_1^2}-\frac{\overline{\mu}\,\hat{u}_{y\,y}}{\mathrm{Re}_e}-\frac{\overline{T}_y\,\overline{\mu}_{\overline{T}}\,\hat{u}_y}{\mathrm{Re}_e}-\frac{h_{3,y}\,\overline{\mu}\,\hat{u}_y}{\mathrm{Re}_e\,h_3}-\frac{h_{1,y}\,\overline{\mu}\,\hat{u}_y}{\mathrm{Re}_e\,h_1}+\frac{\overline{\rho}\,\overline{u}\,\hat{u}_s}{h_1}-
$$

$$
\frac{4\,i\,\Omega_{\mathrm{Re}}\,\alpha\,\overline{\mu}\,\hat{u}_s}{\mathrm{Re}_e\,h_1^2}-\frac{2\,i\,\Omega_{\mathrm{Re}}\,\alpha\,\overline{\lambda}\,\hat{u}_s}{\mathrm{Re}_e\,h_1^2}+\frac{\overline{\rho}\,\overline{u}_s\,\hat{u}}{h_1}+\frac{i\,\alpha\,\overline{\rho}\,\overline{u}\,\hat{u}}{h_1}-i\,\omega\,\overline{\rho}\,\hat{u}+\frac{\overline{T}_y\,h_{1,y}\,\overline{\mu}_{\overline{T}}\,\hat{u}}{\mathrm{Re}_e\,h_1}-
$$

$$
\frac{2\,i\,\Omega_{\mathrm{Re}}\,\overline{T}_s\,\alpha\,\overline{\mu}_{\overline{T}}\,\hat{u}}{\mathrm{Re}_e\,h_1^2}+\frac{h_{1,y}\,h_{3,y}\,\overline{\mu}\,\hat{u}}{\mathrm{Re}_e\,h_1\,h_3}-\frac{2\,i\,\Omega_{\mathrm{Re}}\,\alpha\,h_{3,s}\,\overline{\mu}\,\hat{u}}{\mathrm{Re}_e\,h_1^2\,h_3}+\frac{\beta^2\,\overline{\mu}\,\hat{u}}{\mathrm{Re}_e\,h_3^2}+\frac{h_{1,y\,y}\,\overline{\mu}\,\hat{u}}{\mathrm{Re}_e\,h_1}+
$$

$$
\frac{(h_{1,y})^2\,\overline{\mu}\,\hat{u}}{\mathrm{Re}_e\,h_1^2}+\frac{2\,i\,\Omega_{\mathrm{Re}}\,\alpha\,h_{1,s}\,\overline{\mu}\,\hat{u}}{\mathrm{Re}_e\,h_1^3}-\frac{2\,i\,\Omega_{\mathrm{Re}}\,\alpha_s\,\overline{\mu}\,\hat{u}}{\mathrm{Re}_e\,h_1^2}+\frac{2\,\alpha^2\,\overline{\mu}\,\hat{u}}{\mathrm{Re}_e\,h_1^2}-\frac{i\,\Omega_{\mathrm{Re}}\,\overline{T}_s\,\alpha\,\overline{\lambda}_{\overline{T}}\,\hat{u}}{\mathrm{Re}_e\,h_1^2}-
$$

$$
\frac{i\,\Omega_{\mathrm{Re}}\,\alpha\,h_{3,s}\,\overline{\lambda}\,\hat{u}}{\mathrm{Re}_e\,h_1^2\,h_3}+\frac{i\,\Omega_{\mathrm{Re}}\,\alpha\,h_{1,s}\,\overline{\lambda}\,\hat{u}}{\mathrm{Re}_e\,h_1^3}-\frac{i\,\Omega_{\mathrm{Re}}\,\alpha_s\,\overline{\lambda}\,\hat{u}}{\mathrm{Re}_e\,h_1^2}+\frac{\alpha^2\,\overline{\lambda}\,\hat{u}}{\mathrm{Re}_e\,h_1^2}-\frac{\hat{T}\,\overline{\mu}_{\overline{T}}\,\overline{u}_{y\,y}}{\mathrm{Re}_e}-\frac{\overline{T}_y\,\hat{T}\,\overline{\mu}_{\overline{T}\,\overline{T}}\,\overline{u}_y}{\mathrm{Re}_e}-
$$

$$
\frac{\hat{T}\,h_{3,y}\,\overline{\mu}_{\overline{T}}\,\overline{u}_y}{\mathrm{Re}_e\,h_3}-\frac{\hat{T}\,h_{1,y}\,\overline{\mu}_{\overline{T}}\,\overline{u}_y}{\mathrm{Re}_e\,h_1}-\frac{\hat{T}_y\,\overline{\mu}_{\overline{T}}\,\overline{u}_y}{\mathrm{Re}_e}+\frac{\hat{\rho}\,\overline{u}\,\overline{u}_s}{h_1}-\frac{2\,i\,\Omega_{\mathrm{Re}}\,\hat{T}\,\alpha\,\overline{\mu}_{\overline{T}}\,\overline{u}_s}{\mathrm{Re}_e\,h_1^2}-\frac{i\,\Omega_{\mathrm{Re}}\,\hat{T}\,\alpha\,\overline{\lambda}_{\overline{T}}\,\overline{u}_s}{\mathrm{Re}_e\,h_1^2}+
$$

$$
\frac{\overline{T}_y\,\hat{T}\,h_{1,y}\,\overline{\mu}_{\overline{T}\,\overline{T}}\,\overline{u}}{\mathrm{Re}_e\,h_1}+\frac{\hat{T}\,h_{1,y}\,h_{3,y}\,\overline{\mu}_{\overline{T}}\,\overline{u}}{\mathrm{Re}_e\,h_1\,h_3}+\frac{\hat{T}\,h_{1,y\,y}\,\overline{\mu}_{\overline{T}}\,\overline{u}}{\mathrm{Re}_e\,h_1}+\frac{\hat{T}\,(h_{1,y})^2\,\overline{\mu}_{\overline{T}}\,\overline{u}}{\mathrm{Re}_e\,h_1^2}+\frac{\hat{T}_y\,h_{1,y}\,\overline{\mu}_{\overline{T}}\,\overline{u}}{\mathrm{Re}_e\,h_1}-
$$

$$\frac{i\,\Omega_{\mathrm{Re}}\,\hat{T}\,\alpha\,h_{3,s}\,\overline{\lambda}_{\overline{T}}\,\overline{u}}{\mathrm{Re}_e\,h_1^2\,h_3}+\frac{\Omega_p\,\overline{T}\,\hat{\rho}_s}{{\mathrm{M}_e}^2\,\gamma_e\,h_1}+\frac{i\,\Omega_p\,\overline{T}\,\alpha\,\hat{\rho}}{{\mathrm{M}_e}^2\,\gamma_e\,h_1}+\frac{\Omega_p\,\overline{T}_s\,\hat{\rho}}{{\mathrm{M}_e}^2\,\gamma_e\,h_1}+$$
$$\frac{\Omega_p\,\hat{T}\,\overline{\rho}_s}{{\mathrm{M}_e}^2\,\gamma_e\,h_1}+\frac{i\,\Omega_p\,\hat{T}\,\alpha\,\overline{\rho}}{{\mathrm{M}_e}^2\,\gamma_e\,h_1}+\frac{\Omega_p\,\hat{T}_s\,\overline{\rho}}{{\mathrm{M}_e}^2\,\gamma_e\,h_1}=0$$

B.3.2 Momentum along the y-Axis

$$-\frac{i\,\beta\,\overline{\mu}\,\hat{w}_y}{\mathrm{Re}_e\,h_3}-\frac{i\,\beta\,\overline{\lambda}\,\hat{w}_y}{\mathrm{Re}_e\,h_3}-\frac{2\,h_{3,y}\,\overline{\rho}\,\overline{w}\,\hat{w}}{h_3}+\frac{3\,i\,\beta\,h_{3,y}\,\overline{\mu}\,\hat{w}}{\mathrm{Re}_e\,h_3^2}-\frac{i\,\overline{T}_y\,\beta\,\overline{\lambda}_{\overline{T}}\,\hat{w}}{\mathrm{Re}_e\,h_3}+\frac{i\,\beta\,h_{3,y}\,\overline{\lambda}\,\hat{w}}{\mathrm{Re}_e\,h_3^2}-$$
$$\frac{i\,\hat{T}\,\beta\,\overline{\mu}_{\overline{T}}\,\overline{w}_y}{\mathrm{Re}_e\,h_3}-\frac{h_{3,y}\,\hat{\rho}\,\overline{w}^2}{h_3}+\frac{i\,\beta\,\overline{\rho}\,\hat{v}\,\overline{w}}{h_3}+\frac{i\,\hat{T}\,\beta\,h_{3,y}\,\overline{\mu}_{\overline{T}}\,\overline{w}}{\mathrm{Re}_e\,h_3^2}-\frac{2\,\overline{\mu}\,\hat{v}_{y\,y}}{\mathrm{Re}_e}-\frac{\overline{\lambda}\,\hat{v}_{y\,y}}{\mathrm{Re}_e}+\overline{\rho}\,\overline{v}\,\hat{v}_y-$$
$$\frac{2\,\overline{T}_y\,\overline{\mu}_{\overline{T}}\,\hat{v}_y}{\mathrm{Re}_e}-\frac{2\,h_{3,y}\,\overline{\mu}\,\hat{v}_y}{\mathrm{Re}_e\,h_3}-\frac{2\,h_{1,y}\,\overline{\mu}\,\hat{v}_y}{\mathrm{Re}_e\,h_1}-\frac{\overline{T}_y\,\overline{\lambda}_{\overline{T}}\,\hat{v}_y}{\mathrm{Re}_e}-\frac{h_{3,y}\,\overline{\lambda}\,\hat{v}_y}{\mathrm{Re}_e\,h_3}-\frac{h_{1,y}\,\overline{\lambda}\,\hat{v}_y}{\mathrm{Re}_e\,h_1}+\frac{\overline{\rho}\,\overline{u}\,\hat{v}_s}{h_1}-$$
$$\frac{2\,i\,\Omega_{\mathrm{Re}}\,\alpha\,\overline{\mu}\,\hat{v}_s}{\mathrm{Re}_e\,h_1^2}+\overline{\rho}\,\overline{v}_y\,\hat{v}+\frac{i\,\alpha\,\overline{\rho}\,\overline{u}\,\hat{v}}{h_1}-i\,\omega\,\overline{\rho}\,\hat{v}-\frac{i\,\Omega_{\mathrm{Re}}\,\overline{T}_s\,\alpha\,\overline{\mu}_{\overline{T}}\,\hat{v}}{\mathrm{Re}_e\,h_1^2}+\frac{2\,{(h_{3,y})}^2\,\overline{\mu}\,\hat{v}}{\mathrm{Re}_e\,h_3^2}-$$
$$\frac{i\,\Omega_{\mathrm{Re}}\,\alpha\,h_{3,s}\,\overline{\mu}\,\hat{v}}{\mathrm{Re}_e\,h_1^2\,h_3}+\frac{\beta^2\,\overline{\mu}\,\hat{v}}{\mathrm{Re}_e\,h_3^2}+\frac{2\,{(h_{1,y})}^2\,\overline{\mu}\,\hat{v}}{\mathrm{Re}_e\,h_1^2}+\frac{i\,\Omega_{\mathrm{Re}}\,\alpha\,h_{1,s}\,\overline{\mu}\,\hat{v}}{\mathrm{Re}_e\,h_1^3}-\frac{i\,\Omega_{\mathrm{Re}}\,\alpha_s\,\overline{\mu}\,\hat{v}}{\mathrm{Re}_e\,h_1^2}+\frac{\alpha^2\,\overline{\mu}\,\hat{v}}{\mathrm{Re}_e\,h_1^2}-$$
$$\frac{\overline{T}_y\,h_{3,y}\,\overline{\lambda}_{\overline{T}}\,\hat{v}}{\mathrm{Re}_e\,h_3}-\frac{\overline{T}_y\,h_{1,y}\,\overline{\lambda}_{\overline{T}}\,\hat{v}}{\mathrm{Re}_e\,h_1}-\frac{h_{3,y\,y}\,\overline{\lambda}\,\hat{v}}{\mathrm{Re}_e\,h_3}+\frac{{(h_{3,y})}^2\,\overline{\lambda}\,\hat{v}}{\mathrm{Re}_e\,h_3^2}-\frac{h_{1,y\,y}\,\overline{\lambda}\,\hat{v}}{\mathrm{Re}_e\,h_1}+\frac{{(h_{1,y})}^2\,\overline{\lambda}\,\hat{v}}{\mathrm{Re}_e\,h_1^2}-$$
$$\frac{2\,\Omega_{\mathrm{Re}}\,\hat{T}\,\overline{\mu}_{\overline{T}}\,\overline{v}_{y\,y}}{\mathrm{Re}_e}-\frac{\Omega_{\mathrm{Re}}\,\hat{T}\,\overline{\lambda}_{\overline{T}}\,\overline{v}_{y\,y}}{\mathrm{Re}_e}-\frac{2\,\Omega_{\mathrm{Re}}\,\overline{T}_y\,\hat{T}\,\overline{\mu}_{\overline{T}\,\overline{T}}\,\overline{v}_y}{\mathrm{Re}_e}-\frac{2\,\Omega_{\mathrm{Re}}\,\hat{T}\,h_{3,y}\,\overline{\mu}_{\overline{T}}\,\overline{v}_y}{\mathrm{Re}_e\,h_3}-$$
$$\frac{2\,\Omega_{\mathrm{Re}}\,\hat{T}\,h_{1,y}\,\overline{\mu}_{\overline{T}}\,\overline{v}_y}{\mathrm{Re}_e\,h_1}-\frac{2\,\Omega_{\mathrm{Re}}\,\hat{T}_y\,\overline{\mu}_{\overline{T}}\,\overline{v}_y}{\mathrm{Re}_e}-\frac{\Omega_{\mathrm{Re}}\,\overline{T}_y\,\hat{T}\,\overline{\lambda}_{\overline{T}\,\overline{T}}\,\overline{v}_y}{\mathrm{Re}_e}-\frac{\Omega_{\mathrm{Re}}\,\hat{T}\,h_{3,y}\,\overline{\lambda}_{\overline{T}}\,\overline{v}_y}{\mathrm{Re}_e\,h_3}-$$
$$\frac{\Omega_{\mathrm{Re}}\,\hat{T}\,h_{1,y}\,\overline{\lambda}_{\overline{T}}\,\overline{v}_y}{\mathrm{Re}_e\,h_1}-\frac{\Omega_{\mathrm{Re}}\,\hat{T}_y\,\overline{\lambda}_{\overline{T}}\,\overline{v}_y}{\mathrm{Re}_e}+\frac{2\,\Omega_{\mathrm{Re}}\,\hat{T}\,{(h_{3,y})}^2\,\overline{\mu}_{\overline{T}}\,\overline{v}}{\mathrm{Re}_e\,h_3^2}+\frac{2\,\Omega_{\mathrm{Re}}\,\hat{T}\,{(h_{1,y})}^2\,\overline{\mu}_{\overline{T}}\,\overline{v}}{\mathrm{Re}_e\,h_1^2}-$$
$$\frac{\Omega_{\mathrm{Re}}\,\overline{T}_y\,\hat{T}\,h_{3,y}\,\overline{\lambda}_{\overline{T}\,\overline{T}}\,\overline{v}}{\mathrm{Re}_e\,h_3}-\frac{\Omega_{\mathrm{Re}}\,\overline{T}_y\,\hat{T}\,h_{1,y}\,\overline{\lambda}_{\overline{T}\,\overline{T}}\,\overline{v}}{\mathrm{Re}_e\,h_1}-\frac{\Omega_{\mathrm{Re}}\,\hat{T}\,h_{3,y\,y}\,\overline{\lambda}_{\overline{T}}\,\overline{v}}{\mathrm{Re}_e\,h_3}+\frac{\Omega_{\mathrm{Re}}\,\hat{T}\,{(h_{3,y})}^2\,\overline{\lambda}_{\overline{T}}\,\overline{v}}{\mathrm{Re}_e\,h_3^2}-$$
$$\frac{\Omega_{\mathrm{Re}}\,\hat{T}_y\,h_{3,y}\,\overline{\lambda}_{\overline{T}}\,\overline{v}}{\mathrm{Re}_e\,h_3}-\frac{\Omega_{\mathrm{Re}}\,\hat{T}\,h_{1,y\,y}\,\overline{\lambda}_{\overline{T}}\,\overline{v}}{\mathrm{Re}_e\,h_1}+\frac{\Omega_{\mathrm{Re}}\,\hat{T}\,{(h_{1,y})}^2\,\overline{\lambda}_{\overline{T}}\,\overline{v}}{\mathrm{Re}_e\,h_1^2}-\frac{\Omega_{\mathrm{Re}}\,\hat{T}_y\,h_{1,y}\,\overline{\lambda}_{\overline{T}}\,\overline{v}}{\mathrm{Re}_e\,h_1}-$$
$$\frac{\Omega_{\mathrm{Re}}\,\overline{T}_s\,\overline{\mu}_{\overline{T}}\,\hat{u}_y}{\mathrm{Re}_e\,h_1}-\frac{\Omega_{\mathrm{Re}}\,h_{3,s}\,\overline{\mu}\,\hat{u}_y}{\mathrm{Re}_e\,h_1\,h_3}-\frac{i\,\alpha\,\overline{\mu}\,\hat{u}_y}{\mathrm{Re}_e\,h_1}-\frac{\Omega_{\mathrm{Re}}\,h_{3,s}\,\overline{\lambda}\,\hat{u}_y}{\mathrm{Re}_e\,h_1\,h_3}-\frac{i\,\alpha\,\overline{\lambda}\,\hat{u}_y}{\mathrm{Re}_e\,h_1}-\frac{\Omega_{\mathrm{Re}}\,\overline{\mu}\,\hat{u}_{s\,y}}{\mathrm{Re}_e\,h_1}-$$
$$\frac{\Omega_{\mathrm{Re}}\,\overline{\lambda}\,\hat{u}_{s\,y}}{\mathrm{Re}_e\,h_1}+\frac{3\,\Omega_{\mathrm{Re}}\,h_{1,y}\,\overline{\mu}\,\hat{u}_s}{\mathrm{Re}_e\,h_1^2}-\frac{\Omega_{\mathrm{Re}}\,\overline{T}_y\,\overline{\lambda}_{\overline{T}}\,\hat{u}_s}{\mathrm{Re}_e\,h_1}+\frac{\Omega_{\mathrm{Re}}\,h_{1,y}\,\overline{\lambda}\,\hat{u}_s}{\mathrm{Re}_e\,h_1^2}-\frac{2\,h_{1,y}\,\overline{\rho}\,\overline{u}\,\hat{u}}{h_1}+$$
$$\frac{\Omega_{\mathrm{Re}}\,\overline{T}_s\,h_{1,y}\,\overline{\mu}_{\overline{T}}\,\hat{u}}{\mathrm{Re}_e\,h_1^2}+\frac{2\,\Omega_{\mathrm{Re}}\,h_{3,s}\,h_{3,y}\,\overline{\mu}\,\hat{u}}{\mathrm{Re}_e\,h_1\,h_3^2}+\frac{\Omega_{\mathrm{Re}}\,h_{1,y}\,h_{3,s}\,\overline{\mu}\,\hat{u}}{\mathrm{Re}_e\,h_1^2\,h_3}-\frac{\Omega_{\mathrm{Re}}\,h_{1,s}\,h_{1,y}\,\overline{\mu}\,\hat{u}}{\mathrm{Re}_e\,h_1^3}+$$

$$\frac{3\,i\,\alpha\,h_{1,y}\,\overline{\mu}\,\hat{u}}{\mathrm{Re}_e\,h_1^2}+\frac{\Omega_{\mathrm{Re}}\,h_{1,s\,y}\,\overline{\mu}\,\hat{u}}{\mathrm{Re}_e\,h_1^2}-\frac{\Omega_{\mathrm{Re}}\,\overline{T}_y\,h_{3,s}\,\overline{\lambda}_{\overline{T}}\,\hat{u}}{\mathrm{Re}_e\,h_1\,h_3}-\frac{i\,\overline{T}_y\,\alpha\,\overline{\lambda}_{\overline{T}}\,\hat{u}}{\mathrm{Re}_e\,h_1}+\frac{\Omega_{\mathrm{Re}}\,h_{3,s}\,h_{3,y}\,\overline{\lambda}\,\hat{u}}{\mathrm{Re}_e\,h_1\,h_3^2}-$$
$$\frac{\Omega_{\mathrm{Re}}\,h_{3,s\,y}\,\overline{\lambda}\,\hat{u}}{\mathrm{Re}_e\,h_1\,h_3}+\frac{\Omega_{\mathrm{Re}}\,h_{1,y}\,h_{3,s}\,\overline{\lambda}\,\hat{u}}{\mathrm{Re}_e\,h_1^2\,h_3}+\frac{i\,\alpha\,h_{1,y}\,\overline{\lambda}\,\hat{u}}{\mathrm{Re}_e\,h_1^2}-\frac{\Omega_{\mathrm{Re}}\,\overline{T}_s\,\hat{T}\,\overline{\mu}_{\overline{T}\,\overline{T}}\,\overline{u}_y}{\mathrm{Re}_e\,h_1}-\frac{\Omega_{\mathrm{Re}}\,\hat{T}\,h_{3,s}\,\overline{\mu}_{\overline{T}}\,\overline{u}_y}{\mathrm{Re}_e\,h_1\,h_3}-$$
$$\frac{i\,\hat{T}\,\alpha\,\overline{\mu}_{\overline{T}}\,\overline{u}_y}{\mathrm{Re}_e\,h_1}-\frac{\Omega_{\mathrm{Re}}\,\hat{T}_s\,\overline{\mu}_{\overline{T}}\,\overline{u}_y}{\mathrm{Re}_e\,h_1}-\frac{\Omega_{\mathrm{Re}}\,\hat{T}\,h_{3,s}\,\overline{\lambda}_{\overline{T}}\,\overline{u}_y}{\mathrm{Re}_e\,h_1\,h_3}-\frac{\Omega_{\mathrm{Re}}\,\hat{T}\,\overline{\mu}_{\overline{T}}\,\overline{u}_{s\,y}}{\mathrm{Re}_e\,h_1}-\frac{\Omega_{\mathrm{Re}}\,\hat{T}\,\overline{\lambda}_{\overline{T}}\,\overline{u}_{s\,y}}{\mathrm{Re}_e\,h_1}+$$
$$\frac{3\,\Omega_{\mathrm{Re}}\,\hat{T}\,h_{1,y}\,\overline{\mu}_{\overline{T}}\,\overline{u}_s}{\mathrm{Re}_e\,h_1^2}-\frac{\Omega_{\mathrm{Re}}\,\overline{T}_y\,\hat{T}\,\overline{\lambda}_{\overline{T}\,\overline{T}}\,\overline{u}_s}{\mathrm{Re}_e\,h_1}+\frac{\Omega_{\mathrm{Re}}\,\hat{T}\,h_{1,y}\,\overline{\lambda}_{\overline{T}}\,\overline{u}_s}{\mathrm{Re}_e\,h_1^2}-\frac{\Omega_{\mathrm{Re}}\,\hat{T}_y\,\overline{\lambda}_{\overline{T}}\,\overline{u}_s}{\mathrm{Re}_e\,h_1}-\frac{h_{1,y}\,\hat{\rho}\,\overline{u}^2}{h_1}+$$
$$\frac{\Omega_{\mathrm{Re}}\,\overline{T}_s\,\hat{T}\,h_{1,y}\,\overline{\mu}_{\overline{T}\,\overline{T}}\,\overline{u}}{\mathrm{Re}_e\,h_1^2}+\frac{2\,\Omega_{\mathrm{Re}}\,\hat{T}\,h_{3,s}\,h_{3,y}\,\overline{\mu}_{\overline{T}}\,\overline{u}}{\mathrm{Re}_e\,h_1\,h_3^2}+\frac{\Omega_{\mathrm{Re}}\,\hat{T}\,h_{1,y}\,h_{3,s}\,\overline{\mu}_{\overline{T}}\,\overline{u}}{\mathrm{Re}_e\,h_1^2\,h_3}-\frac{\Omega_{\mathrm{Re}}\,\hat{T}\,h_{1,s}\,h_{1,y}\,\overline{\mu}_{\overline{T}}\,\overline{u}}{\mathrm{Re}_e\,h_1^3}+$$
$$\frac{i\,\hat{T}\,\alpha\,h_{1,y}\,\overline{\mu}_{\overline{T}}\,\overline{u}}{\mathrm{Re}_e\,h_1^2}+\frac{\Omega_{\mathrm{Re}}\,\hat{T}_s\,h_{1,y}\,\overline{\mu}_{\overline{T}}\,\overline{u}}{\mathrm{Re}_e\,h_1^2}+\frac{\Omega_{\mathrm{Re}}\,\hat{T}\,h_{1,s\,y}\,\overline{\mu}_{\overline{T}}\,\overline{u}}{\mathrm{Re}_e\,h_1^2}-\frac{\Omega_{\mathrm{Re}}\,\overline{T}_y\,\hat{T}\,h_{3,s}\,\overline{\lambda}_{\overline{T}\,\overline{T}}\,\overline{u}}{\mathrm{Re}_e\,h_1\,h_3}+$$
$$\frac{\Omega_{\mathrm{Re}}\,\hat{T}\,h_{3,s}\,h_{3,y}\,\overline{\lambda}_{\overline{T}}\,\overline{u}}{\mathrm{Re}_e\,h_1\,h_3^2}-\frac{\Omega_{\mathrm{Re}}\,\hat{T}\,h_{3,s\,y}\,\overline{\lambda}_{\overline{T}}\,\overline{u}}{\mathrm{Re}_e\,h_1\,h_3}+\frac{\Omega_{\mathrm{Re}}\,\hat{T}\,h_{1,y}\,h_{3,s}\,\overline{\lambda}_{\overline{T}}\,\overline{u}}{\mathrm{Re}_e\,h_1^2\,h_3}-\frac{\Omega_{\mathrm{Re}}\,\hat{T}_y\,h_{3,s}\,\overline{\lambda}_{\overline{T}}\,\overline{u}}{\mathrm{Re}_e\,h_1\,h_3}+$$
$$\frac{\overline{T}\,\hat{\rho}_y}{\mathrm{M}_e{}^2\,\gamma_e}+\frac{\overline{T}_y\,\hat{\rho}}{\mathrm{M}_e{}^2\,\gamma_e}+\frac{\hat{T}\,\overline{\rho}_y}{\mathrm{M}_e{}^2\,\gamma_e}+\frac{\hat{T}_y\,\overline{\rho}}{\mathrm{M}_e{}^2\,\gamma_e}=0$$

B.3.3 Momentum along the z-Axis

$$
\begin{aligned}
&-\frac{\overline{\mu}\,\hat{w}_{y\,y}}{\mathrm{Re}_e}+\overline{\rho}\,\overline{v}\,\hat{w}_y-\frac{\overline{T}_y\,\overline{\mu}_{\overline{T}}\,\hat{w}_y}{\mathrm{Re}_e}-\frac{h_{3,y}\,\overline{\mu}\,\hat{w}_y}{\mathrm{Re}_e\,h_3}-\frac{h_{1,y}\,\overline{\mu}\,\hat{w}_y}{\mathrm{Re}_e\,h_1}+\frac{\overline{\rho}\,\overline{u}\,\hat{w}_s}{h_1}-\frac{2\,i\,\Omega_{\mathrm{Re}}\,\alpha\,\overline{\mu}\,\hat{w}_s}{\mathrm{Re}_e\,h_1^2}+\\
&\frac{i\,\beta\,\overline{\rho}\,\overline{w}\,\hat{w}}{h_3}+\frac{h_{3,y}\,\overline{\rho}\,\overline{v}\,\hat{w}}{h_3}+\frac{h_{3,s}\,\overline{\rho}\,\overline{u}\,\hat{w}}{h_1\,h_3}+\frac{i\,\alpha\,\overline{\rho}\,\overline{u}\,\hat{w}}{h_1}-i\,\omega\,\overline{\rho}\,\hat{w}+\frac{\overline{T}_y\,h_{3,y}\,\overline{\mu}_{\overline{T}}\,\hat{w}}{\mathrm{Re}_e\,h_3}-\frac{i\,\Omega_{\mathrm{Re}}\,\overline{T}_s\,\alpha\,\overline{\mu}_{\overline{T}}\,\hat{w}}{\mathrm{Re}_e\,h_1^2}+\\
&\frac{h_{3,y\,y}\,\overline{\mu}\,\hat{w}}{\mathrm{Re}_e\,h_3}+\frac{\left(h_{3,y}\right)^2\,\overline{\mu}\,\hat{w}}{\mathrm{Re}_e\,h_3^2}+\frac{h_{1,y}\,h_{3,y}\,\overline{\mu}\,\hat{w}}{\mathrm{Re}_e\,h_1\,h_3}-\frac{i\,\Omega_{\mathrm{Re}}\,\alpha\,h_{3,s}\,\overline{\mu}\,\hat{w}}{\mathrm{Re}_e\,h_1^2\,h_3}+\frac{2\,\beta^2\,\overline{\mu}\,\hat{w}}{\mathrm{Re}_e\,h_3^2}+\frac{i\,\Omega_{\mathrm{Re}}\,\alpha\,h_{1,s}\,\overline{\mu}\,\hat{w}}{\mathrm{Re}_e\,h_1^3}-\\
&\frac{i\,\Omega_{\mathrm{Re}}\,\alpha_s\,\overline{\mu}\,\hat{w}}{\mathrm{Re}_e\,h_1^2}+\frac{\alpha^2\,\overline{\mu}\,\hat{w}}{\mathrm{Re}_e\,h_1^2}+\frac{\beta^2\,\overline{\lambda}\,\hat{w}}{\mathrm{Re}_e\,h_3^2}-\frac{\hat{T}\,\overline{\mu}_{\overline{T}}\,\overline{w}_{y\,y}}{\mathrm{Re}_e}+\overline{\rho}\,\hat{v}\,\overline{w}_y+\hat{\rho}\,\overline{v}\,\overline{w}_y-\frac{\overline{T}_y\,\hat{T}\,\overline{\mu}_{\overline{T}\,\overline{T}}\,\overline{w}_y}{\mathrm{Re}_e}-\\
&\frac{\hat{T}\,h_{3,y}\,\overline{\mu}_{\overline{T}}\,\overline{w}_y}{\mathrm{Re}_e\,h_3}-\frac{\hat{T}\,h_{1,y}\,\overline{\mu}_{\overline{T}}\,\overline{w}_y}{\mathrm{Re}_e\,h_1}-\frac{\hat{T}_y\,\overline{\mu}_{\overline{T}}\,\overline{w}_y}{\mathrm{Re}_e}+\frac{\overline{\rho}\,\hat{u}\,\overline{w}_s}{h_1}+\frac{\hat{\rho}\,\overline{u}\,\overline{w}_s}{h_1}-\frac{i\,\Omega_{\mathrm{Re}}\,\hat{T}\,\alpha\,\overline{\mu}_{\overline{T}}\,\overline{w}_s}{\mathrm{Re}_e\,h_1^2}+\\
&\frac{h_{3,y}\,\overline{\rho}\,\hat{v}\,\overline{w}}{h_3}+\frac{h_{3,y}\,\hat{\rho}\,\overline{v}\,\overline{w}}{h_3}+\frac{h_{3,s}\,\overline{\rho}\,\hat{u}\,\overline{w}}{h_1\,h_3}+\frac{h_{3,s}\,\hat{\rho}\,\overline{u}\,\overline{w}}{h_1\,h_3}+\frac{\overline{T}_y\,\hat{T}\,h_{3,y}\,\overline{\mu}_{\overline{T}\,\overline{T}}\,\overline{w}}{\mathrm{Re}_e\,h_3}+\frac{\hat{T}\,h_{3,y\,y}\,\overline{\mu}_{\overline{T}}\,\overline{w}}{\mathrm{Re}_e\,h_3}+\\
&\frac{\hat{T}\,\left(h_{3,y}\right)^2\,\overline{\mu}_{\overline{T}}\,\overline{w}}{\mathrm{Re}_e\,h_3^2}+\frac{\hat{T}\,h_{1,y}\,h_{3,y}\,\overline{\mu}_{\overline{T}}\,\overline{w}}{\mathrm{Re}_e\,h_1\,h_3}+\frac{\hat{T}_y\,h_{3,y}\,\overline{\mu}_{\overline{T}}\,\overline{w}}{\mathrm{Re}_e\,h_3}+\frac{i\,\Omega_{\mathrm{Re}}\,\hat{T}\,\alpha\,h_{3,s}\,\overline{\mu}_{\overline{T}}\,\overline{w}}{\mathrm{Re}_e\,h_1^2\,h_3}-\frac{i\,\beta\,\overline{\mu}\,\hat{v}_y}{\mathrm{Re}_e\,h_3}-\\
&\frac{i\,\beta\,\overline{\lambda}\,\hat{v}_y}{\mathrm{Re}_e\,h_3}-\frac{i\,\overline{T}_y\,\beta\,\overline{\mu}_{\overline{T}}\,\hat{v}}{\mathrm{Re}_e\,h_3}-\frac{3\,i\,\beta\,h_{3,y}\,\overline{\mu}\,\hat{v}}{\mathrm{Re}_e\,h_3^2}-\frac{i\,\beta\,h_{1,y}\,\overline{\mu}\,\hat{v}}{\mathrm{Re}_e\,h_1\,h_3}-\frac{i\,\beta\,h_{3,y}\,\overline{\lambda}\,\hat{v}}{\mathrm{Re}_e\,h_3^2}-\frac{i\,\beta\,h_{1,y}\,\overline{\lambda}\,\hat{v}}{\mathrm{Re}_e\,h_1\,h_3}-\\
&\frac{i\,\Omega_{\mathrm{Re}}\,\hat{T}\,\beta\,\overline{\lambda}_{\overline{T}}\,\overline{v}_y}{\mathrm{Re}_e\,h_3}-\frac{2\,i\,\Omega_{\mathrm{Re}}\,\hat{T}\,\beta\,h_{3,y}\,\overline{\mu}_{\overline{T}}\,\overline{v}}{\mathrm{Re}_e\,h_3^2}-\frac{i\,\Omega_{\mathrm{Re}}\,\hat{T}\,\beta\,h_{3,y}\,\overline{\lambda}_{\overline{T}}\,\overline{v}}{\mathrm{Re}_e\,h_3^2}-\frac{i\,\Omega_{\mathrm{Re}}\,\hat{T}\,\beta\,h_{1,y}\,\overline{\lambda}_{\overline{T}}\,\overline{v}}{\mathrm{Re}_e\,h_1\,h_3}-\\
&\frac{i\,\Omega_{\mathrm{Re}}\,\beta\,\overline{\mu}\,\hat{u}_s}{\mathrm{Re}_e\,h_1\,h_3}-\frac{i\,\Omega_{\mathrm{Re}}\,\beta\,\overline{\lambda}\,\hat{u}_s}{\mathrm{Re}_e\,h_1\,h_3}-\frac{i\,\Omega_{\mathrm{Re}}\,\overline{T}_s\,\beta\,\overline{\mu}_{\overline{T}}\,\hat{u}}{\mathrm{Re}_e\,h_1\,h_3}-\frac{3\,i\,\Omega_{\mathrm{Re}}\,\beta\,h_{3,s}\,\overline{\mu}\,\hat{u}}{\mathrm{Re}_e\,h_1\,h_3^2}+\frac{\alpha\,\beta\,\overline{\mu}\,\hat{u}}{\mathrm{Re}_e\,h_1\,h_3}-\\
&\frac{i\,\Omega_{\mathrm{Re}}\,\beta\,h_{3,s}\,\overline{\lambda}\,\hat{u}}{\mathrm{Re}_e\,h_1\,h_3^2}+\frac{\alpha\,\beta\,\overline{\lambda}\,\hat{u}}{\mathrm{Re}_e\,h_1\,h_3}-\frac{i\,\Omega_{\mathrm{Re}}\,\hat{T}\,\beta\,\overline{\lambda}_{\overline{T}}\,\overline{u}_s}{\mathrm{Re}_e\,h_1\,h_3}-\frac{2\,i\,\Omega_{\mathrm{Re}}\,\hat{T}\,\beta\,h_{3,s}\,\overline{\mu}_{\overline{T}}\,\overline{u}}{\mathrm{Re}_e\,h_1\,h_3^2}-\\
&\frac{i\,\Omega_{\mathrm{Re}}\,\hat{T}\,\beta\,h_{3,s}\,\overline{\lambda}_{\overline{T}}\,\overline{u}}{\mathrm{Re}_e\,h_1\,h_3^2}+\frac{i\,\overline{T}\,\beta\,\hat{\rho}}{{\mathrm{M}_e}^2\,\gamma_e\,h_3}+\frac{i\,\hat{T}\,\beta\,\overline{\rho}}{{\mathrm{M}_e}^2\,\gamma_e\,h_3}=0
\end{aligned}
$$

B.3.4 Conservation of Energy

$$
\begin{aligned}
&-\frac{2\,\mathrm{Ec}_e\,\overline{\mu}\,\overline{w}_y\,\hat{w}_y}{\mathrm{Re}_e}+\frac{2\,\mathrm{Ec}_e\,h_{3,y}\,\overline{\mu}\,\overline{w}\,\hat{w}_y}{\mathrm{Re}_e\,h_3}+\frac{2\,\mathrm{Ec}_e\,h_{3,y}\,\overline{\mu}\,\overline{w}_y\,\hat{w}}{\mathrm{Re}_e\,h_3}-\frac{2\,i\,\mathrm{Ec}_e\,\Omega_{\mathrm{Re}}\,\alpha\,\overline{\mu}\,\overline{w}_s\,\hat{w}}{\mathrm{Re}_e\,h_1^2}-\\
&\frac{2\,\mathrm{Ec}_e\,\left(h_{3,y}\right)^2\,\overline{\mu}\,\overline{w}\,\hat{w}}{\mathrm{Re}_e\,h_3^2}+\frac{2\,i\,\mathrm{Ec}_e\,\Omega_{\mathrm{Re}}\,\alpha\,h_{3,s}\,\overline{\mu}\,\overline{w}\,\hat{w}}{\mathrm{Re}_e\,h_1^2\,h_3}-\frac{2\,i\,\mathrm{Ec}_e\,\Omega_{\mathrm{Re}}\,\beta\,\overline{\lambda}\,\overline{v}_y\,\hat{w}}{\mathrm{Re}_e\,h_3}-
\end{aligned}
$$

$$\frac{4\,i\,\mathrm{Ec}_e\,\Omega_{\mathrm{Re}}\,\beta\,h_{3,y}\,\overline{\mu}\,\overline{v}\,\hat{w}}{\mathrm{Re}_e\,h_3^2}-\frac{2\,i\,\mathrm{Ec}_e\,\Omega_{\mathrm{Re}}\,\beta\,h_{3,y}\,\overline{\lambda}\,\overline{v}\,\hat{w}}{\mathrm{Re}_e\,h_3^2}-\frac{2\,i\,\mathrm{Ec}_e\,\Omega_{\mathrm{Re}}\,\beta\,h_{1,y}\,\overline{\lambda}\,\overline{v}\,\hat{w}}{\mathrm{Re}_e\,h_1\,h_3}-$$
$$\frac{2\,i\,\mathrm{Ec}_e\,\Omega_{\mathrm{Re}}\,\beta\,\overline{\lambda}\,\overline{u}_s\,\hat{w}}{\mathrm{Re}_e\,h_1\,h_3}-\frac{4\,i\,\mathrm{Ec}_e\,\Omega_{\mathrm{Re}}\,\beta\,h_{3,s}\,\overline{\mu}\,\overline{u}\,\hat{w}}{\mathrm{Re}_e\,h_1\,h_3^2}-\frac{2\,i\,\mathrm{Ec}_e\,\Omega_{\mathrm{Re}}\,\beta\,h_{3,s}\,\overline{\lambda}\,\overline{u}\,\hat{w}}{\mathrm{Re}_e\,h_1\,h_3^2}-\frac{\mathrm{Ec}_e\,\hat{T}\,\overline{\mu}_{\overline{T}}\,\left(\overline{w}_y\right)^2}{\mathrm{Re}_e}+$$
$$\frac{2\,\mathrm{Ec}_e\,\hat{T}\,h_{3,y}\,\overline{\mu}_{\overline{T}}\,\overline{w}\,\overline{w}_y}{\mathrm{Re}_e\,h_3}-\frac{2\,i\,\mathrm{Ec}_e\,\beta\,\overline{\mu}\,\hat{v}\,\overline{w}_y}{\mathrm{Re}_e\,h_3}-\frac{2\,i\,\mathrm{Ec}_e\,\Omega_{\mathrm{Re}}\,\beta\,\overline{\mu}\,\hat{u}\,\overline{w}_s}{\mathrm{Re}_e\,h_1\,h_3}-\frac{\mathrm{Ec}_e\,\hat{T}\,\left(h_{3,y}\right)^2\,\overline{\mu}_{\overline{T}}\,\overline{w}^2}{\mathrm{Re}_e\,h_3^2}+$$
$$\frac{2\,i\,\mathrm{Ec}_e\,\beta\,h_{3,y}\,\overline{\mu}\,\hat{v}\,\overline{w}}{\mathrm{Re}_e\,h_3^2}+\frac{2\,i\,\mathrm{Ec}_e\,\Omega_{\mathrm{Re}}\,\beta\,h_{3,s}\,\overline{\mu}\,\hat{u}\,\overline{w}}{\mathrm{Re}_e\,h_1\,h_3^2}-\frac{i\,\mathrm{Ec}_e\,\overline{T}\,\beta\,\hat{\rho}\,\overline{w}}{\mathrm{M}_e{}^2\,\gamma_e\,h_3}-\frac{i\,\mathrm{Ec}_e\,\hat{T}\,\beta\,\overline{\rho}\,\overline{w}}{\mathrm{M}_e{}^2\,\gamma_e\,h_3}+\frac{i\,\hat{T}\,\beta\,\overline{c}_p\,\overline{\rho}\,\overline{w}}{h_3}-$$
$$\frac{4\,\mathrm{Ec}_e\,\Omega_{\mathrm{Re}}\,\overline{\mu}\,\overline{v}_y\,\hat{v}_y}{\mathrm{Re}_e}-\frac{2\,\mathrm{Ec}_e\,\Omega_{\mathrm{Re}}\,\overline{\lambda}\,\overline{v}_y\,\hat{v}_y}{\mathrm{Re}_e}-\frac{2\,\mathrm{Ec}_e\,\Omega_{\mathrm{Re}}\,h_{3,y}\,\overline{\lambda}\,\overline{v}\,\hat{v}_y}{\mathrm{Re}_e\,h_3}-\frac{2\,\mathrm{Ec}_e\,\Omega_{\mathrm{Re}}\,h_{1,y}\,\overline{\lambda}\,\overline{v}\,\hat{v}_y}{\mathrm{Re}_e\,h_1}-$$
$$\frac{2\,\mathrm{Ec}_e\,\Omega_{\mathrm{Re}}\,\overline{\lambda}\,\overline{u}_s\,\hat{v}_y}{\mathrm{Re}_e\,h_1}-\frac{2\,\mathrm{Ec}_e\,\Omega_{\mathrm{Re}}\,h_{3,s}\,\overline{\lambda}\,\overline{u}\,\hat{v}_y}{\mathrm{Re}_e\,h_1\,h_3}-\frac{2\,\mathrm{Ec}_e\,\Omega_{\mathrm{Re}}\,\overline{\mu}\,\overline{u}_y\,\hat{v}_s}{\mathrm{Re}_e\,h_1}+\frac{2\,\mathrm{Ec}_e\,\Omega_{\mathrm{Re}}\,h_{1,y}\,\overline{\mu}\,\overline{u}\,\hat{v}_s}{\mathrm{Re}_e\,h_1^2}-$$
$$\frac{2\,\mathrm{Ec}_e\,\Omega_{\mathrm{Re}}\,h_{3,y}\,\overline{\lambda}\,\overline{v}_y\,\hat{v}}{\mathrm{Re}_e\,h_3}-\frac{2\,\mathrm{Ec}_e\,\Omega_{\mathrm{Re}}\,h_{1,y}\,\overline{\lambda}\,\overline{v}_y\,\hat{v}}{\mathrm{Re}_e\,h_1}-\frac{4\,\mathrm{Ec}_e\,\Omega_{\mathrm{Re}}\,\left(h_{3,y}\right)^2\,\overline{\mu}\,\overline{v}\,\hat{v}}{\mathrm{Re}_e\,h_3^2}-$$
$$\frac{4\,\mathrm{Ec}_e\,\Omega_{\mathrm{Re}}\,\left(h_{1,y}\right)^2\,\overline{\mu}\,\overline{v}\,\hat{v}}{\mathrm{Re}_e\,h_1^2}-\frac{2\,\mathrm{Ec}_e\,\Omega_{\mathrm{Re}}\,\left(h_{3,y}\right)^2\,\overline{\lambda}\,\overline{v}\,\hat{v}}{\mathrm{Re}_e\,h_3^2}-\frac{4\,\mathrm{Ec}_e\,\Omega_{\mathrm{Re}}\,h_{1,y}\,h_{3,y}\,\overline{\lambda}\,\overline{v}\,\hat{v}}{\mathrm{Re}_e\,h_1\,h_3}-$$
$$\frac{2\,\mathrm{Ec}_e\,\Omega_{\mathrm{Re}}\,\left(h_{1,y}\right)^2\,\overline{\lambda}\,\overline{v}\,\hat{v}}{\mathrm{Re}_e\,h_1^2}-\frac{2\,i\,\mathrm{Ec}_e\,\alpha\,\overline{\mu}\,\overline{u}_y\,\hat{v}}{\mathrm{Re}_e\,h_1}-\frac{4\,\mathrm{Ec}_e\,\Omega_{\mathrm{Re}}\,h_{1,y}\,\overline{\mu}\,\overline{u}_s\,\hat{v}}{\mathrm{Re}_e\,h_1^2}-\frac{2\,\mathrm{Ec}_e\,\Omega_{\mathrm{Re}}\,h_{3,y}\,\overline{\lambda}\,\overline{u}_s\,\hat{v}}{\mathrm{Re}_e\,h_1\,h_3}-$$
$$\frac{2\,\mathrm{Ec}_e\,\Omega_{\mathrm{Re}}\,h_{1,y}\,\overline{\lambda}\,\overline{u}_s\,\hat{v}}{\mathrm{Re}_e\,h_1^2}-\frac{4\,\mathrm{Ec}_e\,\Omega_{\mathrm{Re}}\,h_{3,s}\,h_{3,y}\,\overline{\mu}\,\overline{u}\,\hat{v}}{\mathrm{Re}_e\,h_1\,h_3^2}+\frac{2\,i\,\mathrm{Ec}_e\,\alpha\,h_{1,y}\,\overline{\mu}\,\overline{u}\,\hat{v}}{\mathrm{Re}_e\,h_1^2}-$$
$$\frac{2\,\mathrm{Ec}_e\,\Omega_{\mathrm{Re}}\,h_{3,s}\,h_{3,y}\,\overline{\lambda}\,\overline{u}\,\hat{v}}{\mathrm{Re}_e\,h_1\,h_3^2}-\frac{2\,\mathrm{Ec}_e\,\Omega_{\mathrm{Re}}\,h_{1,y}\,h_{3,s}\,\overline{\lambda}\,\overline{u}\,\hat{v}}{\mathrm{Re}_e\,h_1^2\,h_3}-\frac{\mathrm{Ec}_e\,\overline{T}\,\overline{\rho}_y\,\hat{v}}{\mathrm{M}_e{}^2\,\gamma_e}-\frac{\mathrm{Ec}_e\,\overline{T}_y\,\overline{\rho}\,\hat{v}}{\mathrm{M}_e{}^2\,\gamma_e}+\overline{T}_y\,\overline{c}_p\,\overline{\rho}\,\hat{v}-$$
$$\frac{2\,i\,\mathrm{Ec}_e\,\Omega_{\mathrm{Re}}\,\alpha\,\overline{\lambda}\,\hat{u}\,\overline{v}_y}{\mathrm{Re}_e\,h_1}-\frac{4\,i\,\mathrm{Ec}_e\,\Omega_{\mathrm{Re}}\,\alpha\,h_{1,y}\,\overline{\mu}\,\hat{u}\,\overline{v}}{\mathrm{Re}_e\,h_1^2}-\frac{2\,i\,\mathrm{Ec}_e\,\Omega_{\mathrm{Re}}\,\alpha\,h_{3,y}\,\overline{\lambda}\,\hat{u}\,\overline{v}}{\mathrm{Re}_e\,h_1\,h_3}-$$
$$\frac{2\,i\,\mathrm{Ec}_e\,\Omega_{\mathrm{Re}}\,\alpha\,h_{1,y}\,\overline{\lambda}\,\hat{u}\,\overline{v}}{\mathrm{Re}_e\,h_1^2}-\frac{\mathrm{Ec}_e\,\overline{T}\,\hat{\rho}_y\,\overline{v}}{\mathrm{M}_e{}^2\,\gamma_e}-\frac{\mathrm{Ec}_e\,\overline{T}_y\,\hat{\rho}\,\overline{v}}{\mathrm{M}_e{}^2\,\gamma_e}+\overline{T}_y\,\overline{c}_p\,\hat{\rho}\,\overline{v}-\frac{\mathrm{Ec}_e\,\hat{T}\,\overline{\rho}_y\,\overline{v}}{\mathrm{M}_e{}^2\,\gamma_e}-\frac{\mathrm{Ec}_e\,\hat{T}_y\,\overline{\rho}\,\overline{v}}{\mathrm{M}_e{}^2\,\gamma_e}+$$
$$\hat{T}_y\,\overline{c}_p\,\overline{\rho}\,\overline{v}-\frac{2\,\mathrm{Ec}_e\,\overline{\mu}\,\overline{u}_y\,\hat{u}_y}{\mathrm{Re}_e}+\frac{2\,\mathrm{Ec}_e\,h_{1,y}\,\overline{\mu}\,\overline{u}\,\hat{u}_y}{\mathrm{Re}_e\,h_1}+\frac{2\,\mathrm{Ec}_e\,h_{1,y}\,\overline{\mu}\,\overline{u}_y\,\hat{u}}{\mathrm{Re}_e\,h_1}-\frac{4\,i\,\mathrm{Ec}_e\,\Omega_{\mathrm{Re}}\,\alpha\,\overline{\mu}\,\overline{u}_s\,\hat{u}}{\mathrm{Re}_e\,h_1^2}-$$
$$\frac{2\,i\,\mathrm{Ec}_e\,\Omega_{\mathrm{Re}}\,\alpha\,\overline{\lambda}\,\overline{u}_s\,\hat{u}}{\mathrm{Re}_e\,h_1^2}-\frac{2\,\mathrm{Ec}_e\,\left(h_{1,y}\right)^2\,\overline{\mu}\,\overline{u}\,\hat{u}}{\mathrm{Re}_e\,h_1^2}-\frac{2\,i\,\mathrm{Ec}_e\,\Omega_{\mathrm{Re}}\,\alpha\,h_{3,s}\,\overline{\lambda}\,\overline{u}\,\hat{u}}{\mathrm{Re}_e\,h_1^2\,h_3}-\frac{\mathrm{Ec}_e\,\Omega_p\,\overline{T}\,\overline{\rho}_s\,\hat{u}}{\mathrm{M}_e{}^2\,\gamma_e\,h_1}-$$
$$\frac{\mathrm{Ec}_e\,\Omega_p\,\overline{T}_s\,\overline{\rho}\,\hat{u}}{\mathrm{M}_e{}^2\,\gamma_e\,h_1}+\frac{\overline{T}_s\,\overline{c}_p\,\overline{\rho}\,\hat{u}}{h_1}-\frac{\mathrm{Ec}_e\,\hat{T}\,\overline{\mu}_{\overline{T}}\,\left(\overline{u}_y\right)^2}{\mathrm{Re}_e}+\frac{2\,\mathrm{Ec}_e\,\hat{T}\,h_{1,y}\,\overline{\mu}_{\overline{T}}\,\overline{u}\,\overline{u}_y}{\mathrm{Re}_e\,h_1}-\frac{\mathrm{Ec}_e\,\hat{T}\,\left(h_{1,y}\right)^2\,\overline{\mu}_{\overline{T}}\,\overline{u}^2}{\mathrm{Re}_e\,h_1^2}-$$
$$\frac{\mathrm{Ec}_e\,\Omega_p\,\overline{T}\,\hat{\rho}_s\,\overline{u}}{\mathrm{M}_e{}^2\,\gamma_e\,h_1}-\frac{i\,\mathrm{Ec}_e\,\Omega_p\,\overline{T}\,\alpha\,\hat{\rho}\,\overline{u}}{\mathrm{M}_e{}^2\,\gamma_e\,h_1}-\frac{\mathrm{Ec}_e\,\Omega_p\,\overline{T}_s\,\hat{\rho}\,\overline{u}}{\mathrm{M}_e{}^2\,\gamma_e\,h_1}+\frac{\overline{T}_s\,\overline{c}_p\,\hat{\rho}\,\overline{u}}{h_1}-\frac{\mathrm{Ec}_e\,\Omega_p\,\hat{T}\,\overline{\rho}_s\,\overline{u}}{\mathrm{M}_e{}^2\,\gamma_e\,h_1}-$$
$$\frac{i\,\mathrm{Ec}_e\,\Omega_p\,\hat{T}\,\alpha\,\overline{\rho}\,\overline{u}}{\mathrm{M}_e{}^2\,\gamma_e\,h_1}-\frac{\mathrm{Ec}_e\,\Omega_p\,\hat{T}_s\,\overline{\rho}\,\overline{u}}{\mathrm{M}_e{}^2\,\gamma_e\,h_1}+\frac{i\,\hat{T}\,\alpha\,\overline{c}_p\,\overline{\rho}\,\overline{u}}{h_1}+\frac{\hat{T}_s\,\overline{c}_p\,\overline{\rho}\,\overline{u}}{h_1}+\frac{i\,\mathrm{Ec}_e\,\overline{T}\,\omega\,\hat{\rho}}{\mathrm{M}_e{}^2\,\gamma_e}+\frac{i\,\mathrm{Ec}_e\,\hat{T}\,\omega\,\overline{\rho}}{\mathrm{M}_e{}^2\,\gamma_e}-$$

$$i\,\hat{T}\,\overline{c}_p\,\omega\,\overline{\rho} - \frac{\left(\overline{T}_y\right)^2\,\hat{T}\,\overline{\kappa}_{\overline{T}\,\overline{T}}}{\mathrm{Pr}_e\,\mathrm{Re}_e} - \frac{\overline{T}_y\,\hat{T}\,h_{3,y}\,\overline{\kappa}_{\overline{T}}}{\mathrm{Pr}_e\,\mathrm{Re}_e\,h_3} - \frac{\overline{T}_y\,\hat{T}\,h_{1,y}\,\overline{\kappa}_{\overline{T}}}{\mathrm{Pr}_e\,\mathrm{Re}_e\,h_1} - \frac{2\,i\,\Omega_{\mathrm{Re}}\,\overline{T}_s\,\hat{T}\,\alpha\,\overline{\kappa}_{\overline{T}}}{\mathrm{Pr}_e\,\mathrm{Re}_e\,h_1^2} - \frac{2\,\overline{T}_y\,\hat{T}_y\,\overline{\kappa}_{\overline{T}}}{\mathrm{Pr}_e\,\mathrm{Re}_e} -$$
$$\frac{\overline{T}_{y\,y}\,\hat{T}\,\overline{\kappa}_{\overline{T}}}{\mathrm{Pr}_e\,\mathrm{Re}_e} - \frac{\hat{T}_y\,h_{3,y}\,\overline{\kappa}}{\mathrm{Pr}_e\,\mathrm{Re}_e\,h_3} - \frac{i\,\Omega_{\mathrm{Re}}\,\hat{T}\,\alpha\,h_{3,s}\,\overline{\kappa}}{\mathrm{Pr}_e\,\mathrm{Re}_e\,h_1^2\,h_3} + \frac{\hat{T}\,\beta^2\,\overline{\kappa}}{\mathrm{Pr}_e\,\mathrm{Re}_e\,h_3^2} - \frac{\hat{T}_y\,h_{1,y}\,\overline{\kappa}}{\mathrm{Pr}_e\,\mathrm{Re}_e\,h_1} + \frac{i\,\Omega_{\mathrm{Re}}\,\hat{T}\,\alpha\,h_{1,s}\,\overline{\kappa}}{\mathrm{Pr}_e\,\mathrm{Re}_e\,h_1^3} -$$
$$\frac{i\,\Omega_{\mathrm{Re}}\,\hat{T}\,\alpha_s\,\overline{\kappa}}{\mathrm{Pr}_e\,\mathrm{Re}_e\,h_1^2} + \frac{\hat{T}\,\alpha^2\,\overline{\kappa}}{\mathrm{Pr}_e\,\mathrm{Re}_e\,h_1^2} - \frac{2\,i\,\Omega_{\mathrm{Re}}\,\hat{T}_s\,\alpha\,\overline{\kappa}}{\mathrm{Pr}_e\,\mathrm{Re}_e\,h_1^2} - \frac{\hat{T}_{y\,y}\,\overline{\kappa}}{\mathrm{Pr}_e\,\mathrm{Re}_e} = 0$$

B.3.5 Continuity

$$\frac{i\,\beta\,\overline{\rho}\,\hat{w}}{h_3} + \frac{i\,\beta\,\hat{\rho}\,\overline{w}}{h_3} + \overline{\rho}\,\hat{v}_y + \overline{\rho}_y\,\hat{v} + \frac{h_{3,y}\,\overline{\rho}\,\hat{v}}{h_3} + \frac{h_{1,y}\,\overline{\rho}\,\hat{v}}{h_1} + \hat{\rho}\,\overline{v}_y + \hat{\rho}_y\,\overline{v} + \frac{h_{3,y}\,\hat{\rho}\,\overline{v}}{h_3} + \frac{h_{1,y}\,\hat{\rho}\,\overline{v}}{h_1} + \frac{\overline{\rho}\,\hat{u}_s}{h_1} +$$
$$\frac{\overline{\rho}_s\,\hat{u}}{h_1} + \frac{h_{3,s}\,\overline{\rho}\,\hat{u}}{h_1\,h_3} + \frac{i\,\alpha\,\overline{\rho}\,\hat{u}}{h_1} + \frac{\hat{\rho}\,\overline{u}_s}{h_1} + \frac{\hat{\rho}_s\,\overline{u}}{h_1} + \frac{h_{3,s}\,\hat{\rho}\,\overline{u}}{h_1\,h_3} + \frac{i\,\alpha\,\hat{\rho}\,\overline{u}}{h_1} - i\,\omega\,\hat{\rho} = 0$$

APPENDIX C

WAVE ANGLES AND STREAMLINE ANGLES

Table C.1: Wave angle and streamline angle values for the sweep angle variation study. These parameters correspond to the most amplified disturbances as presented in Figure 3.3, considering the design angle of attack ($\alpha = -1.520°$).

side,	Λ [°],	ψ_w [°]	ψ_s [°]	$\psi_w - \psi_s$ [°]
top,	0	+23.87	+0.00	+23.87
	5	+37.38	+3.78	+33.61
	10	+43.88	+7.57	+36.32
	15	+93.30	+10.19	+83.11
	20	+98.02	+13.72	+84.30
	25	+101.65	+17.37	+84.28
	30	+103.98	+21.16	+82.81
bottom,	0	+0.00	+0.00	+0.00
	5	−24.50	−4.31	−20.19
	10	−45.46	−8.46	−37.00
	15	−96.58	−12.45	−84.12
	20	−101.94	−16.65	−85.30
	25	−106.23	−20.86	−85.37
	30	−109.42	−25.19	−84.23

Table C.2: Wave angle and streamline angle values for the $\Lambda = 12.5°$ sweep case angle of attack variation study. These parameters characterize the most relevant disturbances for this sweep angle with varying angles of attack as seen in Figure 3.4. The points where this data was extracted are indicated by grey circles in this figure.

side,	α [°],	x/c [%]	ψ_w [°]	ψ_s [°]	$\psi_w - \psi_s$ [°]
top,	−1.772	36	+62.37	+11.44	+50.93
	−1.520	37	+57.41	+11.29	+46.11
	−1.272	38	+57.89	+11.17	+46.72
	−1.772	71	+94.33	+10.29	+84.04
	−1.520	70	+94.44	+10.27	+84.17
	−1.272	73	+91.67	+10.13	+81.54
bottom,	−1.772	8	−45.02	−14.32	−30.70
	−1.772	55	−96.55	−12.40	−84.15
	−1.520	55	−96.58	−12.46	−84.12
	−1.272	56	−96.60	−12.51	−84.09

Table C.3: Wave angle and streamline angle values for the $\Lambda = 12.5°$ sweep case angle of attack variation study. These parameters characterize the most relevant disturbances for this sweep angle with varying angles of attack as seen in Figure 3.6. The points where this data was extracted are indicated by grey circles in this figure.

side,	$\alpha\,[°]$,	$x/c\,[\%]$	$\psi_w\,[°]$	$\psi_s\,[°]$	$\psi_w - \psi_s\,[°]$
top,	-1.772	37	$+55.57$	$+9.49$	$+46.08$
	-1.520	38	$+56.10$	$+9.37$	$+46.72$
	-1.272	38	$+56.55$	$+9.28$	$+47.27$
	-1.772	70	$+92.81$	$+8.60$	$+84.22$
	-1.520	70	$+91.31$	$+8.54$	$+82.77$
	-1.272	70	$+91.27$	$+8.48$	$+82.79$
bottom,	-1.772	9	-37.30	-11.89	-25.41
	-1.520	8	-36.51	-12.20	-24.31
	-1.772	60	-60.11	-10.22	-49.89
	-1.520	52	-94.49	-10.43	-84.06
	-1.272	52	-94.52	-10.47	-84.05